IPP-Report

MAX-PLANCK-INSTITUT
FÜR PLASMAPHYSIK

Felix Paulus

Studies of propagating slow waves in the ion cyclotron range of frequencies

IPP 2024-03
Januar 2024

Studies of propagating slow waves in the ion cyclotron range of frequencies

Felix Paulus

München 2023

Studies of propagating slow waves in the ion cyclotron range of frequencies

Dissertation
an der Fakultät für Physik
der Ludwig-Maximilians-Universität
München

vorgelegt von
Felix Paulus
aus Celle

München, 30. Oktober 2023

Erstgutachter:	Prof. Dr. Hartmut Zohm
Zweitgutachter:	Prof. Dr. Stéphan Heuraux
Tag der mündlichen Prüfung:	20. Dezember 2023

Zusammenfassung

Die Produktion von elektrischem Strom mittels Kernfusion stellt ein weitgehend Treibhausgas freies und sicheres Verfahren dar. Reaktorkonzepte basierend auf dem Ansatz des magnetischen Einschlusses sind heute weit fortgeschritten. Hierbei wird ein Deuterium-Tritium-Plasma mit einem Magnetfeldkäfig eingeschlossen und die Plasmatemperatur so weit erhöht, dass es zur Kernfusion kommt. Um die Temperatur des Plasmas zu erhöhen, wurden unterschiedliche Verfahren entwickelt. Ein Verfahren ist das Heizen mittels elektromagnetischer Wellen im Bereich der Ionen-Zyklotron-Resonanz-Frequenz (engl. Abkürzung: ICRF). Die ICRF-Wellen werden von Antennen, die in die Reaktorwand integriert sind, in das Plasma eingespeist. Die eingebrachte Leistung geht dann mittels Wechselwirkungsmechanismen zwischen der Welle und den geladenen Teilchen an das Plasma über.

Obwohl das Verfahren etabliert ist, ist dessen Anwendung in zukünftigen Fusionsreaktoren umstritten. Grund hierfür ist ein unerwünschter Nebeneffekt, der beim Betrieb der ICRF-Antennen auftreten kann. Es wurde beobachtet, dass der Betrieb der ICRF Antennen zu einer verstärkten Verunreinigung des Plasmas durch Partikel der Reaktorwand führen kann. Dies erschwert den Zugang zu fortschrittlichen Betriebsszenarien, die als reaktorrelevant gelten. Ursprung der Verunreinigung ist vermutlich ein Gleichrichteffekt der Hochfrequenz-Felder (HF-Felder) an der nicht linearen Plasma-Randschicht, was dann zu Sputtern führt. Weil sich die geladenen Plasmateilchen hauptsächlich entlang der Magnetfeldlinien bewegen, wird davon ausgegangen, dass die parallele Komponente der HF-Felder hierfür verantwortlich ist. Die sogenannte langsame Welle, eine der Lösungen der Dispersionsrelation des Plasmas, ist ein möglicher Träger dieser Signale. Wenn sich die langsame Welle im Reaktor ausbreitet, besteht das Risiko, dass das Sputtern an Orten auftritt, die weit entfernt von der Quelle sind. Weil sich die langsame Welle nur in Plasmen mit niedriger Ladungsträgerdichte ausbreitet, kommt dafür nur der äußere Bereich des Reaktors, die sogenannte Abschälschicht, engl. scrape-off layer (SOL), infrage.

Es ist Ziel dieser Arbeit, die Ausbreitung der langsamen Welle im ICRF-Bereich in einem reaktorrelevanten SOL zu untersuchen. Hierfür wurden Simulationen mit der RAPLICASOL-Routine und Experimente am IShTAR-Teststand und am ASDEX Upgrade (AUG) Tokamak durchgeführt. Die Simulationen mit RAPLICASOL zeigen, dass sich die langsame Welle im relevanten Parameterbereich in Form von Resonanzkegeln manifestiert. Diese wurden in Experimenten am IShTAR-Teststand nachgewiesen. Dafür wurde eine lokalisierte HF-Quelle in den Teststand platziert und die Feldverteilung mit HF-Sonden vermessen. Der Wellentyp wurde anhand der Reaktion der Feldverteilung auf Änderungen der Plasma-Parameter identifiziert. Das an IShTAR etablierte Verfahren wurde dann auf die Versuche am AUG übertragen. Hier wurde ein Element der Reaktorwand modifiziert, um von hier aus HF-Felder in den Tokamak zu senden. Basierend auf den Erfahrungen am IShTAR-Experiment wurden Sonden am Mittelebenenmanipulator benutzt, um das HF-Feld zu sondieren. Die Messergebnisse deuten darauf hin, dass sich die langsame Welle in Form von Resonanzkegel durch den SOL in AUG ausbreitet, wenn die Ladungsträgerdichte ausreichend niedrig ist.

Contents

Chapter 1

Introduction

Looking at the recent past suggests that the electricity demand will increase continuously in the foreseeable future. When humanity decides to restrict or abandon the usage of fossil fuels for electricity production, other energy sources have to take over. Besides renewables, nuclear energy is a largely greenhouse-gas-free energy source. Nuclear power plants, based on the fission of heavy radioactive elements, have been in use since the 1950s but until now have not become the leading source of electricity. Reasons for this are partially safety concerns, but economic aspects are relevant too. The fusion of light elements explains the energy release in stars and poses another path towards harnessing nuclear energy. The fusion of two nuclei occurs in collision events when the particles' kinetic energy difference exceeds the repulsive coulomb barrier. Studies have shown that the reaction cross-section of the hydrogen isotopes deuterium (D) and tritium (T) is the highest for kinetic energies between 20 keV and 200 keV [1]. Most technical approaches consequently attempt to access fusion energy using D-T-fuel. Essential advantages of nuclear fusion compared to fission are that meltdowns are impossible, the absence of long-term radioactive waste, and that the D-T-fuel is practically endless and accessible everywhere. Two approaches towards a technical realization prevailed: inertial and magnetic confinement fusion.

In inertial confinement fusion (ICF), short, intense laser pulses irradiate a small D-T-pellet, the target. The pressure and temperature within the target increase rapidly to a point where thermonuclear reactions occur. A recent ICF experiment at the "National Ignition Facility" achieved a milestone [2]: fusion processes released more energy than the laser pulses delivered to the target. While there is fast progress in ICF research, reactor concepts are less developed compared to the magnetic confinement fusion approach.

In magnetic confinement fusion (MCF), a small amount of D-T-gas is released into a vacuum vessel with a strong magnetic field. The gas temperature is increased until the atoms ionize and the gas transitions into the plasma state. The electrically charged particles are forced to orbit around the magnetic field lines, and the plasma becomes confined. Since the beginning of MCF research in the 1950s, two types of experiments have performed exceptionally well and are considered candidates for future fusion power plants. These are the so-called tokamak and stellarator

concepts. Both have a toroidal shape, and the plasma is confined to a ring-like volume. The two concepts differ in how the poloidal component of the magnetic field is created. A poloidal magnetic field component is required to compensate for outward drifts arising from magnetic field gradients and curvature. In a tokamak, a transformer induces a large electric current in the toroidal direction to create the poloidal magnetic field. In a stellarator, the external magnetic field itself is deformed by complex-shaped magnetic field coils.

Over the past decades, significant progress has been made with both MCF concepts. Recently, these resulted in noteworthy achievements towards a fusion power plant. At the end of 2021, an experiment with D-T-fuel at the Joint European Torus (JET) tokamak released a record of 59 MJ of heat energy from fusion [3]. In 2023, a record in energy turnover of 1.3 GJ over more than 8 minutes was achieved at the Wendelstein 7-X stellarator [4], a milestone for stellarators that lags in development behind tokamaks until now. The most prominent upcoming milestones in MCF are experiments at the ITER tokamak, which is being built in Saint-Paul-lès-Durance in France [5]. The largest fusion experiment to date is designed to release ten times the amount of power that is needed to keep the fusion process running. It is considered the predecessor of the first generation of fusion power plants.

Different procedures were developed to heat the confined plasma in MCF. One method is heating the plasma with electromagnetic waves in the ion cyclotron range of frequencies (ICRF). The cyclotron frequency $\omega_c/2\pi = qB_0/m$ is the frequency at which the particle with mass m and charge q gyrate around the magnetic field lines with amplitude B_0. For deuterium ions, it is in the radio frequency (RF) range and about 7.5 MHz/T. Transferring RF power from the generators into the plasma can conceptually be separated into three steps: coupling, propagation, and absorption. The RF power is coupled from (several) antennas in the form of electromagnetic waves into the plasma. The coupling depends on the antenna geometry, the radio frequency, and the plasma parameter in front of the antenna. Once excited, the electromagnetic waves propagate through the plasma to a point where they are absorbed by wave-particle interactions. Different absorption mechanisms can be exploited, the so-called heating schemes [6]. A common heating scheme in modern MCF experiments is hydrogen minority heating, where a minor fraction of hydrogen is added to the fuel. In this scenario, the wave frequency coincides with the cyclotron frequency of the hydrogen ions at some point in the experiments, and the wave is absorbed there. The hot hydrogen ions then redistribute the energy to the plasma via collisions with the other ions and electrons.

ICRF antennas are typically designed to excite one solution of the electromagnetic wave equation, the so-called fast wave, and suppress the other, the so-called slow wave. As the fast wave propagates in plasma with plasma density above the lower hybrid resonance density only, the plasma is generally close to the ICRF antennas. While ICRF heating has been used for decades, an unwanted byproduct impedes its applicability in modern experiments. It was observed that components forming the antenna periphery show enhanced erosion during ICRF heating [7]. The released material contaminates the plasma and poses a loss mechanism for the energy stored in the plasma by transforming heat into radiation. A consequence is

that access to advanced operation scenarios, such as the high confinement mode, a candidate for the operation of future power plants, is inhibited. The process became increasingly relevant when reactor-relevant wall components were installed in MCF experiments [8]. These components usually contain elements with high atomic numbers, such as tungsten. With the presence of heavy nuclei, the radiation losses grow as the cumulative ionization energy increases. Studies suggest that the cause of the increased erosion are RF fields in the antenna periphery that are rectified at the non-linear plasma sheath. The hereby generated time-averaged potential drop accelerates the ions onto the wall, which causes sputtering. Charged particles in a magnetized plasma are confined to move along the magnetic field, implying the presence of parallel RF electric field components. Based on this understanding, an ICRF antenna with reduced parallel RF electric fields at the antenna periphery was developed, and two of them were installed at the ASDEX Upgrade (AUG) tokamak. Experiments confirmed the absence of increased plasma contamination during ICRF heating [9].

The properties of the ICRF slow wave are such that it is a plausible carrier for the parallel RF electric fields in the plasma. If the plasma density in the outer edge of the tokamak plasma, the so-called scrape-off layer (SOL), is low enough, the slow wave propagates, and RF electric fields are distributed through the torus. This poses a risk that the sheath rectification process can be initiated in locations that are far from the actual RF source. Especially in larger MCF experiments like ITER, this becomes increasingly relevant because of the extended size of the SOL. This work intends to study the propagation of ICRF slow waves within a reactor-relevant SOL. For this purpose, a single element of the antenna periphery of the ICRF antenna in the AUG tokamak is utilized as a small localized antenna that preferably emits the ICRF slow wave into the SOL.

The following work is structured into six chapters. Chapter 2 introduces theoretical descriptions of phenomena that are relevant to this work. The experimental environment is described in detail in Chapter 3. Chapter 4 describes simulations of the propagating ICRF slow wave. Experiments performed on the easy-to-access experiment IShTAR follows in Chapter 5. Studies at AUG are discussed in chapter 6. Chapter 7 concludes the work and provides an outlook.

Chapter 2

Theoretical Overview

In physics, the term plasma designates a (gaseous) collection of particles, with a fraction of these particles being electrically charged. In many cases, plasma shows collective phenomena involving the interaction of large quantities of particles with each other or the electromagnetic field. This underlines the often kinetic nature of plasma, which in this context is then modeled using kinetic theory. Here, the particle species are described in terms of distribution functions in a six-dimensional phase space. While this description is typically considered superior, many plasma physics phenomena are sufficiently depicted using averaged values of the distribution functions and their moments. The mathematical formulation of plasma physics simplifies, making many problems easier to understand. The present chapter applies the latter approach because most of the observations discussed in the following do not require kinetic theory. The collective nature of the plasma is, however, always implicit. This chapter is a compilation of descriptions of phenomena relevant to later sections of this work. For a broader analysis, it is referred to the literature, for example, [10],[11],[12] and [13].

2.1 Fundamental plasma physics

Plasma usually consists of electrons (e), different species of ions (i), and neutral particles (n). The charged plasma particles are produced in ionization and lost in recombination events or at the boundaries of the plasma. A stationary plasma is an equilibrium state between certain source and loss terms for the charged particles. Many plasma physics phenomena depend on the density n_σ and temperature T_σ of the plasma particle species $\sigma = \{e, i, n\}$. Although plasma consists of electrically charged particles, it can be considered electrically neutral on macroscopic length scales. The plasma is referred to as being quasi-neutral, meaning that the charge density of positive and negative charges q_σ is approximately the same:

$$q_e n_e \approx \sum_\rho q_i^\rho n_i^\rho.$$

The sum is taken over the different ion species ρ that are present in the plasma. Specifically, in fusion-related experiments with a single ion species of deuterium, the

ion density is approximately equal to the electron density $n_e \approx n_i$, which is then referred to as the plasma density. On microscopic length scales, quasi-neutrality breaks down. The physical parameter that is associated with this is:

$$\lambda_D = \sqrt{\frac{\varepsilon_0 k_B T_e}{n_e e^2}}.$$

The Debye length λ_D is the characteristic length scale above which the electric potential of a test charge in a plasma drops below $\exp(-1)$ of its initial value.

A laboratory plasma is generally contained inside some vessel and consequently in contact with the vessel wall at some point. An important consequence of the large ion-to-electron mass ratio is the formation of a so-called plasma sheath at the plasma/wall boundary. A schematic representation of a static or DC sheath is shown in Figure 2.1.

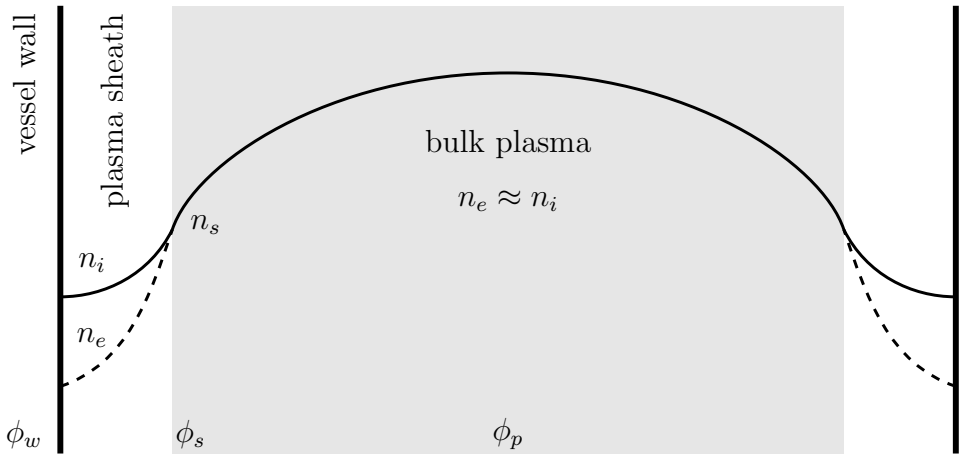

Figure 2.1: Schematic demonstrating the conditions in the plasma sheath following [11, p.60]

The formation of a plasma sheath is typically described as a consequence of the electrons having a higher mobility than the ions. Without external forces, the plasma particles move in arbitrary directions with their thermal velocities. The thermal velocity scales inversely with the square root of the particle mass. Thus, the electrons reach the vessel wall on average before the ions, and the bulk plasma remains with an excess of positive charges. The net drain of negative charges continues until the difference between the electric potential of the plasma ϕ_s and the vessel wall ϕ_w retains the electron flux to a point where it equals the ion flux. In the absence of collisions and ionization processes in the sheath and neglecting secondary emissions of electrons from the impact of the plasma particles on the wall, this potential difference is [14]:

$$\phi_s - \phi_w = \frac{k_B T_e}{e} \frac{1}{2} \ln\left(\frac{m_i}{2\pi m_e} \frac{T_e}{T_e + T_i}\right). \tag{2.1}$$

Here, m_e, T_e, and m_i, T_i are the mass and the temperature of the electrons and ions, respectively. Notice that the potential difference is taken with respect to the electric

potential at the sheath/bulk plasma boundary ϕ_s. The electric potential difference is sustained by a difference in the electron and ion density along the sheath. Both drop towards the vessel wall. However, the physical argument for why the density drop differs for the ions and electrons. The ion density falls because the ions are accelerated towards the vessel wall. Flux conservation requires that the ion density reduces when the particle velocity increases. The electron density drops because the fraction of (thermal) electrons that are repelled by the electric potential increases along the sheath. The electrons, moving with thermal velocity $\bar{v}_e$, that overcome a potential barrier of potential $\Delta\phi$ are described by the Boltzmann relation:

$$\frac{n_s \bar{v}_e}{4} \exp\left(-\frac{e\Delta\phi}{k_B T_e}\right).$$

When no external potential difference is applied, the width of the plasma sheath is in the order of a few λ_D. While λ_D depends on the plasma temperature and density, in fusion-relevant experiments, it is typically small compared to the size of the plasma. However, the plasma sheath's impact extends into the quasi-neutral plasma. In 1949, Bohm derived the so-called Bohm sheath criterion, an inequality at the sheath/bulk plasma boundary describing the necessity that the ions enter the sheath at least at the sound speed:

$$u_s = \sqrt{\frac{k_B \left(Z T_e + \gamma T_i\right)}{m_i}}. \tag{2.2}$$

Here, γ is the adiabatic coefficient for the ions. To accelerate stationary ions to their sound speed, a drop in the electric potential from the center of the bulk plasma to the sheath of at least $\phi_p - \phi_s > m_i u_s^2/2e$ is required. Provided that the electrons follow a Boltzmann relation in the bulk plasma, this causes a drop in the electron and ion density from the plasma center towards the sheath of:

$$\mathrm{f} = \frac{n_s}{n_0} = \exp\left(-\frac{Z T_e + \gamma T_i}{2 T_e}\right). \tag{2.3}$$

In experiments where $T_i << T_e$ and $Z = +1$ is applicable, this factor becomes $\mathrm{f} = \exp(-1/2) \approx 0.6$. The region along which this second potential drop occurs is called the pre-sheath. Depending on the experimental conditions, the pre-sheath can vary in size and possibly extend throughout the entire vessel.

2.2 Langmuir probes

The plasma sheath can be utilized as a diagnostic tool by inserting a small electrically conducting probe into the plasma. This approach is typically attributed to Irvin Langmuir. In the 1920s, he was among the first to study the use of electrostatic probes in plasma, hence the name Langmuir probes. The probe is connected to the vessel wall via an adjustable voltage source. Figure 2.2 shows a schematic of the setup. When the electric potential between the probe and the vessel wall

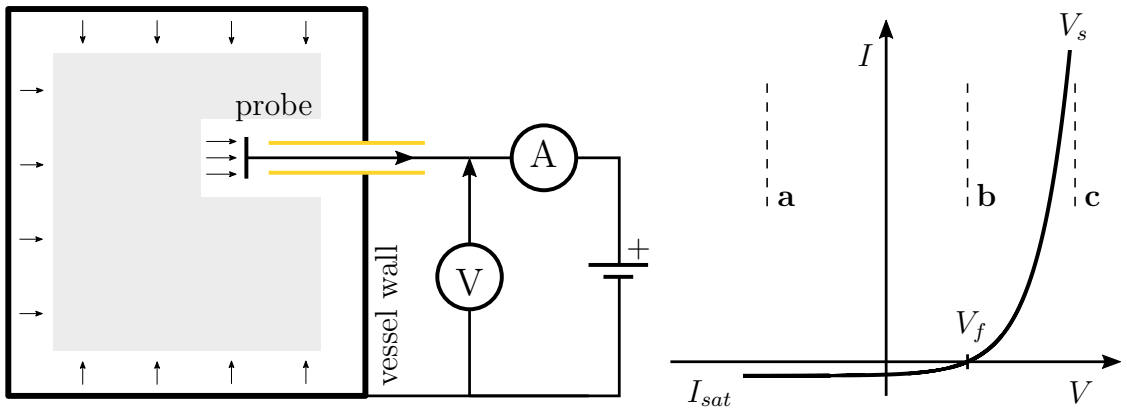

Figure 2.2: Schematic of a Langmuir probe setup and an idealized I-V characteristic

is altered, the sheath equilibrium is distorted, and an electric current I flows from the plasma through the probe, the voltage source, and the vessel wall back into the plasma. An ammeter measures the electric current, and a voltmeter measures the potential difference V between the probe and the vessel wall. The I-V characteristic of a planar probe in an idealized scenario is (for $V < V_s$):

$$I = I_{sat}\left[\exp\left(\frac{e(V - V_f)}{k_B T_e}\right) - 1\right], \tag{2.4}$$

with the ion saturation current:

$$I_{sat} = e u_s n_s A_{eff}. \tag{2.5}$$

Here, n_s is the density at the sheath/bulk plasma boundary at the probe position, and A_{eff} is the effective collection area of the probe. V_f is the so-called floating potential required to reduce the current flow through the circuit to zero. According to the previous discussion, $\phi_s - \phi_w$ (Equation (2.1)) above the floating potential is the potential at the sheath/bulk plasma boundary of the probe V_s.

For a physical interpretation, the I-V characteristic is divided into four regions where the probe collects: the ion saturation current, a net ion current, a net electron current, and the electron saturation current. In the region below **a**, $V \ll V_f$ and the probe repels all electrons. The electric current through the circuit is purely defined by the ion flux to the probe, and the probe draws the ion saturation current. In the region between **a** and **b**, $V < V_f$. The electrons are repelled, but some can overcome the electric potential barrier. The ion flux is still larger than the electron flux, and the electric current comprises a net ion current. In the region between **b** and **c**, $V > V_f$. The electric potential of the probe is still below the potential at the plasma sheath, and the ion flux is about the same as below **b**. However, the flux of electrons exceeds the ion flux to the probe past this point. Above **c**, $V > V_p$. The probe repels the ions, and the electrons are attracted. Equation (2.4) loses applicability around V_p. In experiments, this region of the characteristic is often not accessed since the large electric current would damage the probe.

In practice, it is common to program the voltage source to generate sinusoidal- or triangular-shaped voltage traces to scan the I-V characteristic. The frequency and amplitude of the traces depend on the particular experimental conditions, but typical frequencies and amplitudes are 1 kHz and up to one hundred volts. The ammeter is a small shunt resistor that transforms the current into a measurable voltage. The acquired data are fed into a computer algorithm to determine the model parameters that approximate the data points. Equation (2.4) shows the parameters u_s, n_s, A_{eff}, and T_e. However, u_s does depend only on the temperature of the plasma particles. There are physical processes that modify the effective collection area of the probe, for example, sheath expansion. However, as a first approximation, it is common to set A_{eff} equal to the geometrical surface area of the probe in the absence of a strong magnetic field. Consequently, the algorithm provides n_s and T_e. Calculating the plasma density from n_s is possible, provided the density drop along the pre-sheath f (Equation (2.3)) is known.

2.3 Radio frequency sheath

Radio frequent perturbations of the electromagnetic field in a sheath may, on time average, enhance the effect of the static sheath. This phenomenon is called the RF sheath. Compared to the DC sheath, RF sheaths can extend deeper into the plasma, and the potential drop along the sheath depends on the amplitude of the RF field amplitude. Lieberman formulated an analytical description of how RF sheaths develop [15]. He describes a simplified one-dimensional scenario that outlines the physical mechanism. The model applies when the frequency of the electromagnetic field perturbation $\omega/2\pi$ is above the plasma frequency of the ions ω_{pi} but below the plasma frequency of the electrons ω_{pe}. The plasma frequency represents the natural response time of a charged particle in plasma and is given as:

$$\omega_{p\sigma}^2 = \frac{n_\sigma q_\sigma^2}{\varepsilon_0 m_\sigma}. \tag{2.6}$$

Here, q_σ is the electric charge of the particle species. In the context of nuclear fusion with deuterium and tritium, the charge of ions is typically $q_i = -q_e = e$, and the plasma frequency of the electrons is by a factor of $\sqrt{m_i/m_e}$ larger than the plasma frequency of the ions. In the given frequency range, the electrons respond virtually instantaneously to the field perturbations, while the ions can not. In the sheath, the electrons adapt to a series of momentary states while the ions adapt to a time-averaged condition. This is emphasized in Figure 2.3. It shows the distribution of the ion and electron density along the RF sheath, as considered in [15]. The electrons move back and forth within the RF sheath depending on the RF phase. This manifests in an abrupt drop of the electron density at $s(t)$. The instantaneous electron density n_e equals the ion density in the region **A**, $x < s(t)$. The electric potential difference is approximately zero, and the potential drop along the sheath only appears in region **B**. Lieberman shows that it is possible to find a time-averaged potential profile that is sustained by the ion density n_i and a virtual

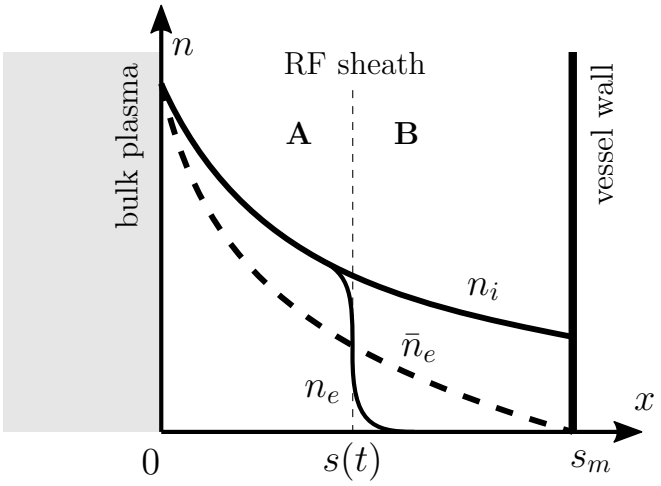

Figure 2.3: Schematic demonstrating the conditions in an RF sheath following [15]

(time-averaged) electron density profile $\bar{n}_e$. The point at which $\bar{n}_e = n_i$ defines the origin $x = 0$ and thereby the thickness of the RF sheath s_m.

As with the DC sheath, it is possible to evaluate the time-averaged potential drop along the RF sheath. An equilibrium is established when the ion flux equals the average electron flux:

$$< \frac{1}{4} n_s \bar{v}_e \exp\left(\frac{-e\left(\phi_1 \sin \omega t + \phi_{DC}\right)}{k_B T_e}\right) > = \; n_s u_s. \tag{2.7}$$

The term on the left-hand side is the (thermal) electron flux, with a sinusoidal perturbation of the electric potential. The <> brackets indicate the average over time. $\phi_{DC} - \phi_w$ is the potential difference that reduces the electric current through the RF sheath on average to zero. It can be shown [11, p.113] that Equation (2.7) is solved for:

$$\phi_{DC} = \frac{k_B T_e}{e}\left[\frac{1}{2}\ln\left(\frac{m_i}{2\pi m_e}\right) + \ln I_0\left(\frac{e\phi_1}{k_B T e}\right)\right],$$

assuming $T_i << T_e$. Here, I_0 is the zero-order modified Bessel function. The first term in the bracket is the already known potential drop along a DC sheath, Equation (2.1). The second term is the contribution from the RF oscillations. Because of $I_0 \geq 1$, the potential of the plasma is increased by ϕ_1. This phenomenon is known as a rectification process. In electronics, rectification processes are utilized to transform an oscillating signal to a static signal at a non-linear component like a diode. In a plasma, the sheath causes this. Figure 2.4 shows the normalized electric current flow through the RF sheath $\hat{\imath}$ for a particular parameter set against the RF phase φ_{RF}, following Equation (2.7). The ion current $\hat{\imath}_i$ is constant over time as the ions do not respond to the RF oscillations. The electron current $\hat{\imath}_e$ responds to the RF oscillations, but the sheath distorts the sinusoidal shape. Per definition, the electric current through the sheath is zero on average.

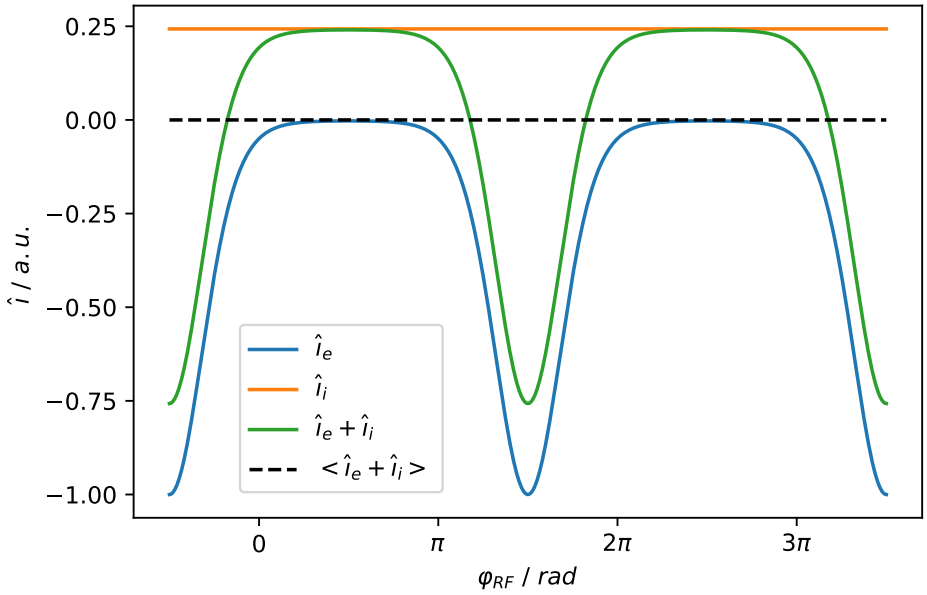

Figure 2.4: Normalized current flow through an RF sheath for $k_B T_e = 1\,\mathrm{eV}, m_i = 1\,\mathrm{u}$ and $\phi_1 = 3\,\mathrm{V}$

It is known that the RF sheath influences the I-V characteristic measured by a Langmuir probe. This is especially relevant in plasma, where an RF plasma source produces the plasma itself. Chen described this process in his lecture notes [12] as a flattening of the I-V characteristic, specifically around V_p. There are strategies to reduce this effect, for example, RF compensation. However, these are usually impracticable in the SOL of MCF devices due to the intermittent behavior of the plasma density. In the experiments discussed in the following chapters, such strategies to improve probe measurements were not applied. In the experiments at ASDEX Upgrade, Chapter 6, it is plausible to assume that the amplitude of the RF perturbations is small compared to the thermal potential drop along the probe sheath. In the experiments at IShTAR, Chapter 5, this is not necessarily the case. A discussion on the significance of the extracted parameters follows there.

2.4 Magnetized plasma

In the presence of a strong magnetic field $\vec{B}_0$, charged particles with velocity $\vec{v} = \vec{v}_\parallel + \vec{v}_\perp$ orbit around the magnetic field lines. The frequency and length scale associated with this is the cyclotron frequency $\omega_{c\sigma}$ and the gyroradius $r_{g\sigma}$, respectively:

$$\omega_{c\sigma} = \frac{q_\sigma B_0}{m_\sigma}, \qquad r_{g\sigma} = \frac{m_\sigma v_\perp}{q_\sigma B_0}. \tag{2.8}$$

The confinement of charged particles greatly restricts their motion across the magnetic field lines. This effect partially transfers to the macroscopic plasma, which then can be confined by external magnetic fields. This is the basis of magnetic confinement fusion. To describe phenomena in a magnetized plasma, it is often

beneficial to formulate physical relations in coordinate systems where one principal axis is oriented parallel to the background magnetic field. The other two principal axes then span a surface orthogonal to $\vec{B}_0$. Tensors $\vec{T}$, representing macroscopic plasma properties, can then be separated in a 1-D parallel $\parallel$ and a 2-D perpendicular $\perp$ component $\vec{T} = \vec{T}_\parallel + \vec{T}_\perp$. This decomposition considers that many physical properties of the plasma, for example, the electric conductivity, vary widely depending on the orientation of the discussed phenomena to the background magnetic field.

The confinement of particles by the magnetic field alters the sheath physics and, consequently, the response of Langmuir probes. Magnetic effects become relevant when the gyro radius becomes smaller than the characteristic length of the probe. At this point, the probe is exposed to charged particles originating only from a thin tube that extends along the magnetic field, as illustrated in Figure 2.5. Hutchinson

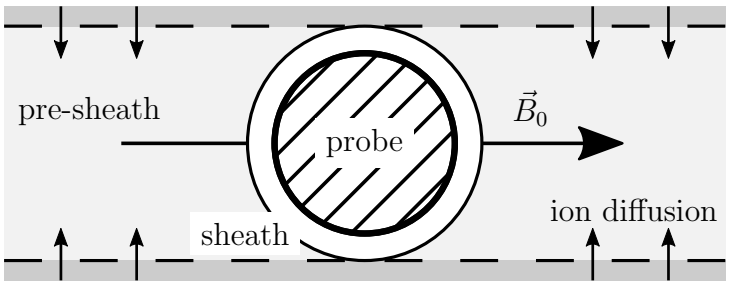

Figure 2.5: Schematic of a probe in a plasma with a strong background magnetic field following [13, p. 75]

discusses in chapter 3.3 of his book [13] that in this scenario, an ion diffusion flux from the surrounding plasma must flow into the tube and that the pre-sheath can extend up to the point where the magnetic field intersects the experimental vessel wall. Collisions in the pre-sheath of a magnetized plasma can generally not be neglected, and a precise derivation of a general probe characteristic is a complex problem. Conveniently, it was found that if the ion diffusion flux is high enough, the I-V characteristic of a Langmuir probe in a plasma with a background magnetic field was found to be not too different from a curve of a probe without a background magnetic field with two exceptions [13, p.77ff]. The first is that the collective area of the probe is not the entire probe surface but rather the projection of the probe along the magnetic field. The second is the scaling parameter that relates the plasma density at the sheath to the density in the (far away) bulk plasma to $f \approx 0.49$.

In the presence of a background ion flow $v_\parallel$ in a magnetized plasma, it is possible to combine two probes into a so-called Mach probe. Figure 2.6 shows a schematic of such a setup. The single probe was replaced by two probes that are biased independently with respect to the same (far away) reference potential, i.e., the vessel wall. The probes are separated, for example, by a dielectric (colored yellow), and each is exposed only to one side of the flux tube. In this example, probe 1 is exposed to an incoming ion flow. The potential drop required to accelerate the ions to the sound speed is reduced compared to the static case, and the scaling factor f_1 is larger. At probe 2, the potential drop along the pre-sheath has to be larger since the ions first have to be brought to rest before they accelerate toward the probe.

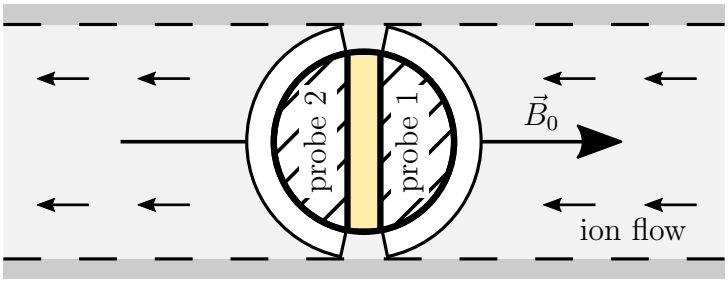

Figure 2.6: Schematic of a Mach probe in a plasma with a strong background magnetic field. Probe 1 is exposed to an incoming ion flow.

Consequently, f_2 is smaller. It can be shown [13, p.85] that:

$$f = \exp\left(-1 - 1.1M + (1 - \sqrt{\alpha})(0.31 + 0.6M)\right).$$

Here, $M = v_{\parallel}/c_s$ is the Mach number of the ion flow, and α is a term absorbing the ($\perp$) viscosity and diffusivity of the plasma. Again, it turns out that typically $\alpha \approx 1$ [13, p.86] and f reduces to:

$$f = \exp\left(-1 - 1.1M\right).$$

The Mach number is sign-sensitive, which is essential when calculating f for the two probes. Probe 1 is exposed to an inflow of ions with normalized velocity M, while probe 2 experiences an outflow with velocity -M.

2.5 Electromagnetic waves in plasma

Considering plasma as a region in space filled with electrically charged particles raises the question of how the plasma responds to perturbations in the electromagnetic field. The following section introduces how this question is typically addressed. The discussion here is restricted to small perturbations and represents the so-called cold plasma approximation, where particles have no kinetic thermal motion. The following text resembles chapter 6 of Bellan's book Fundamentals of Plasma Physics [10]. The electromagnetic dispersion relation is derived from Maxwell's equations and descriptions for the velocity of the charged particles.

Faraday's law is combined with Ampère's law to:

$$\nabla \times \left(\nabla \times \vec{E}\right) = -\frac{\partial}{\partial t}\left(\mu_0\left(\vec{J} + \varepsilon_0 \frac{\partial \vec{E}}{\partial t}\right)\right). \tag{2.9}$$

The current density is modeled as a flow of charged particles:

$$\vec{J} = \sum_{\sigma} n_\sigma q_\sigma \vec{v}_\sigma. \tag{2.10}$$

In the context of perturbation theory, where the fields are described as a zero-order component plus perturbations of decreasing amplitude $\vec{E} = \vec{E}^0 + \epsilon\vec{E}^1 + ...$, it can

be shown [10, p. 110] that, in the absence of collisions, the particles oscillate in a plasma with:

$$\vec{v}_\sigma^1 = \frac{iq_\sigma}{\omega m_\sigma}\left[E_\parallel^1 \vec{e}_z + \frac{\vec{E}_\perp^1}{1-\omega_{c\sigma}^2/\omega^2} - \frac{i\omega_{c\sigma}}{\omega}\frac{\vec{e}_z \times \vec{E}^1}{1-\omega_{c\sigma}^2/\omega^2}\right]. \tag{2.11}$$

Here, the perturbations are of the form $\exp(i\vec{k}\cdot\vec{r} - i\omega t)$. The superscript is dropped hereafter because $\vec{E}^1$ is the wave. The first term in the rectangular bracket represents the component without a magnetic field. The second term represents the generalized polarization drift, and the third is the generalized $\vec{E}\times\vec{B}$ drift. Equations (2.9), (2.10), and (2.11) can be combined into the wave equation:

$$\nabla \times \left(\nabla \times \vec{E}\right) = -\frac{1}{c_0^2}\frac{\partial^2}{\partial t^2}\left(\hat{\varepsilon}\cdot\vec{E}\right), \tag{2.12}$$

with the cold plasma dielectric tensor $\hat{\varepsilon}$:

$$\hat{\varepsilon} = \begin{bmatrix} S & -iD & 0 \\ iD & S & 0 \\ 0 & 0 & P \end{bmatrix}. \tag{2.13}$$

The matrix elements S, D, and P are:

$$R = 1 - \sum_\sigma \frac{\omega_{p\sigma}^2}{\omega(\omega+\omega_{c\sigma})}, \quad L = 1 - \sum_\sigma \frac{\omega_{p\sigma}^2}{\omega(\omega-\omega_{c\sigma})}, \quad P = 1 - \sum_\sigma \frac{\omega_{p\sigma}^2}{\omega^2},$$
$$S = \frac{1}{2}(R+L), \qquad D = \frac{1}{2}(R-L). \tag{2.14}$$

R, L, P, S, and D are typically called Stix parameters in recognition of the plasma physicist T.H. Stix [16].

Assuming harmonic oscillations gives $\partial/\partial t \to -i\omega$ and $\nabla \to i\vec{k}$ and Equation (2.12) becomes:

$$\left(\vec{N}\otimes\vec{N} - N^2\vec{I}\right)\vec{E} = -\hat{\varepsilon}\cdot\vec{E}, \tag{2.15}$$

where the refractive index $\vec{N} = c_0\vec{k}/\omega$ is introduced as the normalized wave vector $\vec{k}$. For a homogeneous plasma, it is possible to choose a coordinate system such that $\vec{N}$ lies in the x-z plane of a Cartesian coordinate system. Equation (2.15) becomes:

$$\begin{bmatrix} S - N^2\cos^2\theta & -iD & N^2\sin\theta\cos\theta \\ iD & S - N^2 & 0 \\ N^2\sin\theta\cos\theta & 0 & P - N^2\sin^2\theta \end{bmatrix} \cdot \begin{bmatrix} E_x \\ E_y \\ E_z \end{bmatrix} = 0. \tag{2.16}$$

Here, θ is the angle between $\vec{B}_0$ and $\vec{N}$. Nontrivial solutions for Equation (2.16) exist when the determinant of the matrix vanishes:

$$AN^4 - BN^2 + C = 0, \tag{2.17}$$

with:

$$\begin{aligned} A &= S\sin^2\theta + P\cos^2\theta, \\ B &= (S^2 - D^2)\sin^2\theta + PS(1+\cos^2\theta), \\ C &= P(S^2 - D^2). \end{aligned} \tag{2.18}$$

Equation (2.17) is the plasma dispersion relation and a quadratic equation with respect to N^2. The two solutions are:

$$N_\pm^2 = \frac{B \pm \sqrt{B^2 - 4AC}}{2A}. \tag{2.19}$$

The subscript is either + or − depending on how ± is used. Notice that any solution of N^2 is real-valued since $B^2 - 4AC$ is always positive, provided that θ is real-valued.

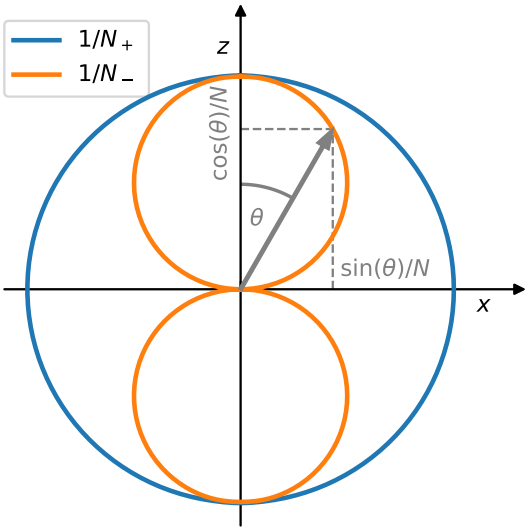

Figure 2.7: Wave normal surface of the compressional N_+ and shear N_- Alfvén wave

For a given frequency in a two-species plasma, electrons, and a single ion species, with known parameters n_e, n_i, and B_0, the solutions reduce to $N^2(\theta)$. It is possible to present $1/N = c_{ph}/c_0$, the normalized phase velocity, in polar form. In 3-D, the solutions form surfaces that are called wave normal surfaces. Figure 2.7 shows an example with parameters realistic for a modern MCF experiment with deuterium: $n_e = n_i = 1 \times 10^{19}\,\mathrm{m}^{-3}$, $B_0 = 2.5\,\mathrm{T}$, $q_i = -q_e = e$, and a frequency of $f = 100\,\mathrm{kHz}$. These particular solutions are named compressional and shear Alfvén wave where:

$$N_+^2 \approx S \approx 1 + \frac{c^2}{v_A^2}, \qquad N_-^2 \approx \frac{PS}{S\sin^2\theta + P\cos^2\theta}, \tag{2.20}$$

with the Alfvén velocity $v_A \approx B_0/\sqrt{\mu_0 m_i n}$. It is apparent that $1/N_+$ forms an ellipse, $1/N_-$ a dumbbell shape, and that $1/N_+ \geq 1/N_-$ for all θ. Notice that N_- has a resonance around $S\sin^2\theta + P\cos^2\theta = 0$, where it diverges. Due to its relation

to the wave's phase velocity, it is common to call the outer solution "fast wave" and the inner "slow wave".

If the parameters n_σ, B_0, or f change, the solutions change, and the wave normal surfaces deform. If the parameter changes are small, the wave normal surfaces typically deform slightly while their qualitative shape is maintained; however, when certain boundaries are crossed, the nature of the solution changes. All possible solutions to the dispersion relation Equation (2.17) are displayed in the so-called CMA diagram, shown in Figure 2.8, named after Clemmow, Mullaly, and Allis to acknowledge their contributions to the field. The horizontal axis of the CMA

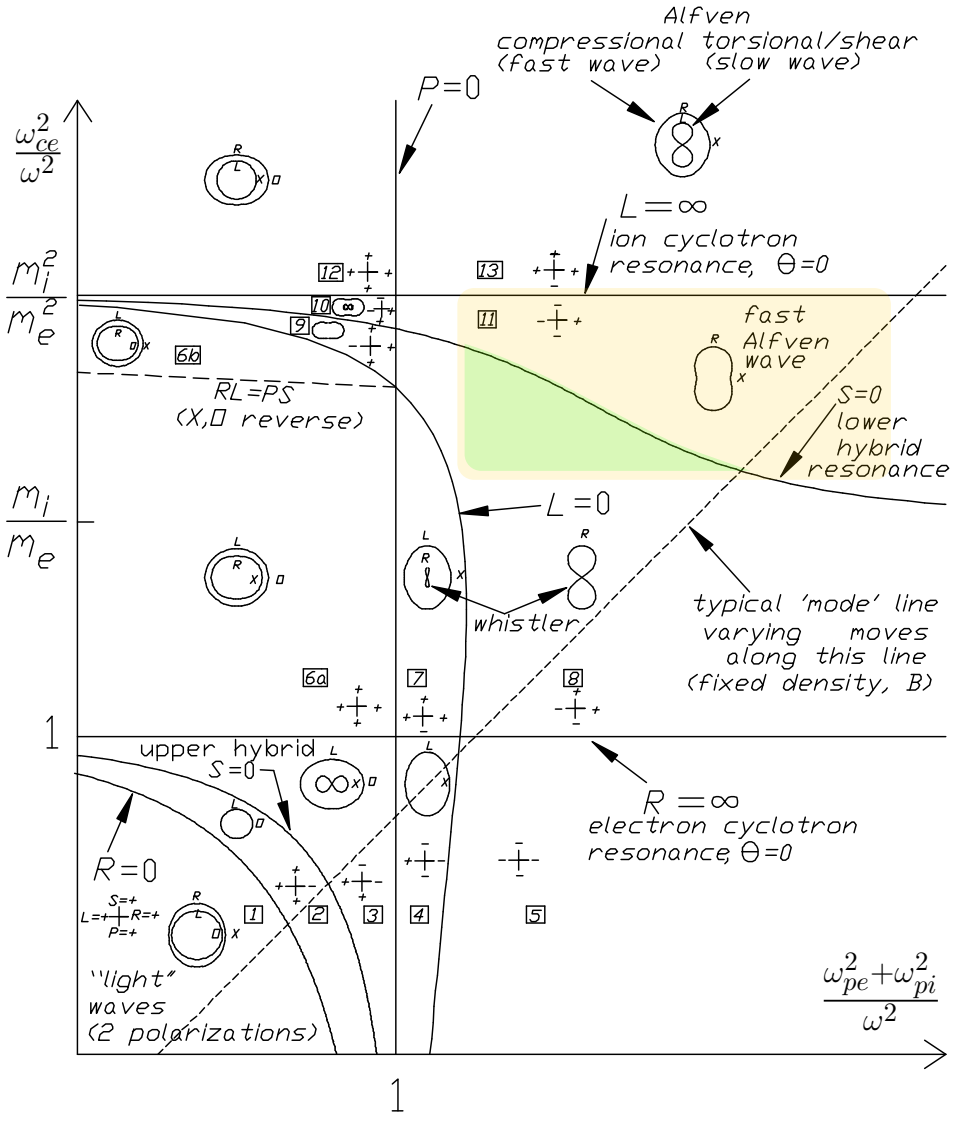

Figure 2.8: CMA diagram from [10, p. 189](modified). ICRF region highlighted in yellow, region of propagating slow waves in green.

diagram is in units $(\omega_{pe}^2 + \omega_{pi}^2)/\omega^2$, therefore depending on the plasma density n_σ. The vertical axis is in units ω_{ce}^2/ω^2, therefore depending on the magnetic field strength B_0. The diagram is divided into 13 regions bound by lines at which the

qualitative nature of the wave normal surfaces changes. Representative wave normal surfaces are drawn into the regions, indicating the qualitative nature of the solutions in the entire region. Notice that some regions contain only one or no wave normal surfaces. Notice that in some regions, there are only one or no wave normal surfaces. Here, either one or both solutions for N^2 are negative, implying that N is imaginary and the wave is evanescent. The approximate ICRF region in a modern tokamak is highlighted in the diagram with a yellow rectangle. The subspace of propagation ICRF slow waves is highlighted in green.

The CMA diagram can be read in two ways. Either it is used to tell which propagating solutions exist in a plasma with fixed n_σ and B_0 for a wave with arbitrary frequency, or it is used to tell how a wave with fixed frequency propagates in a plasma with variable n_σ and B_0. In the former case, the solutions are restricted to points along a (dashed) line at 45° where the position of the line is defined by n_σ and B_0. The latter interpretation presents the CMA diagram as a pond of plasma where n_σ increases along the horizontal and B_0 along the vertical axis. The CMA diagram shows every propagating solution to the dispersion relation in both cases.

As will become apparent in the later chapters, resonances $N \to \infty$ are of major relevance to this work. Equation (2.19) implies that this happens in two cases: B becoming infinite or A approaching zero. B becomes infinite at the cyclotron resonances, R or $L \to \infty$, the horizontal lines in the CMA diagram. The case $A = S\sin^2\theta + P\cos^2\theta = 0 \Leftrightarrow \tan^2\theta = -P/S$ has real-valued (propagative) solutions for θ whenever P and S have opposite signs. This is true in regions 3, 7, 8, 10, and 13 of the CMA diagram. These regions always contain a wave normal surface of the dumbbell type since it implied $n \to \infty$ at the cross-over point. In [10, p. 203ff], it is shown that solutions around this point are (nearly) electrostatic waves, meaning $\nabla \times E \approx 0$. When launched from a point-like source, these waves produce a conical field structure that opens up along the background magnetic field. For

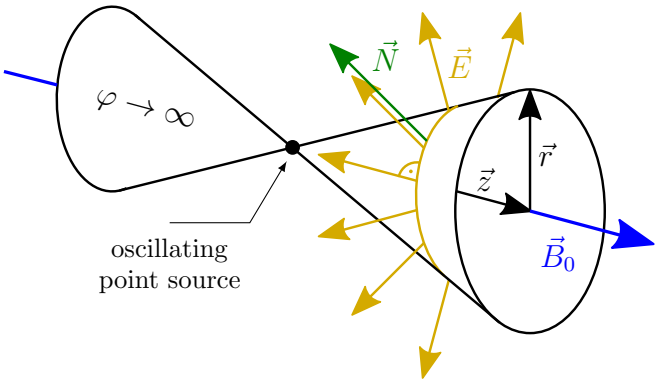

Figure 2.9: Schematic of a RC following [10, Fig. 6.4]

clarity, an illustration of these so-called resonance cones, hereafter abbreviated as RCs, is shown in Figure 2.9. The opening angle of these cones is such that:

$$\tan\theta_c = r/z = \pm\sqrt{-S/P}, \tag{2.21}$$

and $\vec{E}$, as well as $\vec{N}$, are (anti)parallel to the normal vector of the cone. RCs are

typically called slow waves because they are a subset of the dumbbell solution type. However, the assignment becomes ambiguous in region 8 of the CMA diagram, which contains only one solution. This makes the distinction between fast and slow, in principle, obsolete. Since RCs are quasi-electrostatic waves with a negligible magnetic field component, the electric field can be expressed as:

$$\vec{E} = -\nabla\varphi,$$

where φ is the oscillatory electric potential.

It is possible to show [10, p.206] that the electric potential diverges on the cone's surface within the cold plasma approximation. In this work, the type of RCs in the ICRF region, the green-colored region in the CMA diagram, are relevant. Here, they are called lower hybrid RCs. The following approximations are restricted to these. In most of this region $\omega_{ci} << \omega << \omega_{pe}, \omega_{ce}$ applies, and $\tan\theta_c$ can be approximated as:

$$\tan^2\theta_c = -\frac{S}{P} \approx \left(\omega^2 - \omega_{lh}^2\right)\left(\frac{1}{\omega_{pe}^2} + \frac{1}{\omega_{ce}^2}\right), \tag{2.22}$$

where $\omega_{lh}/2\pi$ is the lower hybrid resonance frequency:

$$\omega_{lh}^2 = \omega_{ci}^2 + \frac{\omega_{pi}^2}{1 + \frac{\omega_{pe}^2}{\omega_{ce}^2}}. \tag{2.23}$$

Specifically, when the plasma density is relatively low $\omega_{lh} << \omega$ and $\omega_{pe} << \omega_{ce}$, then:

$$\tan\theta_c \approx \frac{\omega}{\omega_{pe}}. \tag{2.24}$$

The previous discussion implies an isotropic density distribution and a constant magnetic field in the z-direction. In realistic experiments, in particular, in the outer edge of fusion-related experiments, this does not apply. Here, the background magnetic field is curved, and strong density gradients are observed.

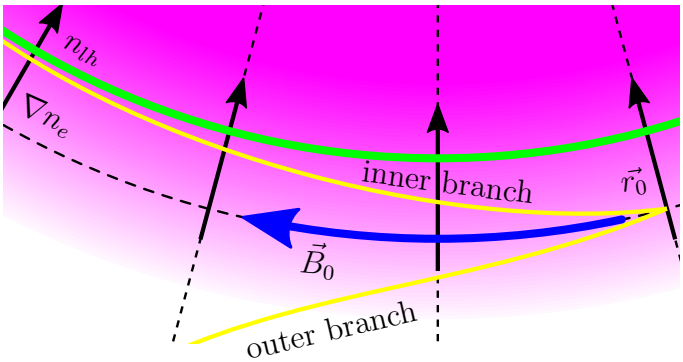

Figure 2.10: Schematic of a lower hybrid RC in curved $\vec{B}_0$ with $\nabla n_e \neq 0$

Without strict mathematical proof, it is argued that RCs propagate along the curved $\vec{B}_0$ with varying θ_c as the plasma density varies. A conceptualized illustration of this is shown in Figure 2.10. For simplicity, the problem description is reduced to a polar scenario with increasing density towards the center (purple) and a background magnetic field in the φ direction (blue). The line of argument is the following: If a RC (yellow) exists at some point $\vec{r_0}$ in the plasma, it opens up along the background magnetic field with an angle that is determined by the plasma density at that point $\theta_c(n(\vec{r_0}))$. When a section of the RC enters a region with lower or higher plasma density, the opening angle increases or decreases respectively, based on the opening angle at that point. The RCs get distorted by the density profile. Suppose the density increases continuously towards the center. In that case, the outer branch of the RC leaves the plasma while the inner branch propagates inwards until the opening angle approaches zero when $\omega = \omega_{lh}$, see Equation (2.22). That density (cyan) is called lower hybrid resonance density n_{lh}. Assuming $n_e = n_i$ in Equation (2.23) yields:

$$n_{lh} = \frac{m_e \varepsilon_0}{e^2} \frac{\omega_{ce}^2 \left(\omega_{lh}^2 - \omega_{ci}^2\right)}{\omega_{ci} \left(\omega_{ci} - \omega_{ce}\right) - \omega_{lh}^2}, \tag{2.25}$$

where $\omega_{ce} + \omega_{ci} \approx \omega_{ce}$ might be used.

Chapter 3

Experimental Framework

An experiment is a (measurement) process that is carried out to test a hypothesis. The experimental procedure can be straightforward, such as measuring some object size with a ruler, or it may require sophisticated measurement tools and models to interpret the obtained data. Langmuir probes are an example of the latter. In natural science and engineering, experiments typically consist of the object to be probed, the measuring devices that probe the object's parameters, and the components that form the experimental infrastructure. Together, these make the experimental framework. It is typically advantageous to consider the different aspects of the experimental framework when an experiment is conceived. The object to be probed places requirements on the measurement apparatus, and from a practical point of view, it needs to be possible to build and operate the experiment. This chapter introduces the experimental framework relevant to this work, and implications drawn from it are discussed.

3.1 ASDEX Upgrade

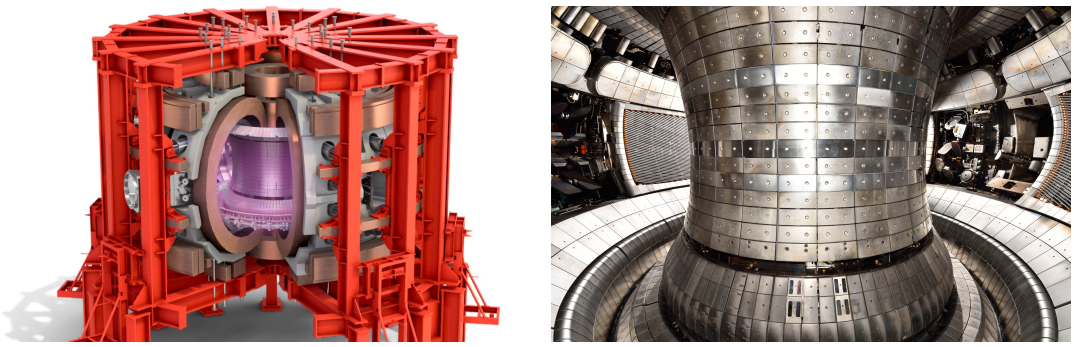

Figure 3.1: **(left)** Schematic and **(right)** picture of the inside of the ASDEX Upgrade tokamak [17],[18]

As motivated in the introduction, Chapter 1, the experimental framework is the SOL of a reactor-relevant MCF experiment. Here, this is the SOL of the Axial Symetrix Divertor EXperiment (ASDEX) Upgrade, a tokamak experiments oper-

ated at the Max-Planck-Institute of Plasma Physics in Garching bei München, Germany. Figure 3.1 shows a schematic and a picture of ASDEX Upgrade (AUG). Although AUG was never built to perform experiments with D-T fusion reactions, it is often considered a scaled-down version of a future fusion reactor. Experiments are typically performed with deuterium, and many plasma parameters and the power flows in AUG are in the order of reactor-relevant values. Over the past three decades, AUG addressed different topics in MCF research and contributed to the design of ITER. Reviews from Kallenbach [19] and Stroth [20] provide an overview of recent studies at AUG.

The toroidal shape of a tokamak suggests a set of coordinates (r, ϕ, θ), where r is the minor radius, ϕ is the toroidal angle, and θ is the poloidal angle, as shown in Figure 3.2. Besides these, cylindrical coordinates (R, ϕ, z) are used commonly.

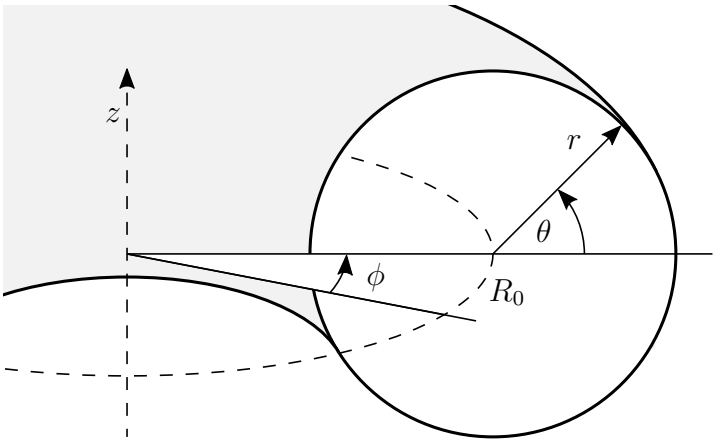

Figure 3.2: Schematic showing coordinates (r, θ, ϕ) in a torus

Magnetic confinement in a tokamak is achieved by creating a background magnetic field $\vec{B}_0$ that wraps around the torus. The twisted magnetic field consists primarily of two components: the toroidal and the poloidal field components . The toroidal component is produced by multiple D-shaped magnetic field coils that encircle the torus. The toroidal field decays with increasing distance to the z-axis because of the circular arrangement of the coils. The poloidal component is created by a large toroidal electric current in the plasma. The so-called plasma current I_p is induced with a cylindrical transformer that is located inside the torus hole. Besides this, tokamaks are typically equipped with additional magnetic field coils to realize sophisticated magnetic geometries. All components together create the background magnetic field $\vec{B}_0$. An example of the magnetic field profiles at $\theta = 0$ (or equivalent $z = 0$) in AUG is shown in Figure 3.3.a. In tokamaks, it is often appropriate to assume axial symmetry around the z-axis as a first-order approximation, and it is redundant to specify the ϕ coordinate. The toroidal component of the background magnetic field B_ϕ shows the mentioned decay towards larger distances from the origin. The poloidal component B_θ changes sign at the magnetic axis, considering that the toroidal electric current creates it. The toroidal field is the dominant component of the background magnetic field, and the designation high or low field

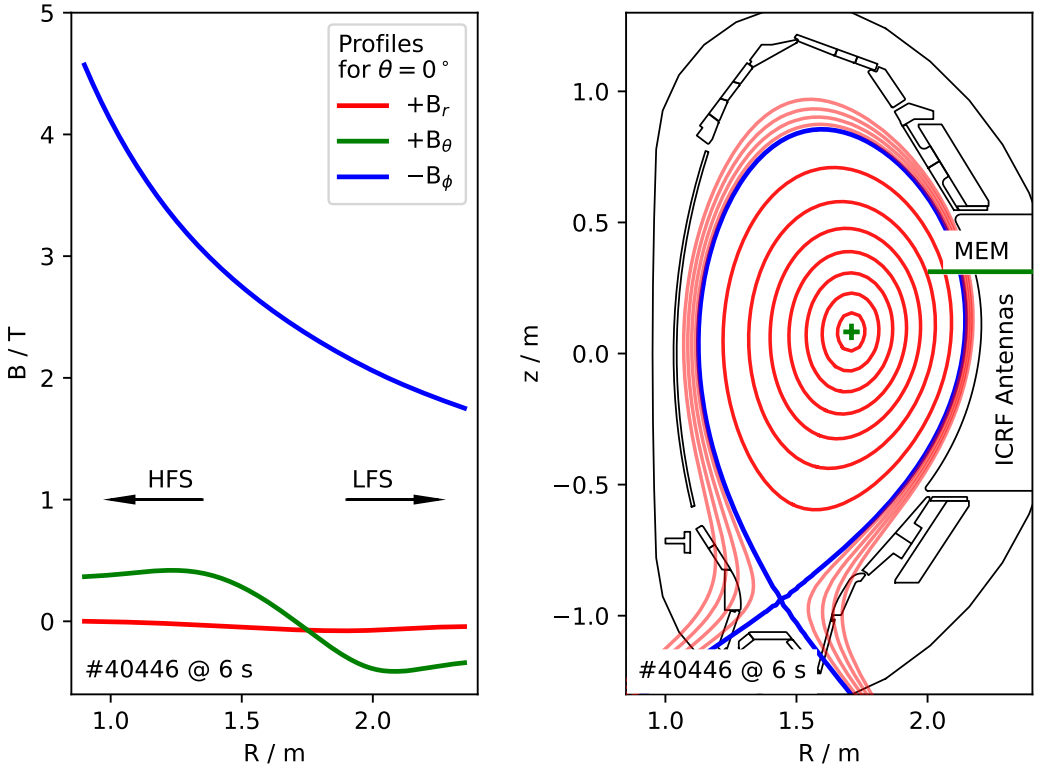

Figure 3.3: **(left)** Profiles of magnetic components for $\theta = 0$ **(right)** Poloidal cross-section of AUG with flux surfaces and separatrix

side (HFS or LFS) is used to differentiate between regions with smaller or larger R, respectively.

Figure 3.3.b shows the poloidal cross-section of AUG together with several poloidal flux surfaces in red and the separatrix in blue. Flux surfaces are surfaces where $\vec{B}_0 \cdot \vec{n} = 0$ everywhere, with $\vec{n}$ being the surface normal vector. It is common to define a normalized coordinate ρ_{pol} for the flux surfaces such that it is zero at the magnetic axis and unity at the separatrix. The magnetic axis is the flux surface in the core that encloses an infinitesimal volume. It is highlighted with a small green + in the Figure. The separatrix separates the region of closed flux surfaces from the region where the magnetic field lines intersect with the vessel wall. At AUG [21]:

$$\rho_{pol} = \sqrt{\frac{\Psi - \Psi_a}{\Psi_s - \Psi_a}}. \tag{3.1}$$

Here, Ψ is the poloidal magnetic flux defined as:

$$\Psi = \int_S \vec{B}_0 \cdot d\vec{S}, \tag{3.2}$$

where S is the ring-shaped cross-section of the particular flux surface at $z = z_a$. The indices s and a refer to the separatrix and the magnetic axis, respectively. At

AUG, the magnetic field is reconstructed from different magnetic diagnostics with the CLISTE code [22].

The confinement region $\rho_{pol} \leq 1$ in a tokamak is the volume where the fusion reaction occures in a future reactor. It is characterized by a hot and dense plasma. Exemplarically, the electron density n_e and temperature T_e profiles in AUG at a specific time t during an experimental sequence, called discharge and referenced with a unique five-digit number, are shown in Figure 3.4. In contrast to the confinement region, the SOL $\rho_{pol} > 1$ is characterized by steep gradients in the plasma parameters. The values are taken from the integrated data analysis (IDA) [23] and plotted against ρ_{pol}. The SOL contains the plasma-facing components (PFC), the

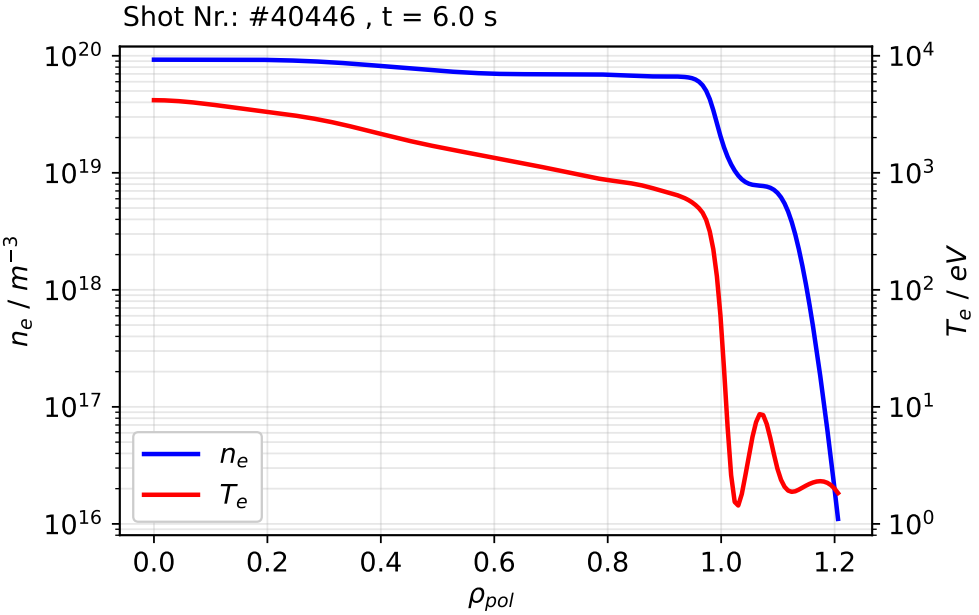

Figure 3.4: Profiles of n_e, and T_e in AUG against ρ_{pol} for discharge #40446 at $t = 6\,\mathrm{s}$ from the integrated data analysis

components of the experiment that are exposed to the plasma directly. This includes, in particular, the ICRF antennas and other components, i.e., the divertor. The divertor is the region in a tokamak where most open field lines intersect the PFC. Operating an MCF experiment with a divertor has been shown to increase its overall performance significantly. In AUG, the complex-shaped region in the bottom of the poloidal cross-section in Figure 3.3.b is usually used as the divertor. Other divertor concepts exist, and AUG is currently updated to study alternative scenarios with a new upper divertor [24].

3.2 Plasma heating

The plasma in AUG is created and maintained by four plasma heating techniques. They exploit different physical mechanisms of how energy is transferred from outside the tokamak into the plasma. The four techniques are ohmic heating, heating by

neutral beam injection (NBI), electron cyclotron resonance heating (ECRH), and ion cyclotron range of frequencies (ICRF) heating. The ohmic heating transfers energy to the plasma via the plasma current that flows in the plasma. The electrical conductivity of the plasma is large but not infinite, and driving the plasma current leads to a power flow from the transformer into the plasma. However, the plasma's electric resistance drops when the temperature increases and ohmic heating becomes less effective. The NBI injects electrically neutral high-energetic particles into the vessel. These are ionized in the plasma, and their kinetic energy is transferred to the plasma via collisions with the other plasma particles. The ECRH and ICRF heating are conceptually based on injecting electromagnetic waves with frequencies in the range of the electron and the ion cyclotron frequency ω_{ce} and ω_{ci} into the plasma. However, the method of how the waves are injected into and absorbed by the plasma differs for ECRH and ICRF heating. The ECRH system operates in AUG at $f = 105\,\mathrm{GHz}$ or $140\,\mathrm{GHz}$. The microwave power is transferred to the torus via hollow waveguides. Inside the vessel, the waveguides terminate, and the microwave signals are launched onto metallic mirrors that redirect the power into the plasma. The gyrating electrons absorb the launched waves, subsequently distributing the injected power to all plasma particles via collisions.

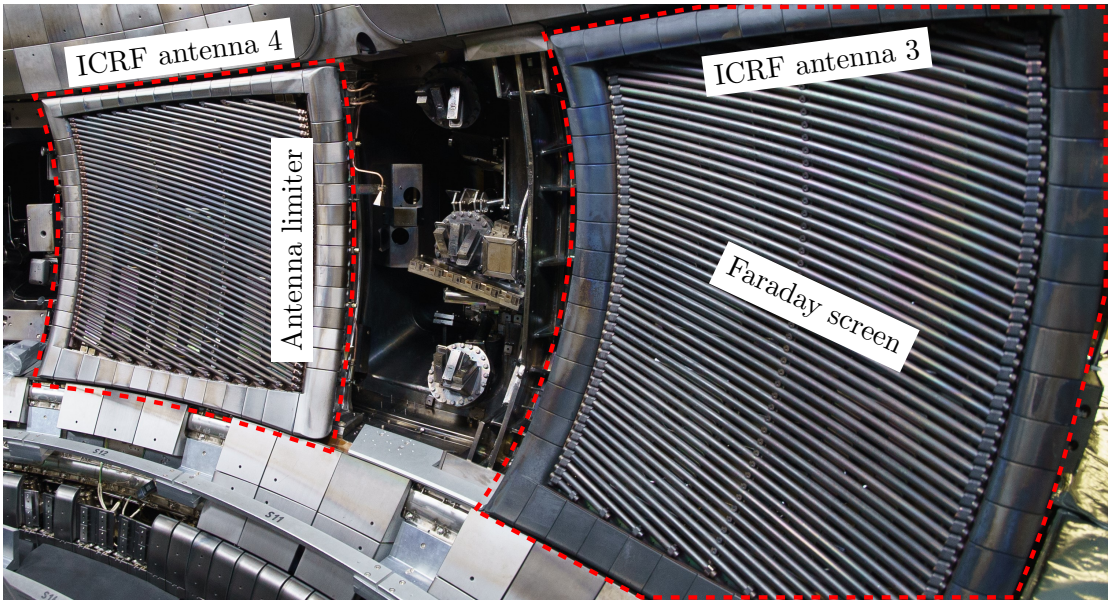

Figure 3.5: Photograph of ICRF antenna 4 and 3 in the AUG tokamak [25]

In ICRF heating, it is possible to exploit different wave absorption mechanisms. These so-called heating schemes are explained in detail elsewhere [6]. A typical heating scheme for AUG is hydrogen minority heating. Here, a small amount of hydrogen is added to the deuterium gas. The frequency of the ICRF system matches $\omega_{ci}^{H}/2\pi \approx 15\,\mathrm{MHz/T}$ at some point in the plasma, and the wave gets absorbed by the hydrogen ions. The vacuum wavelength of these RF waves is for $B_0 = 2\,\mathrm{T}$ ten meters and comparable to the size of the tokamak. While the wavelengths in the

plasma are typically shorter, a full wave description is nevertheless necessary when determining the distribution of the RF fields through the vessel. The RF power is launched into the vessel from up to four antennas that are embedded in the torus's outer wall. Figure 3.5 shows a photograph of AUG's ICRF antennas 3 and 4.

The main components of an antenna are a metal box with two coaxial feedthroughs where the RF power enters the box (not visible), a number of folded steel straps that are connected to the coaxial feedthroughs, a Faraday screen suppressing RF electric fields that are parallel to the background magnetic field, and the antenna limiter that protects the antenna against the heat flux from the plasma. Antenna 2 and Antenna 4 (A2 and A4) differ from Antenna 1 and Antenna 3 (A1 and A3). A2 and A4 are of the relatively new type implemented to prevent increased plasma contamination during ICRF heating; see Chapter 1. They contain three poloidally oriented steel straps. A1 and A3, on the other hand, contain only two straps and are smaller in size. The antenna straps are for all antennas located behind the inclined Faraday screen inside the antenna box. It is possible to identify some of the straps of A4 behind the Faraday screen in Figure 3.5. The radially protruding antenna limiter consists of graphite tiles, hereafter designated as limiter tiles, coated either with tungsten at A2 and A4 or boron at A1 and A3. The reduced fields at the antenna periphery on the three strap antennas A2 and A4 enabled the unhindered operation of AUG with tungsten-coated limiter tiles. This is not the case for the two strap antennas A1 and A3, hence the low-Z coating.

3.3 Diagnostics

In order to address questions in the research, it is typically required to determine many different parameters in and around a tokamak. AUG is equipped with many diagnostic systems to measure most of the relevant physical parameters. Relevant to this work are:

- probes that determine the magnetic field geometry and the plasma current;
- active probes to determine the local plasma parameter, e.g., Langmuir probes;
- spectroscopic systems to determine the plasma parameter, e.g., Li-Beam diagnostic.

Specifically, the core, the divertor, and the plasma edge, the transition region between the confinement region and the SOL are covered intensively with probes because of their elevated relevance in future reactors. Compared to that, the section of the SOL relevant to this work around the ICRF antennas, particularly the region in the limiter shadow, is not well diagnosed. An exception is the so-called Mittelebenenmanipulator (MEM), translated from German to English as mid-plane-manipulator. It is a pneumatically driven apparatus used to plunge probes radially from the LFS into the torus. Consider the green line in Figure 3.3.b). To protect the probes from eroding in the plasma, they are typically embedded in a solid

tungsten-coated graphite rod, the probe head. In order to reduce the heat load on the probe head, the plunge sequence is typically completed in less than 200 ms.

Depending on the research question, several probe heads equipped with different probes are available at AUG. Figure 3.6 shows the so-called ball-pen probe head [26]. It contains seven probes overall. Four are directly exposed to the plasma and typically operated independently as Langmuir or in pairs as Mach probes, reconsider Sections 2.2 and 2.4). The three spherical probes are indented. In a magnetized plasma, the electron-to-ion saturation current ratio becomes approximately unity, and the probe floats near the plasma potential. This allows the measurement of plasma potential perturbations [26].

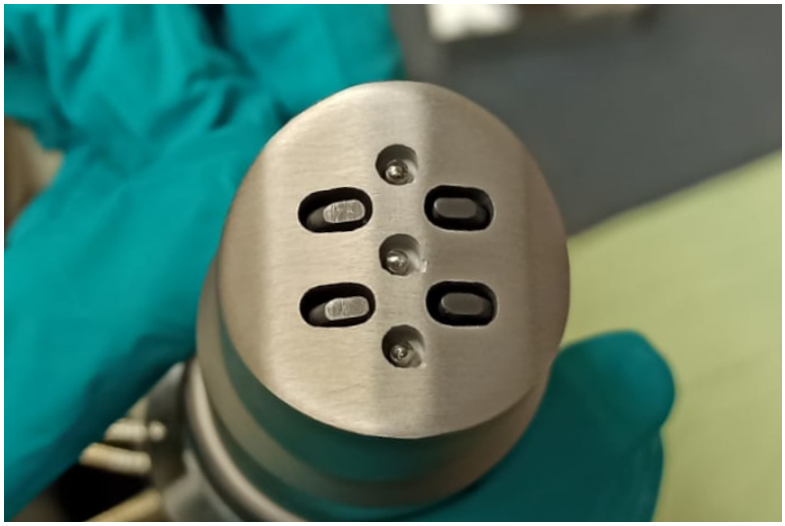

Figure 3.6: Ball-pen probe head for the AUG mid-plane manipulator

3.4 Implications on the problem definition

Considering the theoretical description in Chapter 2 and the preceding discussion allows to refine this work's problem definition. For this, a result of Chapter 4 is anticipated:

- simulations indicate that ICRF slow waves manifests in plasma with densities below the lower hybrid resonance density n_{lh} predominantly as RCs;
- a divergence condition at the RF source/plasma boundary favors the excitation of RCs over other ICRF slow wave modes;
- studying the propagation of the ICRF slow wave means, therefore, studying the propagation of lower hybrid RCs in this work.

From Section 2.5, it is known that lower hybrid RCs expand along the background magnetic field vector $\vec{B}_0$ with an opening angle such that $\tan\theta_c = \pm\sqrt{-S/P} \approx \omega/\omega_{pe}$. The approximation ω/ω_{pe} highlights that the opening angle depends, in

the parameter range of applicability $\omega_{ci}, \omega_{lh} << \omega << \omega_{pe} << \omega_{ce}$, on the wave's angular frequency and inverse on the plasma density. The plasma density in front of the ICRF antenna is in AUG usually relatively high, and θ_c is consequently relatively small at the for AUG typical ICRF of $f_1 = 30\,\mathrm{MHz}$ to $36.5\,\mathrm{MHz}$. This is shown in Figure 3.7, where the RC opening angle is plotted against the electron plasma density n_e for different background magnetic field amplitudes B_0 in a deuterium plasma.

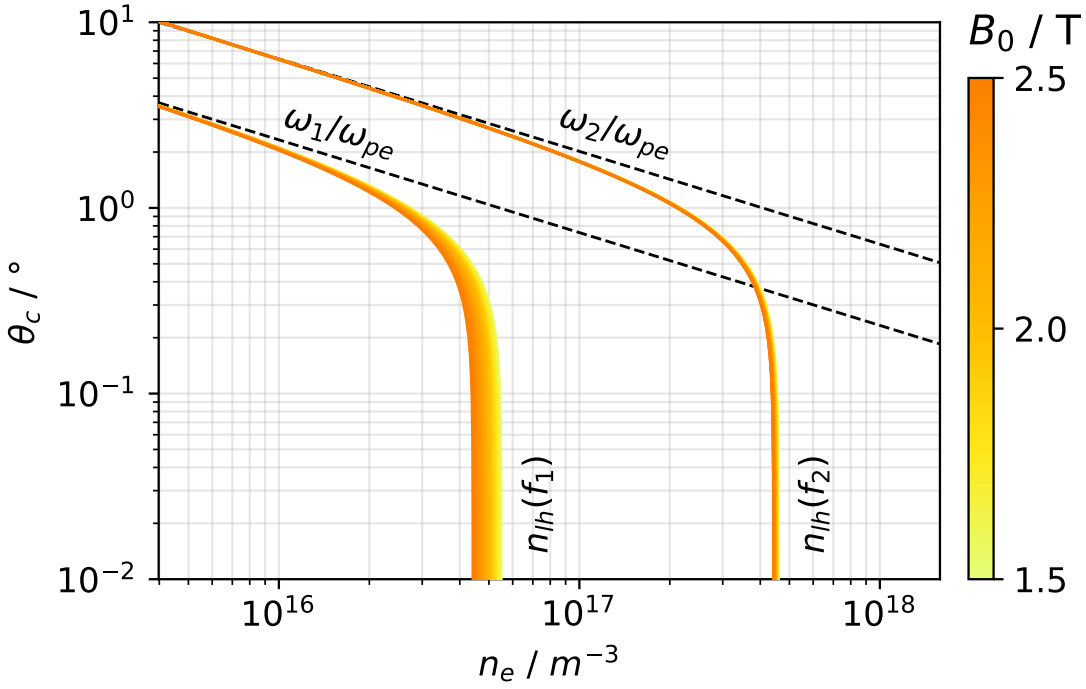

Figure 3.7: RC opening angle θ_c for $f_1 = 36.5\,\mathrm{MHz}$ and $f_2 = 100\,\mathrm{MHz}$

It is apparent that θ_c approaches zero at the lower hybrid resonance density n_{lh}. Further. it is visible that the approximation ω/ω_{pe} loses applicability at smaller opening angles. Performing experiments with the ICRF frequencies typical for AUG was found to be difficult. The plasma density gradient in the SOL in front of the ICRF antenna limiter is steep, and the plasma density typically surpasses the lower hybrid resonance density quickly. If RCs exist in this region, their opening angle is likely small, and the RF signals are restricted to a narrow layer. The RCs consequently terminate with the background magnetic field lines at the next possible PFC, and studying propagating RCs in the SOL is impeded. The problem is solved by increasing the frequency of the waves. The opening angle of the RCs increases, and the signals penetrate deeper into the SOL. Changing the wave's frequency selects a different solution from the cold plasma dispersion relation. However, it is argued that the qualitative findings remain conclusive if the solution stays within the same region (here, region 8) of the CMA diagram. Increasing the frequency has further benefits. As will become apparent in Chapter 6, the RCs are launched into the SOL from individual limiter tiles with a specific setup. The electric impedance

of the setup depends on the wave's frequency, and it is plausible that the RC's amplitude is larger at higher frequencies due to better coupling. Another aspect that benefits from a higher radio frequency is the plasma diagnostic, specifically the Langmuir probe system. To connect the findings with the dispersion relation, it is required to determine the plasma parameters, specifically the plasma density. In the antenna limiter SOL, this can be obtained with Langmuir probes at the MEM. However, the electronics available to measure the Langmuir probe characteristic were designed to probe regions with relatively high plasma densities. By increasing the wave's frequency, the region of interest is shifted towards higher plasma densities, and the requirements on the diagnostic apparatus are relaxed. Most simulations and experiments discussed in the following chapters are performed with frequencies of about $f_2 = 100\,\mathrm{MHz}$. The frequency satisfies the discussed aspects while not being too far from the typical ICRF frequency range used in AUG. The physics remains the same, and it is possible to utilize most of the equipment available for ICRF-related studies at AUG.

Chapter 4

ICRF slow wave modelling with RAPLICASOL

This section describes simulations that were performed with the RAPLICASOL procedure [27]. The intention is to investigate the excitation of the ICRF slow wave and to derive a set of principles that help to describe the experimental findings in Chapters 5 and 6.

The procedure RAPLICASOL, an abbreviation for radio frequency wave coupling for ion cyclotron antenna in scrape-off-layer, is an implementation in the FEM solver COMSOL Multiphysics. It approximates the electromagnetic field that is generated by an antenna in a stationary cold magnetized plasma. The program solves the electromagnetic wave equation (2.12). It is consequently expected that the field is defined by superpositions of the fundamental waves that were discussed in Section 2.5. In the past, RAPLICASOL was typically used to model the RF fields around different models of the AUG ICRF antennas with a focus on plasma with densities above the lower hybrid resonance density. Recently, the procedure was modified to model ICRF slow waves as well [28]. In this work, RAPLICASOL is used to compute the electromagnetic field distribution around different sources with comparatively simple contours in plasma with densities below the lower hybrid resonance density.

Section 4.1 introduces the framework of a RAPLICASOL simulation. Section 4.2 describes simulations in two dimensions (2-D) without variations in the z-direction. 2-D simulations simplify the description, and the results are easier to interpret. They provide insights into how the ICRF slow wave is excited and show relevant phenomena. Another advantage of 2-D simulation is the reduction of computational resources that allow high mesh resolutions. In Section 4.3, simulations in three dimensions (3-D) reveal insights that remain hidden in the 2-D description. In particular, the different excitation forms for 3-D simulations compared to 2-D simulations have implications. The conducted simulations attempt to contribute to a deeper understanding of the relevant mechanisms. They focus on a qualitative description and are, therefore, typically not reflecting realistic conditions in a SOL.

4.1 Framework of a simulation

A RAPLICASOL simulation consists of at least one domain that is surrounded by a so-called perfectly matched layer (PML) [29]. This is shown schematically in Figure 4.1 in 2-D for clarity. The simulation domains are regions (surfaces in

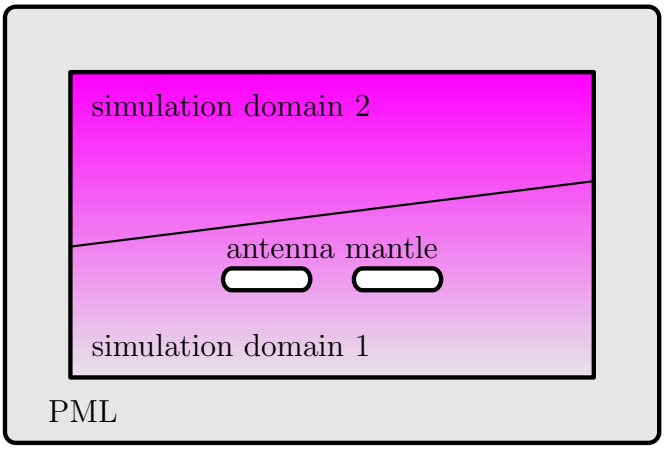

Figure 4.1: Concept of a RAPLICASOL simulation

2-D or volumes in 3-D) equipped with a dielectric tensor $\boldsymbol{\varepsilon}$ that represents the cold magnetized plasma (Equation (2.13)). A signal source is typically added by subtracting a (simplified) geometrical model of an antenna from the simulation domain. The simulation is then excited via boundary conditions imposed on the edge of the hereby-created antenna mantel. The PML is an established method to emulate a simulation domain that extends to infinity. It is an artificial layer surrounding the simulation domain to absorb incoming radiation without creating reflections at the interface. This is achieved by gradually stretching the space coordinates within the PML to the imaginary axis. However, there is a drawback regarding PMLs when it comes to ICRF slow wave simulations. RCs that are expected to appear in ICRF slow wave simulations were observed to be amplified instead of being damped by the PML. Constructing a PML that copes with such media is ongoing work and has been discussed, for example, in [30]. Based on previous work [31], Usoltceva showed that, for certain conditions, it is possible to simulate RCs within RAPLICASOL [28].

Another aspect that complicates simulations of ICRF slow waves is the diverging fields that can appear when RCs form. It is, from both a computational and a physical point of view, beneficial to restrict the infinite fields by adding a friction term, in the form of collisions, to the model. Brambilla described in his book [32, p. 169f] how to implement collisions between charged particles and neutrals, and electrons and ions as long as ω is high enough that the ions can be considered stationary. In the following simulations, this condition is fulfilled as $\omega > \omega_p i$ always. The collisions are implemented by replacing ω with $\omega + i\nu$ in the so-called mobility tensor $\vec{\mathcal{M}}_\sigma$. Here, ν is the collision frequency. In Brambilla's description, the mobility tensor is the matrix in the linear map $\vec{v}_\sigma = \vec{\mathcal{M}}_\sigma \cdot \vec{E}$, which describes the

relation between the electric field and the velocity of the particles. This results in the transformation of the Stix parameters to:

$$R = 1 - \sum_{\sigma} \frac{\omega_{p\sigma}^2}{\omega(\omega + i\nu + \omega_{c\sigma})}, \quad L = 1 - \sum_{\sigma} \frac{\omega_{p\sigma}^2}{\omega(\omega + i\nu - \omega_{c\sigma})}, \\ P = 1 - \sum_{\sigma} \frac{\omega_{p\sigma}^2}{\omega\left(\omega + i\nu\right)}. \tag{4.1}$$

To estimate an appropriate collision frequency, it is necessary to assess the plasma parameters of the experiment, identify the dominant collision mechanisms, and find the corresponding collision cross-section. Doing so is considered to be trifling here because of two reasons. First, the required plasma parameters remain partially unknown in some of the experiments discussed later. Second, it is expected that collisions have a negligible influence on the qualitative outcome of the simulations. In the following, a collision frequency $\nu = \omega/10$ is chosen. As a result, it is observed that artifacts that are known to appear in ICRF slow wave simulations with RAPLICASOL [28] were reduced.

The results and conclusions drawn from the RAPLICASOL simulations are restricted by the validity of the underlying model. A selection of possibly influential phenomena that, besides the limitations of the cold plasma approximation, are not included in the present version of the procedure are:

- non-linearity - The dielectric tensor is independent of the electric field;
- polychromatic - The RF spectra consist of a single frequency, although it is expected that harmonics appear in a plasma;
- plasma sheath - The present model omits a description of the plasma sheath at the plasma/wall boundaries.

While it is reasonable to interpret linearity and monochromaticity as first-order approximations, it remains unknown how the plasma sheath modifies the simulations.

4.2 2-D studies

In Section 2.5, it is described that a point source in a cold magnetized plasma with relatively low plasma density induces RCs. These RCs expand along the magnetic field and open up based on the local plasma parameter. In the case of plasma density gradients, the RCs are distorted. Figure 4.2 shows results from a simulation of such a scenario. The simulation domain is a ring segment that extends to $\pm\infty$ in the z-direction. The simulation domain is terminated radially with a radial PML [33] and in the φ direction with a perfect electric conductor (PEC) boundary condition. The excitation is a line current $I = 1\,\mathrm{A}\delta(x - x_0)\delta(y - y_0)\exp(i\omega t)$ that oscillates at $x_0 = 0, y_0 = 2.13\,\mathrm{m}$ in the z-direction with a frequency of $\omega/2\pi = 100\,\mathrm{MHz}$. The

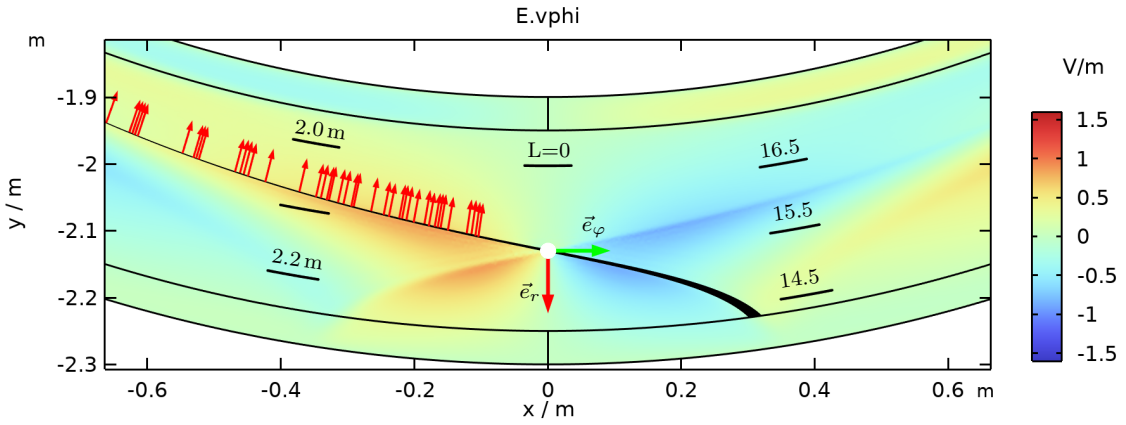

Figure 4.2: Distorted RC from a point source (magenta) in a plasma with a curved magnetic field and a radially decreasing density

source is highlighted with a white point in the middle of the Figure. Black lines on the left-hand side show the radial coordinates. The plasma density n decreases exponentially with increasing radius. This is indicated by black lines on the right-hand side of the Figure, which are labeled according to $\log_{10}(n)$. The ion species is Deuterium $m_i = m_p + m_n$. The parameters and the respective Stix parameters are collected in Table 4.1. The boundary where $L = 0$ is highlighted by a black line in

f	$100\,\mathrm{MHz}$	P	$0 - -1.6 \times 10^3 \uparrow$
$\vec{I}$	$1\,\mathrm{A}\vec{e}_z$	R	$1 - 3.5 \uparrow$
$\vec{B}_0$	$2\,\mathrm{T}\vec{e}_\varphi$	L	$1 - -2.4 \downarrow$
$n(r)$	$2 \times 10^{14} - 2 \times 10^{17}\,\mathrm{m}^{-3} \downarrow$	S	$1 - 0.6 \downarrow$
m_i	$m_p + m_n$	D	$0 - 3 \uparrow$

Table 4.1: Parameters for the point source simulation. Up and down arrows indicate how the parameters change with increasing r

the center of the Figure. The Stix parameters locate the scenario to regions 7 for $L > 0$ and 8 for $L < 0$ in the CMA diagram (Figure 2.8).

The color in Figure 4.2 represents the φ component of the electric field. The butterfly-like shape is a RC that opens up along the background magnetic field $B_0 = 2\,\mathrm{T}$ that points in the φ direction. The red arrows in Figure 4.2 illustrate the normalized electric field vector $\vec{E} = (E_x\vec{e}_x + E_y\vec{e}_y)/E$ at the tail of the arrows. The arrows are about orthogonal to the RCs. This coincides with the theory. The black curve indicates the path of the RCs. It is derived from geometric relations. It is known from Section 2.5 that the opening angle of a RC is $\tan\theta_c = \sqrt{-S/P}$. Based on that, an Ansatz is:

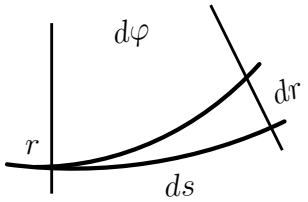

$$\tan\theta_c = \sqrt{-\frac{S}{P}} = \frac{dr}{ds} = \frac{dr}{r\,d\varphi}$$
$$\rightarrow \varphi(r) = \int \frac{1}{r}\frac{1}{\tan\theta_c}dr. \tag{4.2}$$

The integral is evaluated numerically, and the area in the interval $\varphi(r)\pm \approx 0.3°$ is colored black. The simple derivation confirms that the observed structures are indeed RCs, indicating that introducing collisions does not change the qualitative nature of the solution much.

The simulation validates the claim that RCs follow a curved magnetic field and distort at a density gradient. It also shows that the section of the RC that propagates radially inwards is confined to a layer with finite width at a distance of about 1 m to the source. This is visible in Figure 4.3. Here, an extended view of the field pattern is shown. The signal in the upper left corner of the simulation contracts

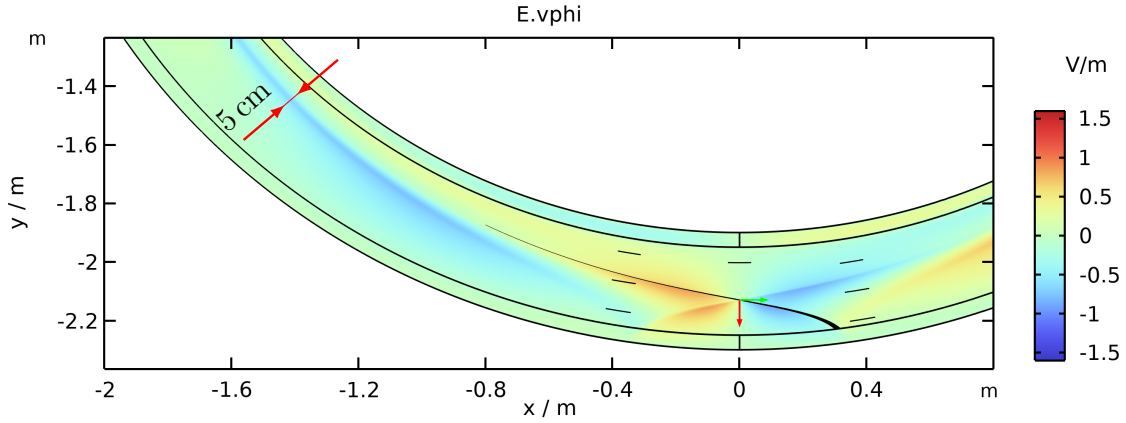

Figure 4.3: Extended view on the point source simulation

to a several-centimeter-wide layer. A similar observation is made in experiments that are discussed in Chapter 6.

The point-like simulation provides insights regarding the propagation of RF signals as RCs. Its significance is, however, limited when considering realistic RF sources with finite size. In order to extend the simulations to finite-sized objects and minimize the computational requirements, the following simulations are confined to a small area around the source. Here, the background magnetic field is in the x-direction, and the plasma density is uniform $n = 10^{15}\,\mathrm{m}^{-3}$. The plasma density is chosen to create RCs with an opening angle of about $\theta_c \approx 20°$ to make the analysis comprehensible. The discussion holds, however, for all RCs in regions 7 and 8 in the CMA diagram.

Figure 4.4 shows the results of a 2-D simulation with a circular wire as a source of RF signals in a rectangular simulation domain that is surrounded by a PML. To overcome restrictions of the software regarding the implementation of a PEC boundary condition together with a surface current density, the antenna domain is filled with copper. This leads to a condition similar to a PEC and allows the application of an external current density J_e that oscillates in the z-direction inside the conductor. In the given frequency range, it is expected that the skin effect confines the currents to a thin layer inside the conductor. This is observed in the simulations and consistent with theory. Figure 4.4 shows the component of the electric field that is parallel to the background magnetic field, the component E_x. It can be seen that, overall, four lines emerge from the current carrying wire. The

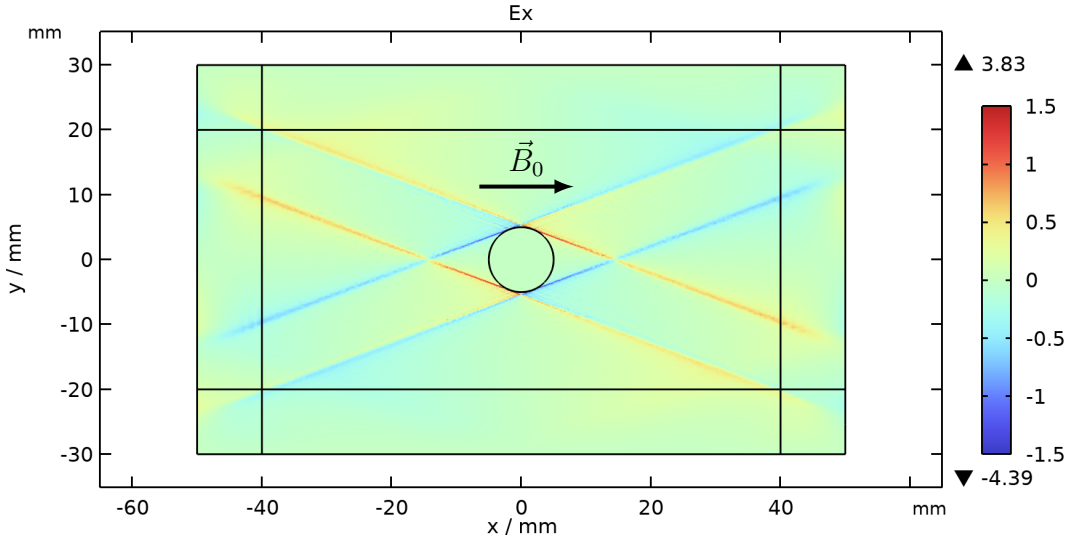

Figure 4.4: RCs emerging from a circular copper wire in a uniform plasma

angle between the lines and the background magnetic field agrees with the expected opening angle of RCs. Notice that the designation resonance cone can be misleading here. Variations in the z-direction are impossible in 2-D simulations. The observed lines are planes that extend to $z = \pm\infty$.

Figure 4.5 shows an excerpt of the same simulation. Here, black arrows represent the electric field at mesh points along the interface. It is apparent that the linear structures emerge from four points along the circumference of the wire. The set of angles are $\pm\pi/2 \pm \theta_c$.

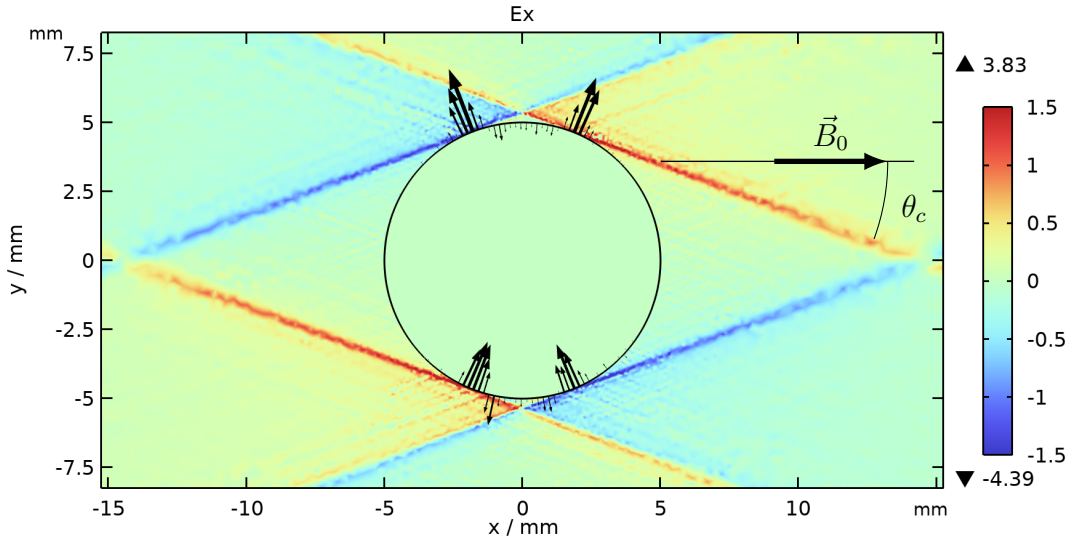

Figure 4.5: Detailed view around the copper wire

The emission of RCs from these points results from a divergence condition at the RF source/plasma boundary. The collision term that was introduced in the simulations restricts this divergence. The divergence condition is, in principle, a statement that holds for other geometries and wave types outside the ICRF. It was

described by Tierens [34]. The line of argument for a particular boundary, a circle, is repeated here. It is started by changing to a cylindrical coordinate system (r, φ, z) with the origin in the center of the circle. In the discussed 2-D scenario, the electric field is $\vec{E} = \vec{E}\left(E_r(r,\varphi), E_\varphi(r,\varphi), E_z(r,\varphi)\right)$ and the dielectric tensor reads:

$$\hat{\varepsilon} = \begin{bmatrix} P\cos^2\varphi + S\sin^2\varphi & \sin\varphi\cos\varphi(P-S) & -iD\sin\varphi \\ \sin\varphi\cos\varphi(P-S) & P\sin^2\varphi + S\cos^2\varphi & iD\cos\varphi \\ iD\sin\varphi & -iD\cos\varphi & S \end{bmatrix}$$

The r component of the wave equation in the cylindrical coordinate system is then:

$$\left(\nabla\times\left(\nabla\times\vec{E}\right) + \frac{\omega^2}{c^2}\hat{\varepsilon}\left(\varphi\right)\vec{E}\right)_r = \frac{rE_\varphi^{(1,1)} - E_r^{(0,2)} + E_\varphi^{(0,1)}}{r^2} - K = 0. \tag{4.3}$$

The superscripts represent the order of derivative either with respect to r or φ. K is:

$$K = \frac{\omega^2}{c^2}\left(-iD\sin\varphi E_z + \sin\varphi\cos\varphi(P-S)E_\varphi + E_r\left(P\cos^2\varphi + S\sin^2\varphi\right)\right).$$

From fundamental electromagnetic boundary conditions, it is known that at a PEC interface ($r = r_0$), there are no surface currents tangential to the surface:

$$\left(\vec{e}_r\times\left(\nabla\times\vec{E}\right)\right)_\varphi = 0 \leftrightarrow E_\varphi^{(1,0)} - \frac{E_r^{(0,1)}}{r} + \frac{E_\varphi}{r}\bigg|_{r=r_0} = 0.$$

Consequently, $K = 0$ is required at the cylinder boundary. Solving for E_r yields:

$$E_r\left(r = r_0, \varphi\right) = \frac{\sin\varphi(\cos\varphi(S-P)E_\varphi + iDE_z)}{P\cos^2\varphi + S\sin^2\varphi}$$

which diverges for $\tan^2\varphi = -P/S = \tan^2(\pm\pi/2 \pm \theta_c)$. The derivation shows that RCs are excited at points along the RF source/plasma boundary where the normal is parallel to the electric field of the RC. It is plausible that this generalizes to sources with different contours. The RCs emerge from all points along a boundary where the normal forms an angle of $\pm\pi/2 \pm \theta_c$ with the background magnetic field. It is reasonable to assume that source contours without the associated angles do not create RCs.

Figure 4.6 shows the results of a simulation where the cross-section of the circle was modified to address four different scenarios, each in one quadrant (I, II, III, IV). Quadrant IV is the original circular scenario as the reference. In quadrant I, the circular wire is clipped, and a sharp edge is created. Quadrant II shows the scenario of a clipped wire with a rounded edge. Quadrant III shows a scenario with a cavity-like shape. Deforming the contour of the conductor is expected to change the distribution of the surface current density along the contour. This is indeed observed and illustrated by the magenta-colored boundary that represents the local current density $\vec{J}$. It is observed that despite the clipping in quadrant I and II,

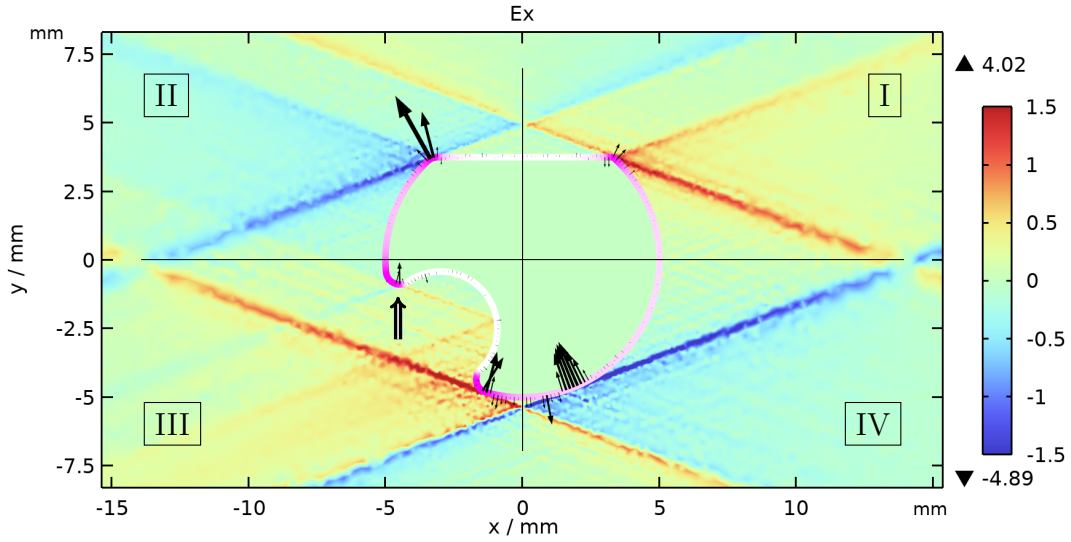

Figure 4.6: RCs emerging from a deformed wire contour

RCs emerge from the corners. In I, it is not apparent why RC emerges from the corner in quadrant I. However, the scenario is not very realistic since there exist no sharp edges in reality. In II, it is reasonable to expect that there is a point along the circumference of the rounding where the angle of the normal is $\pi/2 + \theta_c$. The field pattern in quadrant III shows that the geometry of the source affects the excitation of RCs. Consider the rounded corner that is highlighted with an $\Rightarrow$-arrow. Because of the existence of the rounding, it poses a source for RCs somewhere along the boundary. While RCs emerge from the corner, their amplitude is significantly reduced compared to their counterparts on the other side of the cavity.

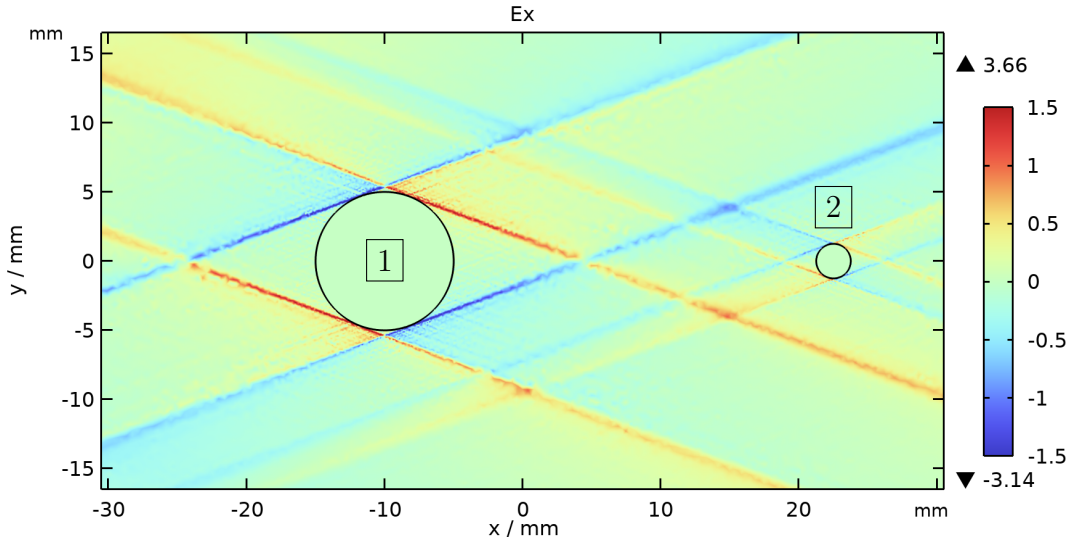

Figure 4.7: RCs emerging from a nearby passive conductor

An experimental observation, which is described in Chapter 5, motivated the simulation shown in Figure 4.7. In this case, a second [2] electrically passive wire was introduced beside the active one [1]. It is observed that the 2nd wire emits RCs.

The radio frequency field that is induced by the active wire induces RF currents in the passive wire, which then starts emitting RCs.

Figure 4.8 shows a scenario where the RCs strike a passive rectangular conductor 2. Highlighted by ⇒-arrows are the points where RCs originating from the active wire 1 hit the boundary. Intuitively, the observation is interpreted as a reflection of the RCs at the boundary. The angle of the reflected RC is, however, independent from the orientation of the normal at the interface and only determined by the orientation of $\vec{B}_0$ and θ_c.

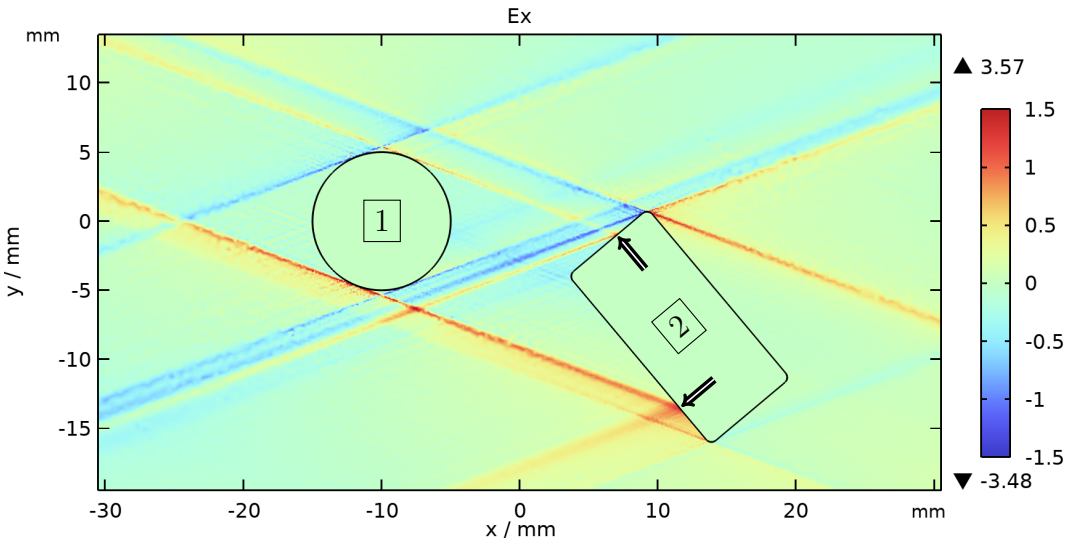

Figure 4.8: Reflections of RCs at a passive conductor

The previous simulations were excited deliberately with a surface current that oscillates in the z-direction, orthogonal to $\vec{B}_0$. However, experimental conditions deviate from this idealized scenario. For example, the straps in AUG'S ICRF antenna are oriented poloidally, but $\vec{B}_0$ is inclined in front of the antenna. To construct a simulation where the current flow is not $\perp$ to $\vec{B}_0$, the dielectric tensor is rotated around the y-axis by some angle α using a standard rotation matrix R_y. This is illustrated conceptually in Figure 4.9 for clarity. The yellow surface represents the 2-D simulation domain.

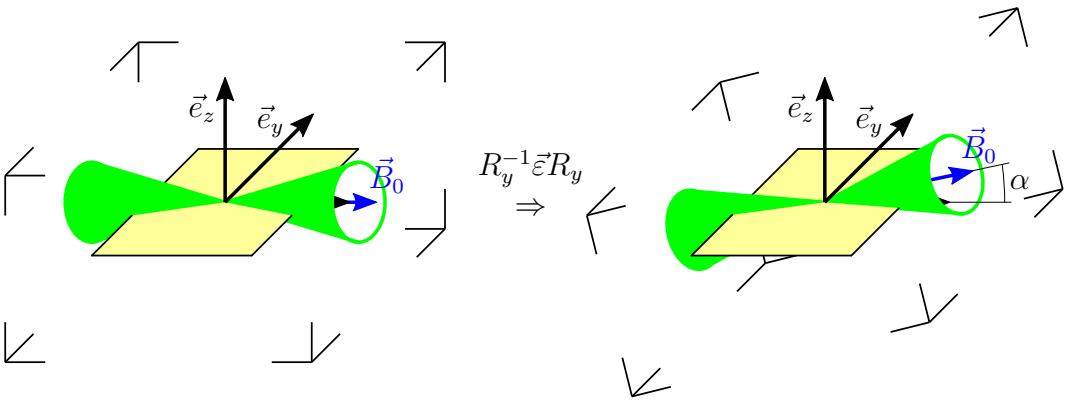

Figure 4.9: Rotation of $\hat{\varepsilon}$ in a stationary Cartesian coordinate system

The results of a simulation with a circular wire with the rotated $\hat{\varepsilon}$ are shown in Figure 4.10. Notice the significant increase in the field amplitude, which is larger by about a factor of > 10 compared to the fields shown in Figure 4.4. Notice as well the circular background field that defines the vicinity around the wire. The simulation shows that the excitation of RCs is favorable in cases where the surface current is inclined with respect to the background magnetic field.

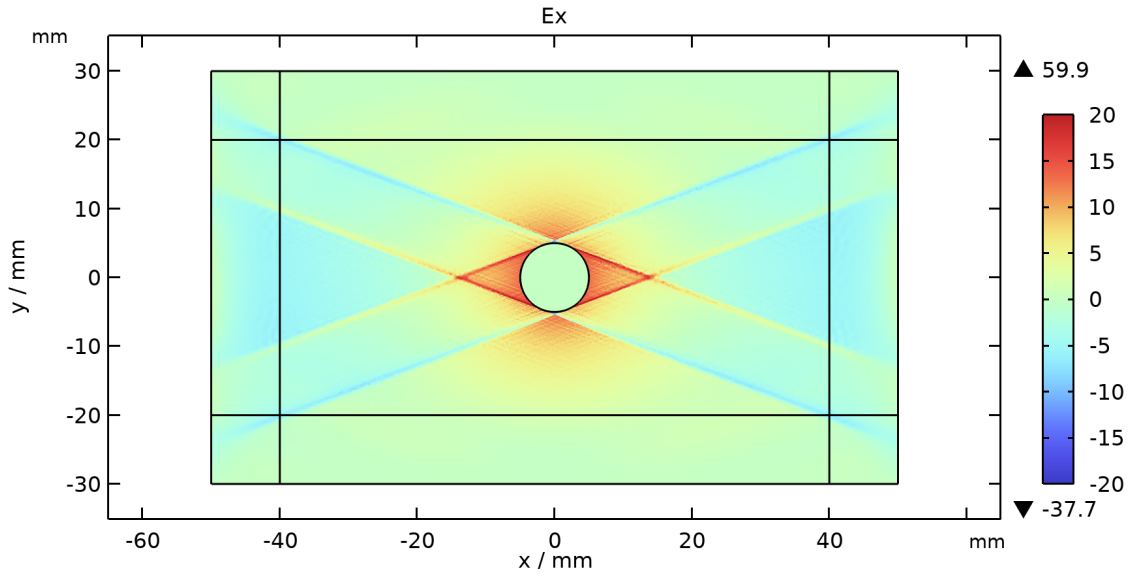

Figure 4.10: Simulation results of RCs in a rotated plasma with $\alpha = 5°$

The 2-D simulations provided insides on how RCs emerge from the sources and spread through the plasma. However, the previous simulation already showed the importance of 3-D effects. On the path toward realistic models, it is necessary to account for the self-regulating field structure and current that an antenna generates inside the plasma. The 3-D simulations overcome the limitations of the 2-D description.

4.3 3-D studies

Figure 4.11.a shows the geometry of a 3-D simulation. Located in the center is a yellow-colored copper cylinder with a radius $r_w = 5\,\text{mm}$, height $z_w = 20\,\text{mm}$, and rounded edges. An external current density in the z-direction is imposed to excite the simulation. The wire is surrounded by a green-colored cuboid representing the cold magnetized plasma via the dielectric tensor $\hat{\varepsilon}$. The direction of the magnetic field is predominantly in the x-direction, but the background magnetic field is again inclined by $\alpha = 5°$ in the xz-plane. The plasma domain is surrounded entirely by a gray-colored PML. The cross-section of the geometry is at $z = 0$, identical to the preceding 2-D simulation. Figure 4.11.b shows the current density at the conductor's boundary in the z-direction. It is maximal at $z = 0$ and approaches zero at the top and bottom ends of the conductor. The conditions represent a standing wave. Charge conservation $\nabla \cdot \vec{J} + \partial\rho/\partial t = 0$ requires an accompanying

increase in the charge density ρ towards the top and bottom of the wire. It is possible to interpret this as an increase/decrease of the electric potential in these regions. The scenario is similar to an oscillating dipole.

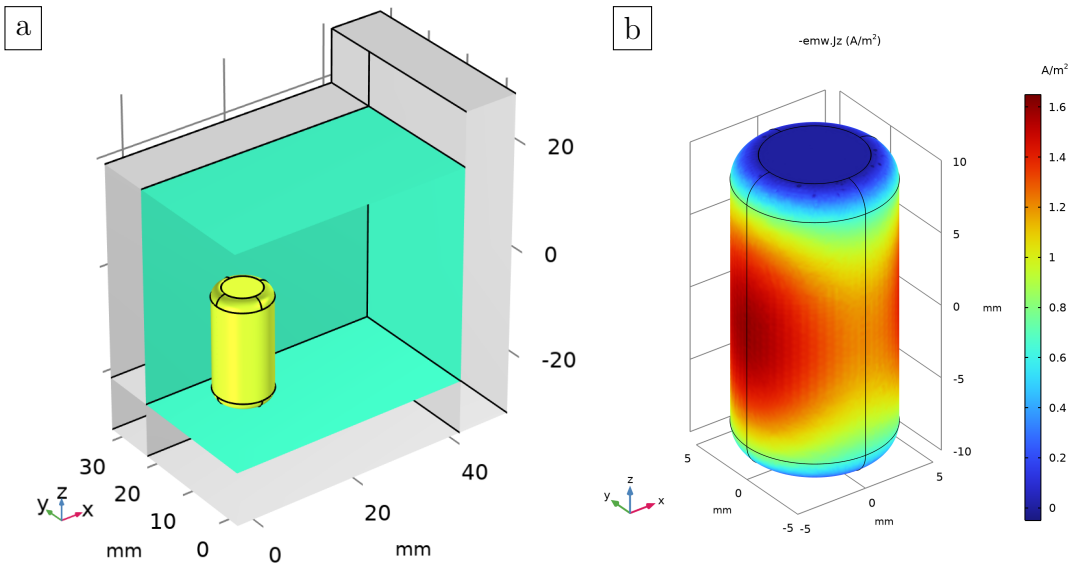

Figure 4.11: **a**: Geometry of the 3-D simulation of the short copper wire **b**: z components of the current density $\vec{J}$ on the wire

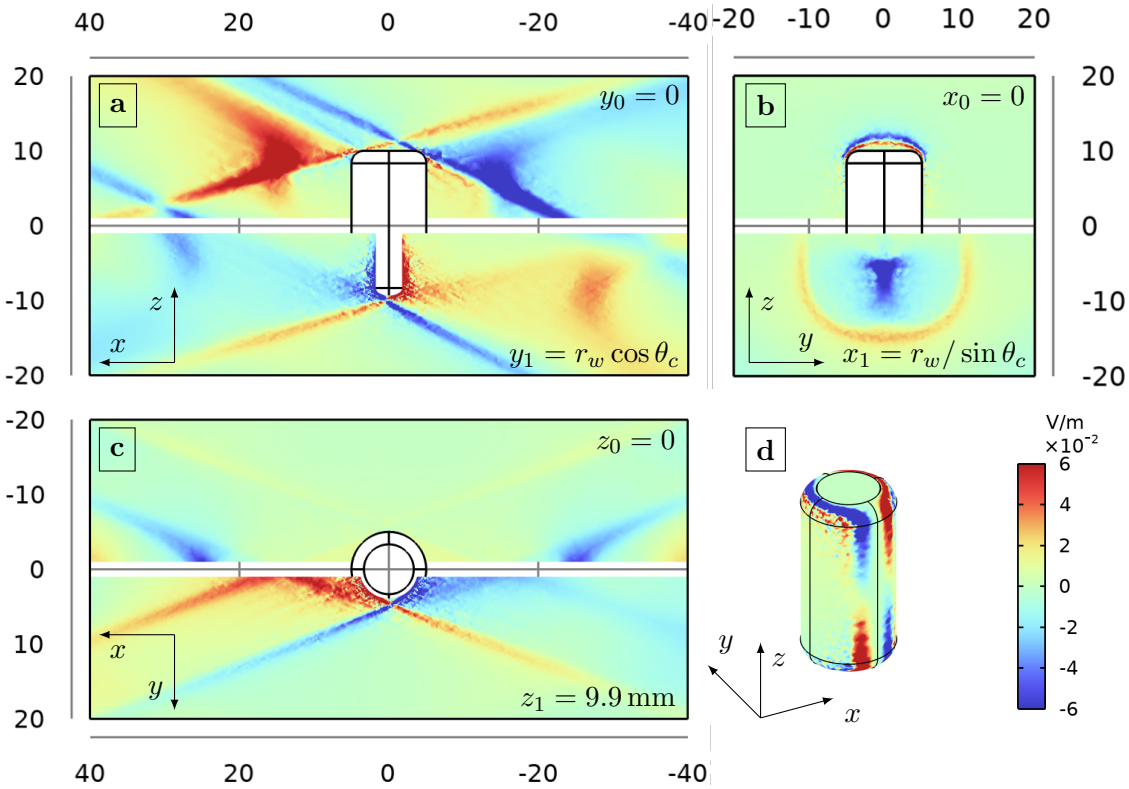

Figure 4.12: Different cross sections through the RF electric field in the plasma from the simulation with the simple wire element.

Figure 4.12 shows the x component of the RF electric field at different positions in the plasma from different perspectives. **a** shows two cross sections at $y_0 = 0$ and $y_1 = r_w \cos\theta_c$. **b** shows two cross sections at $x_0 = 0$ and $x_1 = r_w / \sin\theta_c$. **c** shows two cross sections at $z_0 = 0$ and $z_1 = 9.9\,\text{mm}$. **d** shows the field component on the wire element surface. The two cross sections in the Figures are separated by a gap to maintain readability. The cross-section at y_0 in Figure 4.12.**a** shows that the RCs with the highest field amplitudes emerge from the rounded edges at the top and the bottom of the conductor. The cross-section at y_1 shows a gradual decrease in the field amplitude of the emerging RCs towards $z = 0$. This observation is confirmed in the cross-section at z_0 in Figure 4.12.**c**, where the emerging RC is barely observable. However, it is clearly visible in the cross-section at z_1. It is plausible to assume that this is a consequence of the increased charge density ρ at the ends of the wire element. RCs emerge from points along the source boundary where the normal vector is parallel to the RC electric field. However, their amplitude is determined by the charge density distribution on the source boundary. The cross-section at x_1 in Figure 4.12.**b** shows the field distribution at a distance from the source, the RCs that expand towards larger x. The RCs that converge towards $y = 0$ intersect at x_1 and create the blue vertical region. The RCs that expand away from $y = 0$, the red corona, resemble the contour of the copper wire, but it is magnified by the opening angle of the RCs.

Exciting the simulation by imposing an external current density on a detached object is an impractical scenario. In reality, RF signals are transferred from a generator to an antenna via transmission lines. COMSOL enables the application of a coaxial lumped port boundary condition to a ring boundary. Together with a potential difference between the two bounding circles, a reference impedance defines the electromagnetic fields at the boundary. Figure 4.13 shows the x component of the electric field that develops when the copper wire element is excited at a coaxial connection, highlighted by two red arrows. The wire element becomes the

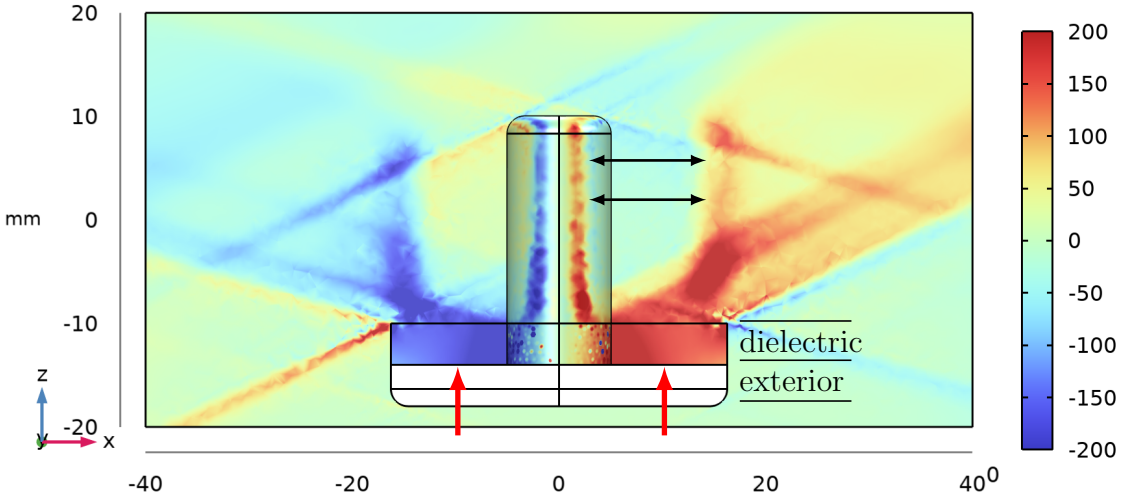

Figure 4.13: E_x at $y = 0$ and the inner conductor surface from a coaxial cable

inner conductor, and a cup-like boundary is the outer conductor of a coaxial cable. Beside a section of the inner conductor, the outer conductor contains a dielectric ring. The white section at the bottom of the outer conductor is excluded from the simulation domain and represents the interface to the exterior. It is observed that the field structure within the plasma is dominated by signals emerging from the top end of the outer conductor. At this point, the distance between the inner and outer conductor is minimal. Because of the short coaxial cable element, the electric potential difference is nearly maximal, and RCs emerge from the dielectric/plasma interface. Inspecting the fields on the surface of the inner conductor reveals that, in contrast to the detached wire element, RCs emerge along the entire extent of the inner wire. This creates the blue and red wing-like structure in the field pattern highlighted by two black arrows.

With the coaxial boundary condition, it becomes feasible to excite complex-shaped objects. Figure 4.14 shows a simplified model of a tile of the AUG ICRF antenna limiter. It consists of (yellow colored) the limiter tile itself, a slab representing the antenna frame, a cup containing the coaxial boundary condition (as in Figure 4.13 but smaller), two wire elements connecting the inner and outer conductor of the coaxial line with respectively the tile and the antenna frame, a shunt connecting the tile and the antenna frame, and a (magenta colored) dielectric between the limiter and the antenna frame. The model represents, in principle, the connection used in experiments at the AUG tokamak described in Chapter 6.

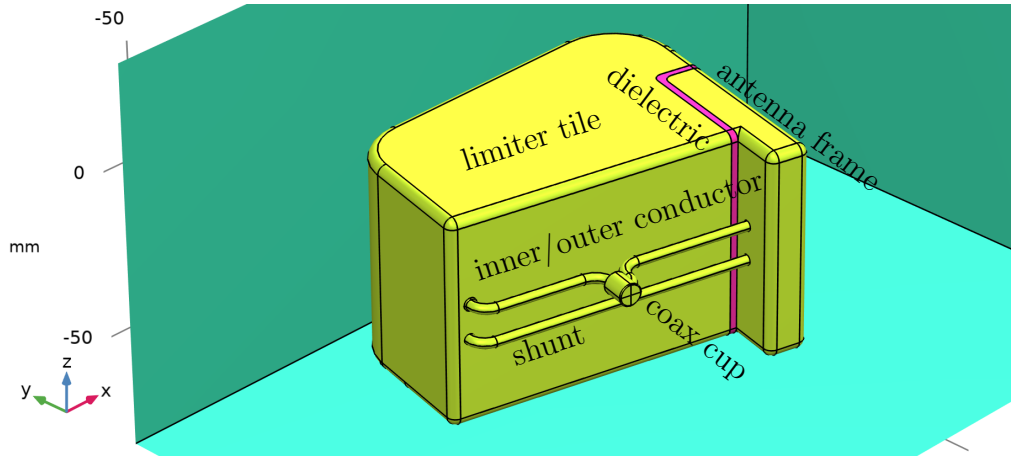

Figure 4.14: Simplified model of an AUG ICRF antenna limiter tile

The field structure that develops when a homogeneous plasma density is chosen becomes dominated by RCs that emerge from elements located behind the limiter tile. To avoid this, the plasma density was reduced to a point where RCs could not propagate anymore. Only the front section of the limiter tile is immersed in a plasma with a density that allows the propagation of RCs. The scenario gets closer to realistic conditions, where the plasma density is higher in front of the limiter than behind it. The coaxial boundary condition is excited by a 1 V potential difference at a 25 Ω reference impedance. Figure 4.15 shows the norm of the electric field that develops on the surface of the conductors and, on the left-hand side, the plasma

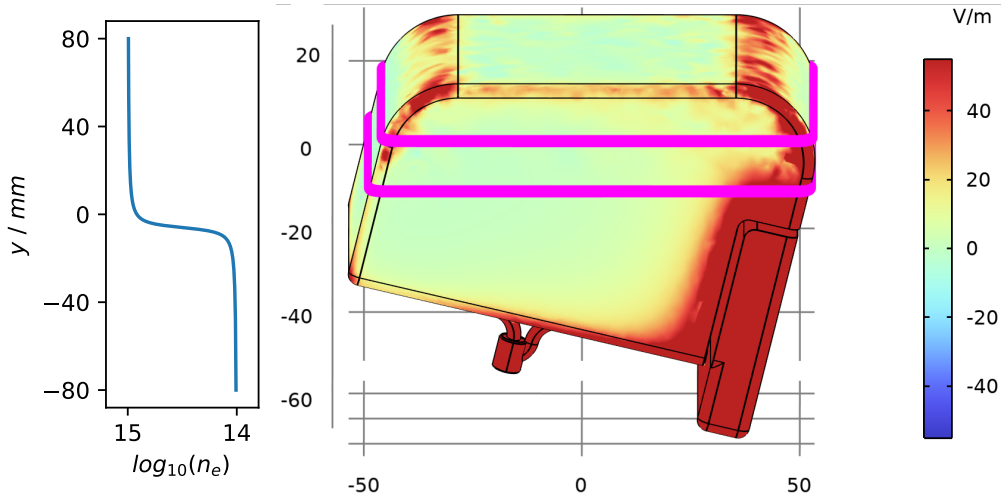

Figure 4.15: Norm of $\vec{E}$ on the conductor surface and plasma density increase along y illustrated on the left

density distribution. Magenta-colored lines on the limiter boundary indicate the transition region where the plasma density increases from about $10^{14}\,\mathrm{m}^{-3}$ to about $10^{15}\,\mathrm{m}^{-3}$. It is apparent that in the low-density region, the electric field is large around the dielectric between the limiter tile and the antenna frame. This is a consequence of the relatively short distance between the two conductors together with the presence of the dielectric. The gap represents a relatively large capacitor that forms an LC resonator together with the inductance from the wires. LC resonator cause for certain L and C, large potential differences resulting in high fields. In the plasma region, the electric field is large along the rounded edges of the tile. This is in contrast to the vacuum scenario, where the fields are high only at the roundings with the smallest radii of curvature. The geometrical shape of the tile poses a source region for RCs there, which causes the fields and currents to increase.

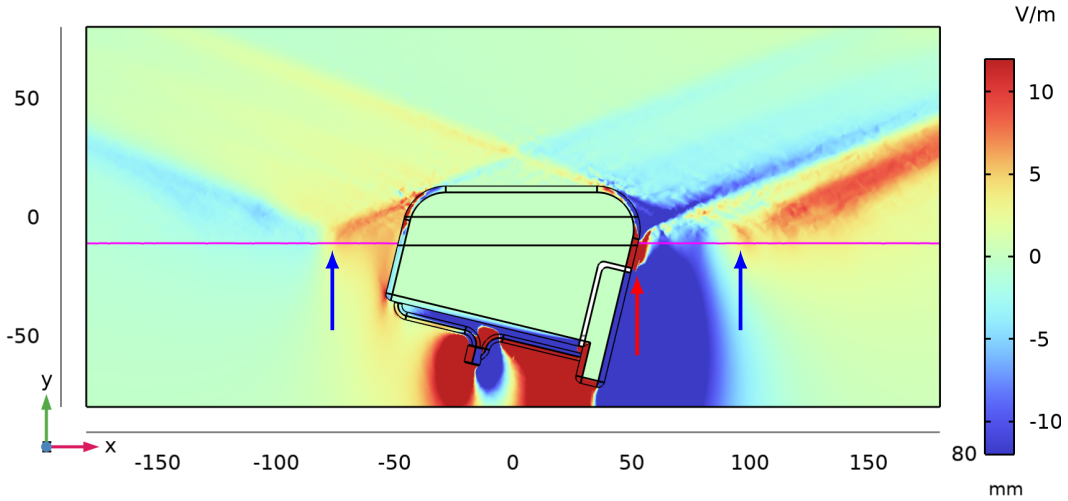

Figure 4.16: E_x in the plasma and on the conductor surface ($\varepsilon_r^{DE} = 8.5$)

Figure 4.16 shows the component of the electric field on the conductor's boundary and in the surrounding plasma at $z = 5\,\mathrm{mm}$. A magenta line separates the low from the high plasma density regions according to the Stix parameter $P = 0$. Besides the existence of the RCs, there are three important observations: 1st, RCs are reflected at the $P = 0$ interface (blue arrows); 2nd, high fields in the low-density region can induce RCs in the higher-density region (red arrow); and 3rd, the RF field is determined by RCs at some distance from the tile.

The scenario discussed in Figure 4.16 was designed to generate RCs with large amplitudes. It is a single solution of a parameter scan where the relative permittivity of the dielectric ε_r^{DE} between the limiter tile and the antenna frame was scanned between $\varepsilon_r^{DE} = 1$ to 16. Hereby, the limiter tiles (largest) capacitive component is changed without deforming the model's geometry. Figure 4.17 shows the reflection coefficient $S_{11}/1.06$ from the scan in a Smith chart. Because of the simplicity

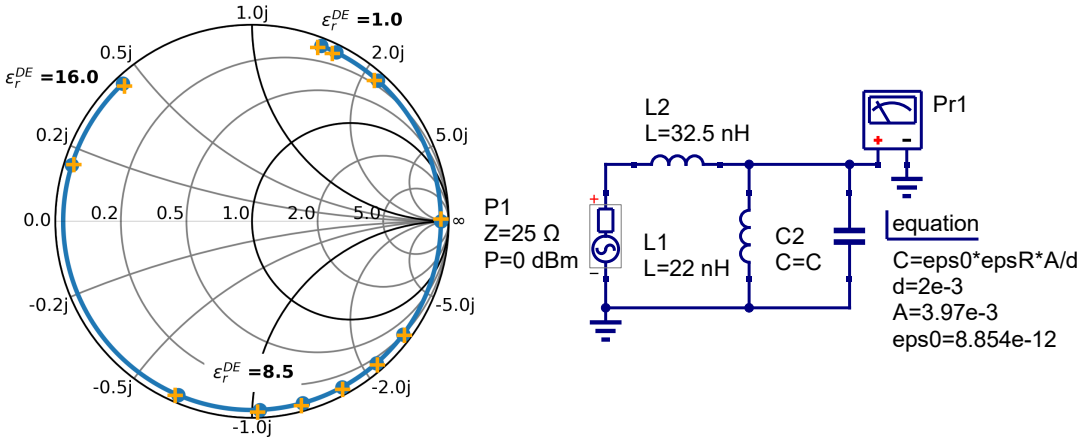

Figure 4.17: S_{11} from RAPLICASOL (orange pluses) and the model (blue dots and line) at the coaxial boundary port for different ε_r^{DE}

of the data points, it was possible to find an electric circuit that resembles the limiter tile's reflection coefficient. It is shown on the right-hand side of the Figure. It was developed with the Quite Universal Circuit Simulator (Qucs). The model parameters are reasonable values. For comparison, a pair of wires with diameter, distance, and length comparable to the parameters of the shunt and the inner and outer conductor (Figure 4.14) has an inductance of about 55 nH. The electric model reveals for which ε_r^{DE} the electric potential at the capacitor C becomes maximal. This allows to test if the amplitude of the launched RCs is connected to the electric potential of the source. Further, it connects the RAPLICASOL simulations to the experimentally accessible reflection coefficient. Figure 4.18 shows the electric potential (Qucs syntax Pr1.dv) at the capacitor C against ε_r^{DE}. The electric potential is maximum close to $\varepsilon_r^{DE} = 8.5$. This is where the resonance frequency of the series resonator, $L2$, and the parallel circuit, $L1 + C2$, is close to the stimulation $f = 100\,\mathrm{MHz}$:

$$f_{res} = \frac{1}{2\pi}\sqrt{\frac{L_1 + L_2}{L_1 L_2 C_2}} \approx 114\,\mathrm{MHz}.$$

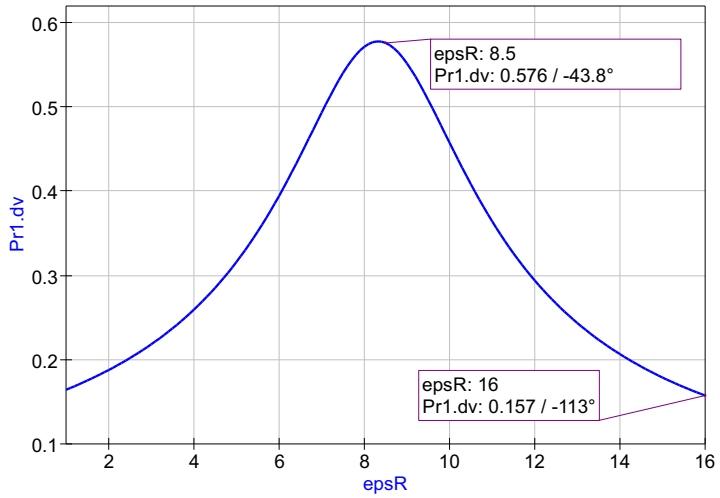

Figure 4.18: The electric potential at the capacitor against relative permittivity of the dielectric

Within the chosen range, the minimum electric potential at the capacitor occurs at $\varepsilon_r^{DE} = 16$. Figure 4.19 shows E_x for this case. The entire field structure is significantly reduced compared to 4.16.

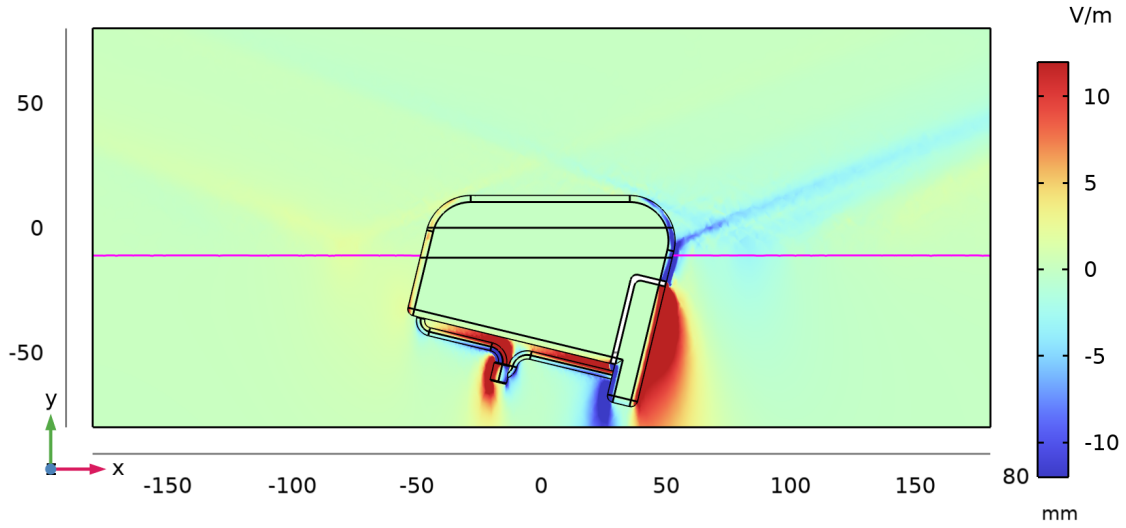

Figure 4.19: E_x in the plasma and on the conductor surface ($\varepsilon_r^{DE} = 16$)

The findings of the performed RAPLICASOL simulations are summarized.

- RCs that are known to exist for specific plasma parameters (Section 2.5) appear in the simulated field structure. These RCs are propagating ICRF slow waves. The properties of the observed RCs, specifically the opening angle and the electric field orientation, match the theoretical expectations.
- RCs follow curved magnetic field lines and distort at density gradients (Figure 4.2) in agreement with a simple geometrical model (Equation (4.2)). The branch of the RCs that faces the increasing density approaches the layer with

the lower hybrid resonance density.

- Passive objects in the vicinity of an active antenna emit RCs (Figure 4.7).
- RCs are reflected at conductors (Figure 4.8), insulators, and the $P = 0$ layer (Figure 4.16). The angle of reflection is independent of the boundary's normal vector and solely defined by the orientation of the background magnetic field and the RC opening angle.
- As a consequence of a divergence condition, antennas excite RCs primarily at points along their circumference where the normal vector is parallel to the electric field vector of the RCs. A modified antenna contour showed, however, that the amplitude of the RCs can be manipulated (Figure 4.6).
- The existence of RCs leads to a redistribution of fields and currents to regions on the antenna where the above-mentioned resonance condition applies. Specifically for the limiter tiles, this leads to the activation of edges that intuitively would not contribute much to the field structure.
- The electric field distribution at some distance from the source along the background magnetic field resembles the source contour while being scaled up or down according to the RC opening angle (Figure 4.12).

Chapter 5

ICRF slow waves in IShTAR

Before performing experiments on AUG, a series of experiments was conducted on the ion sheath test arrangement (IShTAR). The intention was to gain experience in measuring lower hybrid RCs as the manifestation of the ICRF slow wave. The problem was divided into:

- how to launch RCs into the plasma;
- how to measure RCs;
- and does a simplified RC theory describe the fields.

The experimental setup used in IShTAR was motivated by experiments described by Fisher and Gould in 1969 [35]. They were among the first to describe the detection of RCs in a magnetized plasma using a relatively simple setup composed of two short dipole antennas: a transmitting antenna launching the cones and a receiving antenna attached to a rotatable mount, see Figure 5.1.a. The plasma

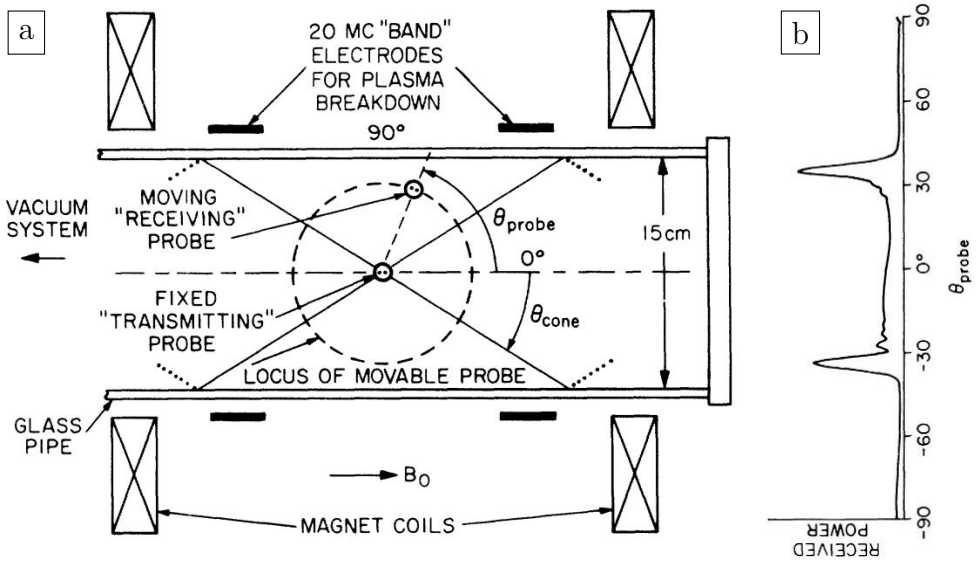

Figure 5.1: Schematic of the setup used by Fisher and Gould [35]

was produced by an RF discharge inside a glass tube surrounded by two magnetic field coils. Fisher and Gould observed strong signals at the receiving antenna output at angles in agreement with cold plasma theory; see Figure 5.1.b. With their experimental setup, Fisher and Gould studied RCs around ω_{ce}, but they proposed the possibility of studying RCs in the ICRF as well.

The present work attempts to incorporate the original approach to probe the electric potential produced by RCs. Figure 5.2 shows a schematic of the experiment: RF signals from a source are launched from an antenna into the plasma. The plasma determines the propagation of the RF waves. Because RCs are expected to be electrostatic waves, it is attempted to measure the RF perturbation of the electric potential by inserting a probe into the plasma. The probe is kept on average on floating potential, and the RF signals are measured using an RF detector. A Langmuir probe measures the plasma parameters to connect the measurements to the dispersion relation. The following description is limited to a subset of experiments, called discharges referenced using *xXXX, carried out on IShTAR.

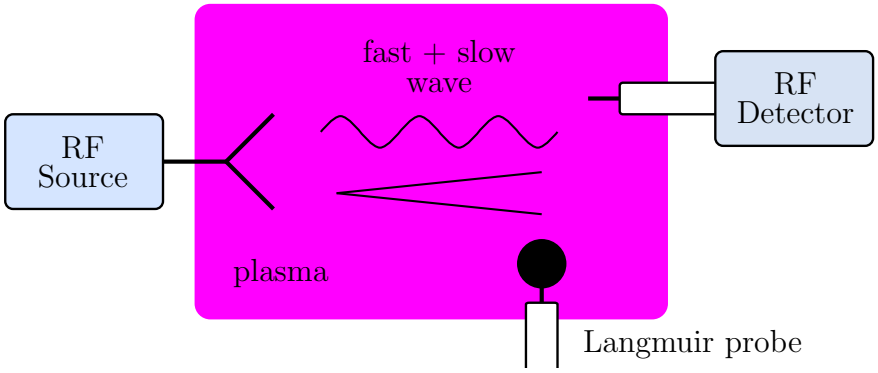

Figure 5.2: Schematic of the experimental concept

5.1 Experimental setup

The IShTAR experiment is a cylindrical vacuum vessel that is surrounded by two magnetic field coils in a Helmholtz configuration. The background magnetic field in IShTAR is oriented along the symmetry axis of the vacuum vessel, and the magnetic field strength is up to 0.2 T. To create a plasma, IShTAR is equipped with a Helicon source and a single-strap ICRF antenna. The plasma density created by the usual plasma sources is typically too high for ICRF slow wave studies, and the so-called wire-loop antenna was used instead. Figure 5.3.a. shows the wire-loop antenna in IShTAR. The Figure shows also three probes at the top of the image. The antenna, as well as the probes, were mounted to two manipulators. This allowed to position them independently radially r with respect to IShTAR's symmetry axis, as indicated in the Figure.

The wire-loop antenna, Figure 5.3.b, was made from a stainless steel wire, two sleeves, and a mounting plate. The wire was bent into the shape of two parallel

circle segments spanning around 80° with a radius of about ≈ 125 mm and an axial distance of about ≈ 30 mm. The wire was connected to the inner conductor of two type N connectors that were attached to the back of the mounting plate (not visible in the Figure). The sleeves were electrically connected to the outer conductor of the type N connector via the mounting plate, which in turn was attached to the lower manipulator. Coaxial cables, shielded with flexible metallic tubes, were used to connect the wire-loop antenna via vacuum feedthroughs to the outside. Figure

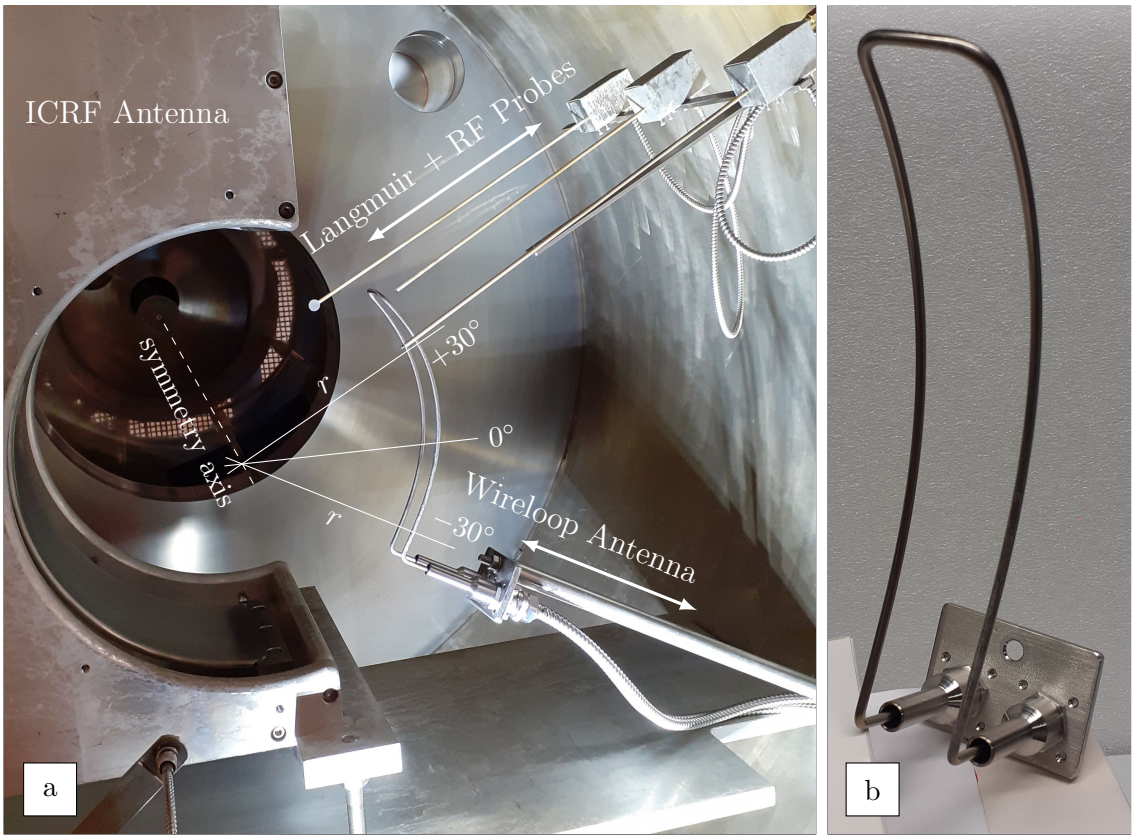

Figure 5.3: **a**: The experimental setup inside of IShTAR and **b**: The wire-loop antenna.

5.4 shows a sketch of the tips of the three probes: RF probe 1, RF probe 2, and the Langmuir probe. All probes have identical internal components but differ in the part that is exposed to the plasma. The probe's core is a metallic wire with a diameter of approximately 0.5 mm. For the RF probes, the wire protrudes out of the probe's body, forming either a short tip or extending about 10 mm at an angle of 90°, forming an L shape. To increase the collection area of the Langmuir probe, the wire was welded to a metallic disc with a diameter of 10 mm. Inside the probe, the metallic wire is covered with a flexible PTFE hose (blue) to insulate it from a metallic tube, surrounding it for electrical shielding. The outermost layer is a ceramic tube (yellow) insulating the shield from the plasma. The probes are fixed to small metal boxes that are distributed along a metal strap at the upper probe manipulator. Inside the metallic boxes, the probes' cores are connected to

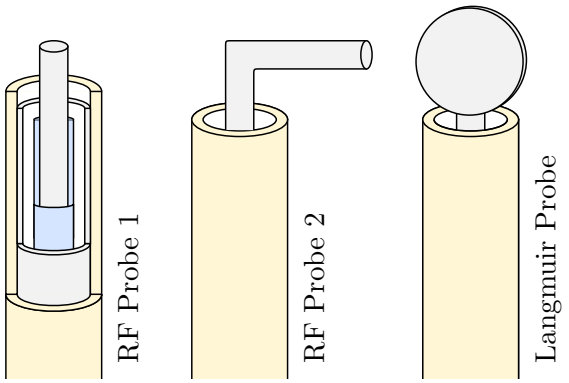

Figure 5.4: Schematic of the different probes

the inner conductor of SMA connectors that emerge from the boxes at the bottom (not visible in Figure 5.3.a). The metallic shielding tubes are electrically connected to the outer conductor of the SMA connectors via the boxes' body. Coaxial cables, shielded with flexible metallic tubes, connect the probes via vacuum feedthroughs to the outside.

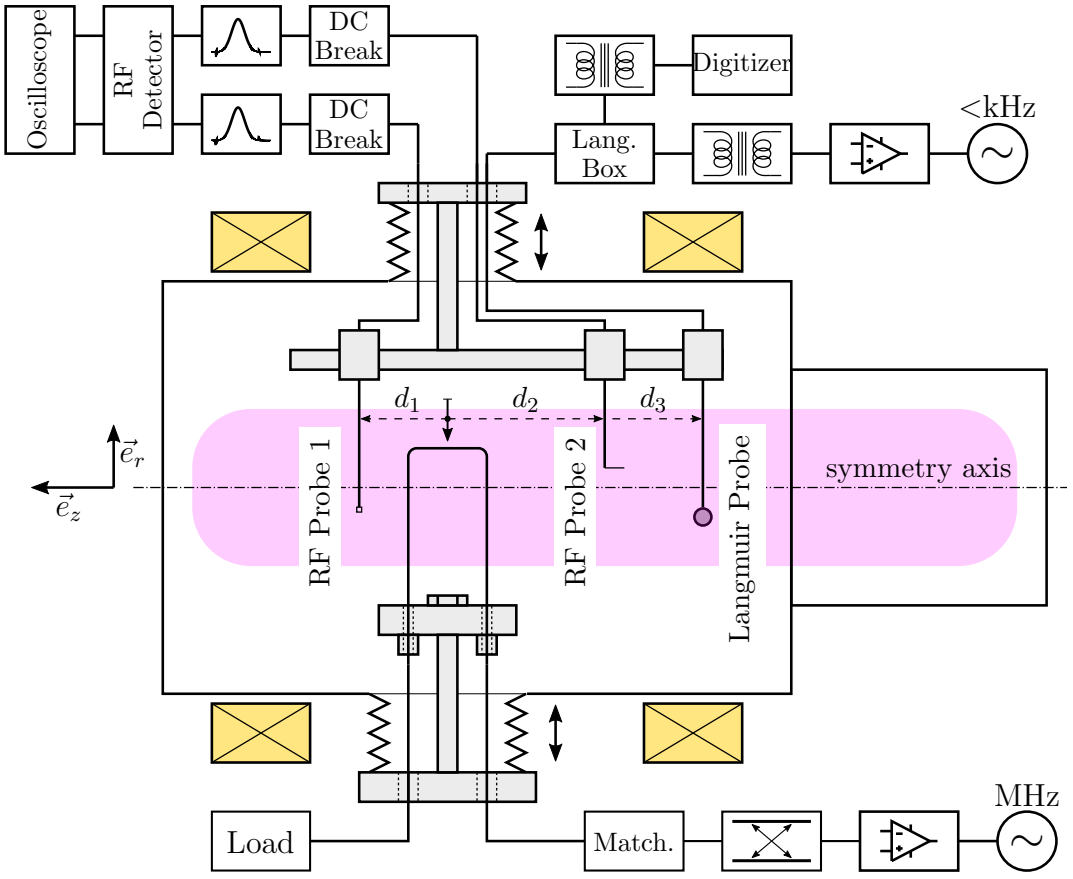

Figure 5.5: Schematic of the wiring of the experimental setup in IShTAR

Figure 5.5 shows the wiring of the experiment. As seen in the lower part of the Figure, one of the connectors at the wire-loop antennawas connected to a 50 Ω load.

The second connector at the wire-loop antennawas connected via a stub + trombone matching network and a directional coupler to an RF amplifier + oscillator. Unless mentioned differently, the oscillator was operated at $f = 100\,\mathrm{MHz}$.

The wiring of the probes is considered in the upper part of Figure 5.5. The RF probes were kept on floating potential with DC breaks. DC breaks are components that block low-frequency signals but allow RF signals to pass. The signals from the RF probes were fed through a bandpass filter to suppress harmonics before they were detected with an RF detector. The output signal of the RF detector was measured with an oscilloscope. The Langmuir probe was connected to a so-called Langmuir box. It is a collection of electronics that measures the I-V characteristic. The Langmuir box is insulated from the voltage source with an audio transformer and from the digitizer with an isolation amplifier.

A plasma formed around the wire-loop antenna in the presence of a background magnetic field. The plasma is maintained after the magnetic field has elapsed. A picture of the antenna with the plasma is shown in Figure 5.6. The default gas type is Argon, and the default gas pressure is $25 \times 10^{-3}\,\mathrm{mbar}$. The picture was taken with a camera that is located outside of IShTAR. The camera aims through a glass window on the back of the wire-loop antenna. It is possible to identify RF probe 1 to the left of the wire-loop antenna. IShTAR's axis of symmetry is oriented horizontally.

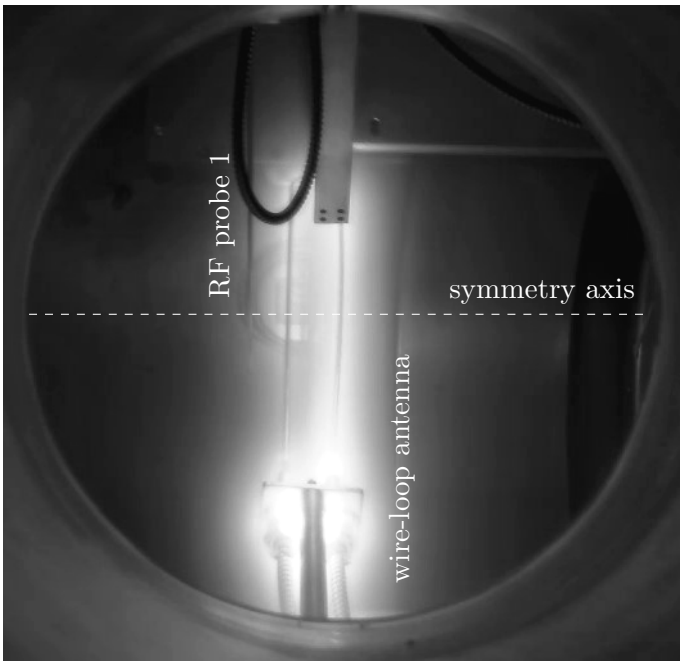

Figure 5.6: wire-loop antenna with plasma from *475 without magnetic field

5.2 Finding the RCs

In the early stages of experiments, it was noticed that RCs exist only in a subset of IShTAR's operational parameter space. The reason is that RCs do not exist at some plasma parameters that are accessible with the experiment; see Section 2.5. However, how the plasma was generated had a major influence on the plasma density. It was impossible to use IShTAR's helical antenna to create a homogeneous plasma column because the plasma density produced by it proved to be too high for the studies. But, the wire-loop antenna produced a plasma of suitable density. However, this led to a non-uniform distribution of the plasma through the vessel, as indicated by the light emission from the plasma.

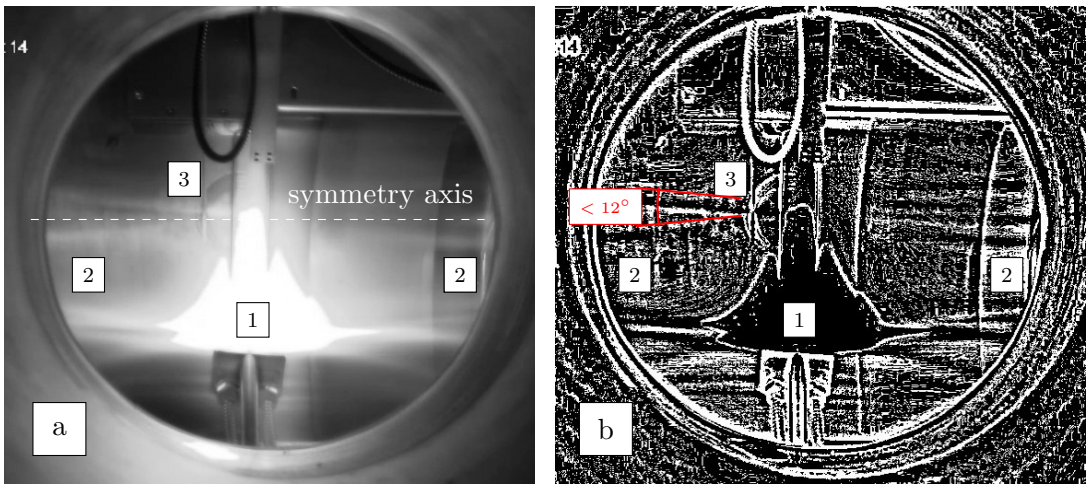

Figure 5.7: **a**: wire-loop antenna with plasma, *475, $t \approx 4.53\,\mathrm{s}$, $B_0 \approx 70\,\mathrm{mT}$,
b: Picture after applying an adaptive threshold method

For certain parameters, it was possible to observe linear structures with non-zero angles with respect to $\vec{B}_0$ in the camera images. Figure 5.7.a shows the image taken by the camera during discharge $*475$ at $\approx 4.53\,\mathrm{s}$ where a magnetic field at the wire-loop antennaof $B \approx 70\,\mathrm{mT}$ was present. Figure 5.7.b shows a processed version of the image after an adaptive threshold method [36] was applied. It assigns each pixel either a high value (white) or a low value (black) depending on whether it is above or below a threshold that is defined by the surrounding pixels. This highlights the perception of gradients in the intensity.

Numbers label highlights in the image:

1. Most of the light is emitted from a region around the wire-loop antenna's base plate. The electric fields are highest at the point where the wire exits the sleeves. For clarification, it is referred to Figure 5.3.b. Higher electric fields cause higher power flows, thus generating a larger source term in this region.

2. There are linear structures with a non-zero angle to $\vec{B}_0$ in the picture. They are, in particular, visible in Figure 5.7.b. The lines appear to emerge from the

wire-loop antenna. Over the course of a discharge, the angles between the lines and the horizontally aligned $\vec{B}_0$ vector were shrinking as the magnetic field increased. The sequence of this observation is consistent with expectations for RCs: It is known from Section 2.5 that the opening angle of a RC is defined by $\tan\theta_c = \sqrt{-S/P}$. Figure 5.8 shows the calculated θ_c as a function of B_0 using the experimental parameters and assuming $q_i = +e$. For small B_0, the graph is dominated by a $1/B_0$ term. For larger B_0, this is not the case, and θ_c approaches a value defined by ω_{pe}. It is possible to compute an electron density from the observed angles. With an angle of about 6°, this corresponds to a plasma density of $n_e \approx 1 \times 10^{16}\,\mathrm{m}^{-3}$. The linear structures in the plasma are interpreted as RCs.

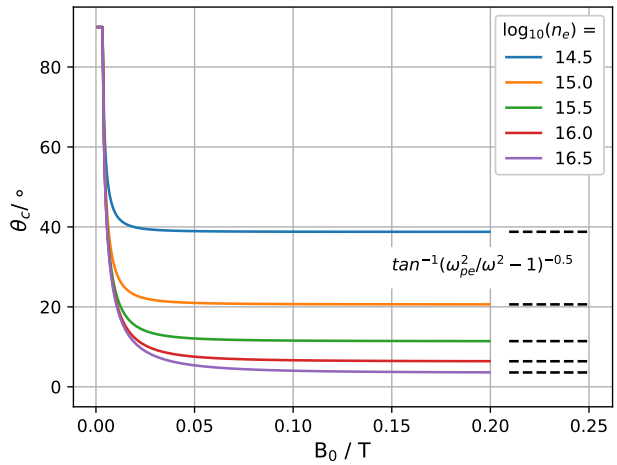

Figure 5.8: Calculated θ_c as a function of B_0 in Ar with $f = 100\,\mathrm{MHz}$

3. RCs emerge from the body of RF probe 1 when it is positioned such that it extends past the wire-loop antenna. The observation coincides with the observations in the RAPLICASOL simulation Figure 4.7. The cones emerge from the point where the distance between the wire-loop antennaand the probe is minimal since the fields are the highest there.

5.3 Measuring the RCs

After identifying the RCs with the camera, it was attempted to measure them with the RF probes. For this purpose, discharges with a constant B_0 of about 0.13 T at the wire-loop antennawere performed. At that point, the opening angle becomes independent from the magnetic field and depends only on the plasma density. To measure the field profile, the probe manipulator was moved radially inwards over the course of a discharge. Because of experimental limitations, it was necessary to perform two consecutive discharges for an entire scan.

Figure 5.9 shows data from discharges ∗819 and ∗820. $\boxed{a}$ and $\boxed{b}$ show the signals U_1 and U_2 from the two RF probes 1 and 2 against their radial distance to IShTAR's symmetry axis r. $\boxed{c}$ shows the current I_L as a function of the potential

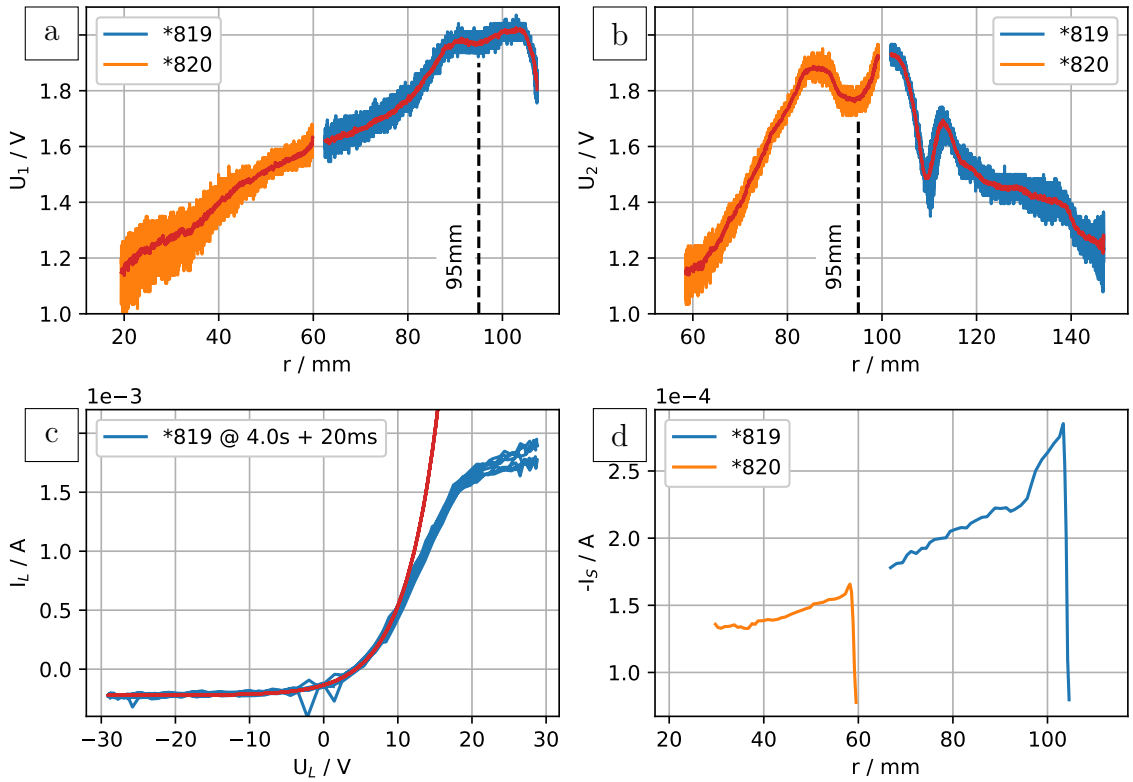

Figure 5.9: Representative signals from discharges *819 and *820

U_L of the Langmuir probe during a short time interval. $\boxed{d}$ shows the ion saturation current I_s as a function of r.

The signals from the two RF probes, $\boxed{a}$ and $\boxed{b}$, were filtered with a Savitzky-Golay filter from the scipy library [37] with 3rd-order polynomials and a window width of 51 data points. This is represented by the red lines. It can be seen that the signals from the two consecutive discharges create continuous graphs. This is interpreted as a sign of high repeatability between the discharges. The signal in $\boxed{a}$ increases gradually towards a region, which can be interpreted as two close maxima. The signal in $\boxed{b}$ shows stronger radial changes with two pronounced and a lesser maxima. Notice that in $\boxed{b}$, a signal difference of up to 0.8 V corresponding to a 16 dB change was measured in the interval 60 mm to 85 mm.

The different characteristics of the signals U_1 and U_2 are explained by the different distances of the RF probes to the wire-loop antenna. Consider Figure 5.10, which shows a sketch of the wire-loop antenna as recorded by the camera. Two orange arrows indicate the paths of the RF probes. The distance between RF probe 1 and the wire-loop antenna is about $d_1 \approx 4$ cm, whereas the distance between RF probe 2 and the wire-loop antenna is about $d_2 \approx 10.5$ cm. The signal that is measured by RF probe 1 is interpreted as the superposition of a decaying near field from the antenna and RCs. Over the distance towards RF probe 2, the near field decays, and the field structure is dominated by RCs. This agrees with geometrical considerations that are indicated by blue lines in the Figure: any diverging field that emerges from the wire-loop antenna creates a broader profile at a larger distance.

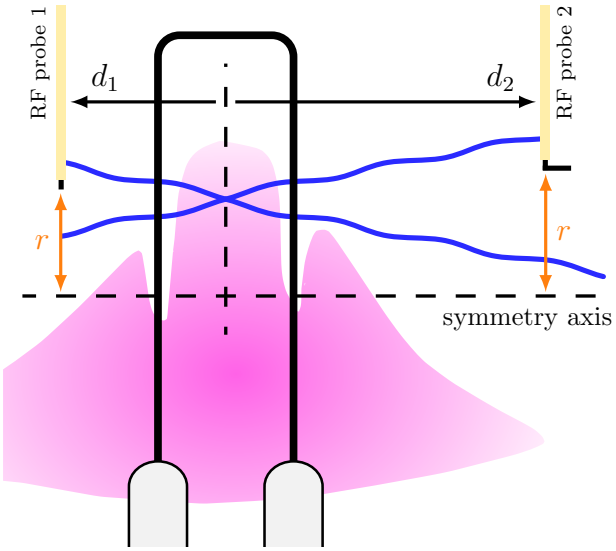

Figure 5.10: Schematic of the wire-loop antenna with the two RF probes

In both graphs, the maxima are located around a minimum close to $r = 95\,\text{mm}$, which is close to the radial position of the wire-loop antenna $r \approx 90\,\text{mm}$.

The graph in Figure 5.9 c) shows the characteristic of the Langmuir probe during a 20 ms interval. The measured curve resembles the expected shape of a Langmuir probe; see Figure 2.2. Additionally to the data, a least squares fit is included in red. The model function is described by Equation (2.4). The fit parameters are $I_{sat} \approx 0.22\,\text{mA}$, $U_{float} = 4.35\,\text{V}$, and $k_B T_e \approx 4.6\,\text{eV}$. Provided that the majority of argon ions is in charge state $Z = +1$, $T_i << T_e$, $A_{eff} = 2\pi r^2$ and f = 0.5 is applicable, this corresponds to a density of $n_e = I_{sat}/efc_s A_{eff} \approx 5.3 \times 10^{15}\,\text{m}^{-3}$. Because some parameters (T_i, Z, A_{eff}) and the influence of the RF fields on the $k_B T_e$ parameter remained unknown, the ion saturation current is considered a preferential parameter. It is used hereafter as a proxy for the plasma density.

While it is possible to interpret the measured profiles as a field structure created by RCs, further confirmation was required to eliminate coincidence. A parameter scan was performed to check whether the experimental observations changed according to expectations. Three parameters influencing the dispersion relation were identified: the RF power sent to the wire-loop antenna, the frequency of the RF waves, and the ion mass.

Within certain limits, it was possible to change the plasma density by changing the RF power. Since the opening angle of RCs scales with $1/\omega_{pe}$, it was expected to observe this in the profiles. One of the results of the RF power scans with 11 steps between 6 W and 90 W is displayed in Figure 5.11. The Figure is constructed by interpolating between the filtered signals from the RF probes. The individual signal profiles were normalized to the RF forward power and positioned based on the radial averaged ion saturation current $\langle I_{sat} \rangle$. Consistent with expectations, the field structure broadens at lower and narrows at higher $\langle I_{sat} \rangle$. The profiles follow the red dashed curves plotted in the Figure. The curves describe at which point the RF probes would cross through a single RC that emerges from the center of the

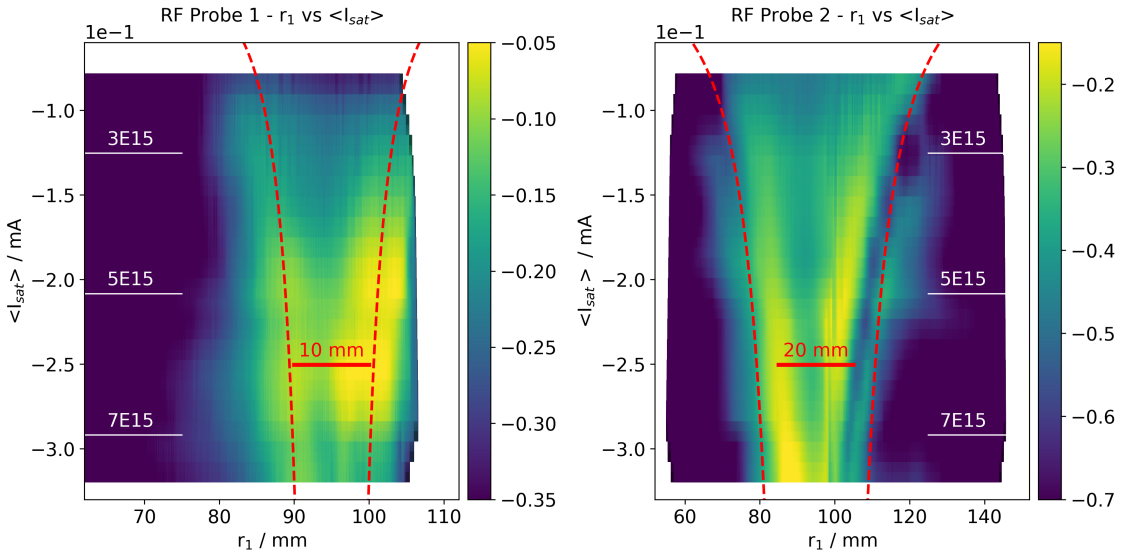

Figure 5.11: RF signals from discharges in the range *806-*828 in Ar with $f = 100\,\mathrm{MHz}$

wire-loop antenna. To compute the curves, the plasma density and assumptions regarding the plasma temperature ($k_B T_e = 4.6\,\mathrm{eV}$) and the effective collection area of the Langmuir probe ($A_{eff} = 2\pi r^2$) were necessary. The electron density per m^3 is shown in the Figures in white.

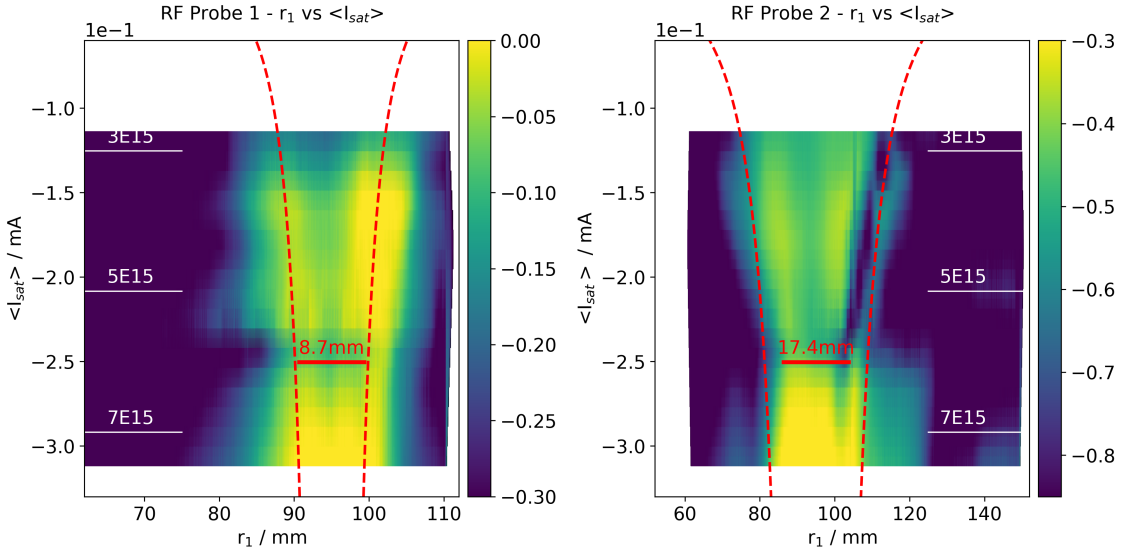

Figure 5.12: RF signals from discharges in the range *901-*923 in Ar with $f = 87\,\mathrm{MHz}$

The consistency of the experimental data with the expected RC properties is further elaborated by the results displayed in Figure 5.12. It shows the results from a power scan at a frequency of $f = 87\,\mathrm{MHz}$. In agreement with expectations, the field structure narrows compared to the experiments with $f = 100\,\mathrm{Hz}$ since θ scales

with ω. This is emphasized by a horizontal red line that is located in both Figures at $\langle I_{sat} \rangle = -0.25\,\mathrm{mA}$. The length of the line reduces from 10 mm in Figure 5.11 to 8.7 mm in Figure 5.12.

With the foresight to studies on AUG, experiments with smaller ion masses were performed. The results of experiments in Helium are shown in Figure 5.13. Notice the different $\langle I_{sat} \rangle$ range. From Section 2.2, it is known that I_{sat} is $\propto n_e c_s$. Because of $c_s \propto \sqrt{1/m_i}$, the opening angle scales with $1/\sqrt[4]{m_i}$, recalling that $\tan\theta \approx \omega/\omega_{pe}$ and $\omega_{pe}^2 \propto n$. With a mass ratio of about 1/10 from Helium to Argon, it is expected to observe a spread by a factor of about 1.8. This is again emphasized with red scales at the same $\langle I_{sat} \rangle = -0.25\,\mathrm{mA}$. The line stretches from 8.7 mm to approximately 15.7 mm.

The observations indicate that RCs were launched from the wire-loop antenna and detected with the RF probes. Simple geometric relations describe the propagation of the fields through the experiment. To prepare experiments at AUG, a single tile of AUG's ICRF antenna limiter was utilized as an antenna in the next step.

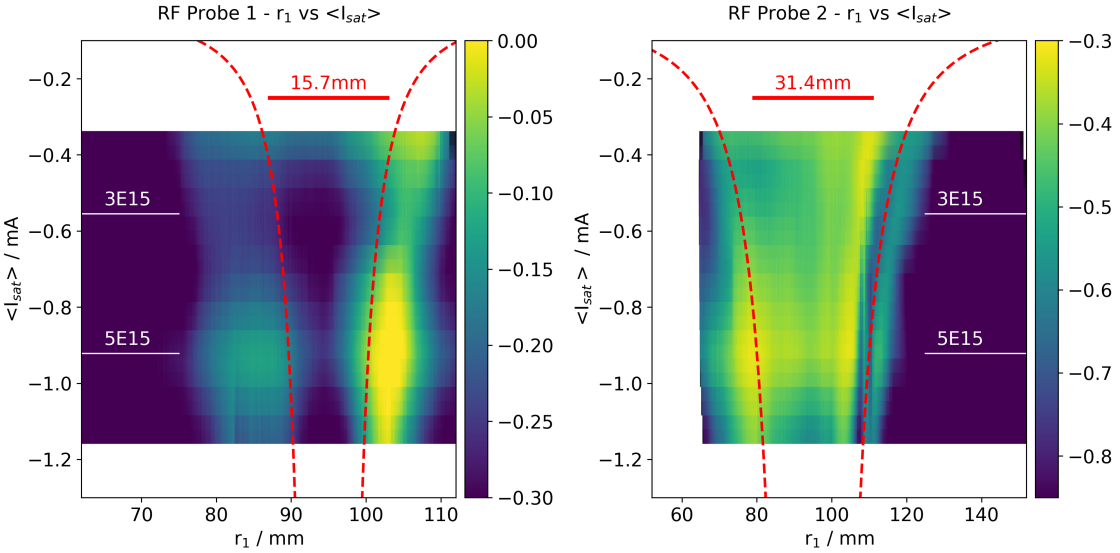

Figure 5.13: RF signals from discharges in the range *983-*998 in He with $f = 87\,\mathrm{MHz}$

5.4 Limiter tile as antenna

Figure 5.14 a) shows the limiter tile installed in IShTAR, b) and c) provides a detailed view from different perspectives. In Figure 5.14 b), two reference points, #1 and #2, at the limiter tile are highlighted with red arrows. The image in Figure 5.14 c) shows a view of the back of the tile. Here, a prototype of an electrical connection of the RF source to the limiter tile is shown. The approach of the design was to connect the inner conductor of a coaxial cable to the edge of the limiter tile, as shown on the left in Figure 5.14 c). It was intended to redirect the RF fields to the front of the tile by electrically connecting the limiter tile to the

grounded mounting plate only at the interface highlighted by the green arrow in Figure 5.14 b). The interface at which the limiter tile is mounted to the plate, highlighted by a blue arrow, is electrically insulated with a mica sheet.

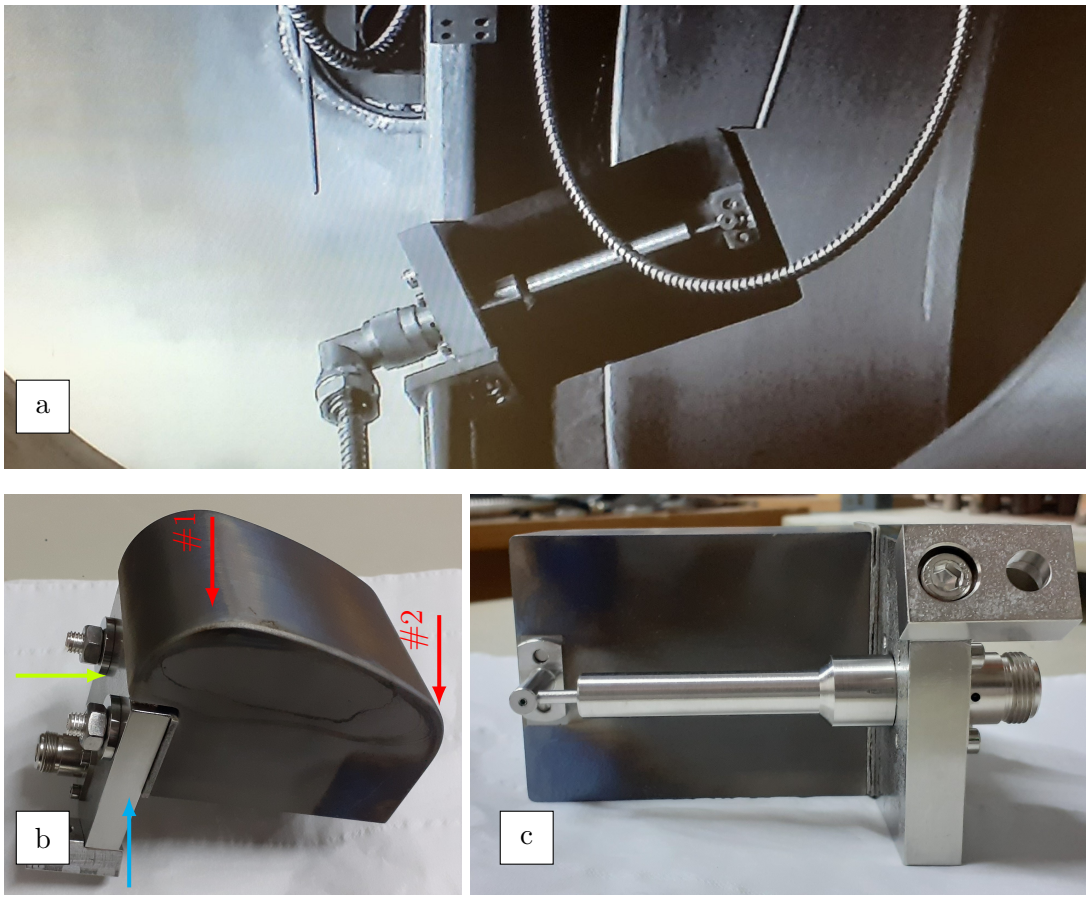

Figure 5.14: AUG limiter tile in IShTAR. a: installed, b: overview, and c: backside view

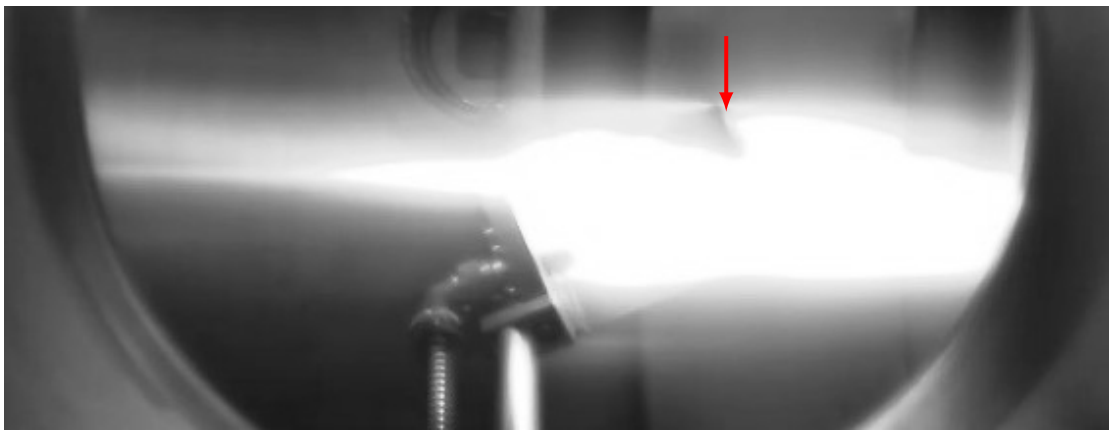

Figure 5.15: Limiter tile with plasma in IShTAR. *1186, $P_{for} \approx 45\,\mathrm{W}$

During experiments, RF power between P_{for} 20 W and 90 W with the frequency of $f \approx 99$ MHz was sent to the limiter tile. Figure 5.15 shows the tile within the plasma that developed at a B_0 of about 0.13 T. The distinct features that were present during the experiments with the wire-loop antenna are hardly perceptible in Figure. While the wire-loop antenna posed a source for highly located fields, a relatively large object like the limiter does this only at the edges, highlighted by a red arrow.

Signals from the RF probes are shown in Figures 5.16 and 5.17 as a function of the probe manipulator coordinate L_1. The location where the distance between the probes and reference points #1 and #2 is minimal is highlighted in the Figures. Figure 5.16 shows data from two scans, each composed of six consecutive discharges to cover most of the RF profiles. The discharges *1212-1217 differed from discharges *1225-1231 in P_{for} that was either about 55 W or 35 W, respectively. Hereby, the plasma density was changed, as can be seen in the subplot on the right. The difference in $\langle I_{sat} \rangle$ is especially pronounced in the region $L_1 \approx 80$ mm to 200 mm, but it also appears above.

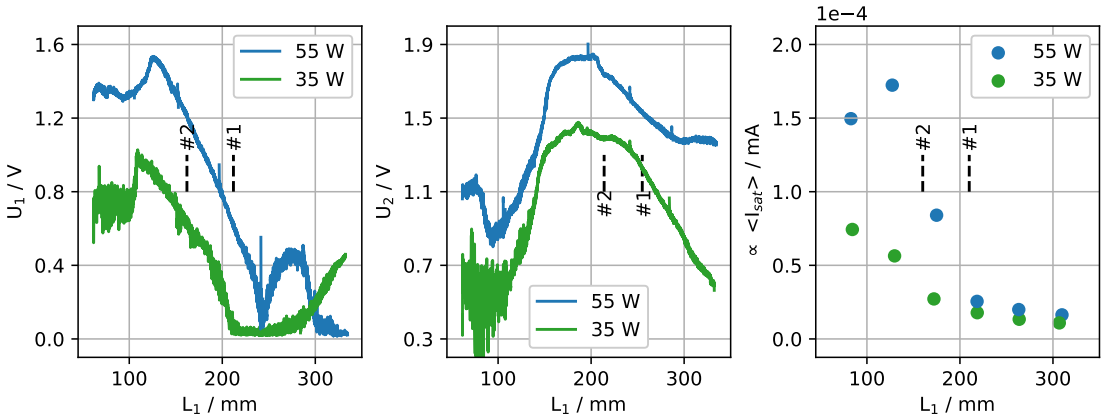

Figure 5.16: RF and Langmuir probe signals at different P_{for}, $f = 99$ MHz

While the difference in the RF probe signals is partially caused by the different RF power levels: $10 \log_{10}(35/55) \approx 2$ dB $\leftrightarrow 0.1V$, it is possible to observe changes in the profiles. The maxima in the profile from RF probe 1 shift toward lower L_1. The minima and the smaller local maxima in the range between 200 mm to 350 mm, on the other hand, distort towards larger L_1. The signals from RF probe 2 are broader at lower power levels. A spread of the profiles at lower densities, as expected from theory, is realistic.

In Figure 5.17, two radial scans at different RF frequencies are compared. In the discharges *1235-1240, the frequency was changed to 87.4 MHz. The $\langle I_{sat} \rangle$ is similar, especially above $L_1 > 200$ mm, eliminating density-dependent changes. Based on $\tan\theta = \omega/\omega_{pe}$, a compression of the profiles by $\omega_1/\omega_2 \approx 13\,\%$ is expected. It is possible to observe changes in the shape of the profiles of RF probe 1, but only barely in the signals of RF probe 2.

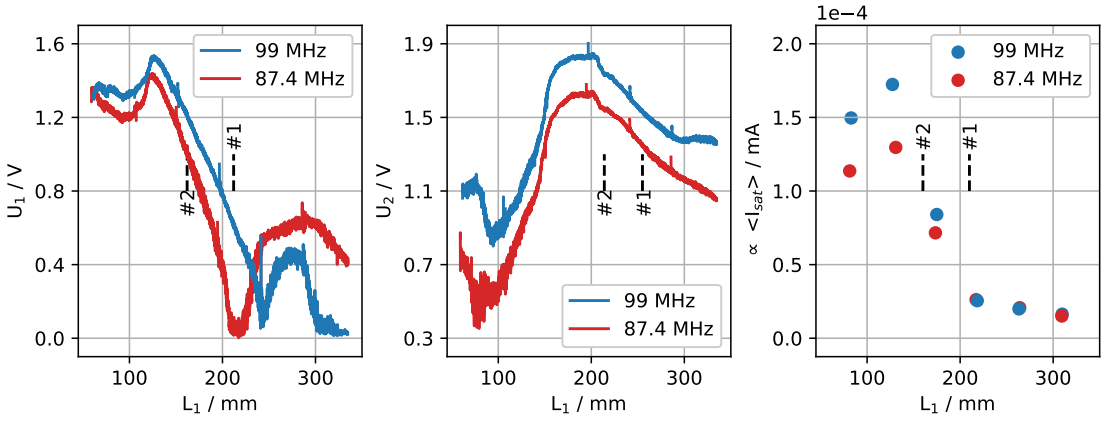

Figure 5.17: RF and Langmuir probe signals at different f, $P_{for} \approx 55\,\mathrm{W}$

The experiments on IShTAR showed that:

- RCs were launched from the wire-loop antenna and (possibly) from the limiter tile;
- the RF probes, including the electronics periphery, are a viable method for detecting the RCs;
- a simple geometric model describes the measured signals.

The findings were used to design a set of experiments to study the propagation of RCs in the AUG SOL.

Chapter 6

ICRF slow waves in ASDEX Upgrade

The work that is described in the previous chapters culminated in a set of experiments that were performed on the ASDEX Upgrade tokamak. The results relevant to this chapter are revisited concisely:

Chapter 1 introduced the research questions: "Do RF signals in the ICRF propagate as slow waves in the SOL of a reactor-relevant tokamak?", "Is this an unwanted path for RF power flows?" and: "Does this pose a mechanism that transfers sheath rectification processes to places that are far away from the original RF source?". The theoretical overview in Chapter 2 introduced fundamental concepts involving a description of the propagation of electromagnetic waves through a plasma. The location of ICRF waves within the theory was identified, and the different solutions to the dispersion relation were discussed. RCs were presented as a particular solution of the slow wave solution type. Chapter 3 provided an overview of the ASDEX Upgrade tokamak involving a brief description of the magnetic field topology, common plasma parameters, and the ICRF antennas. Based on this information, together with the knowledge of how waves propagate through the plasma, the radio frequency was chosen to be at or around $f = 100\,\mathrm{MHz}$. This relaxes the required precision on the experimental apparatus while the qualitative nature of the original problem remains. Simulations with the RAPLICASOL procedure, Chapter 4, showed that perturbations in the electric field are predominately defined by RCs in the ICRF slow wave parameter space. The goal is to study the propagation of ICRF slow waves, therefore constricts in this work to the study of RCs. A heuristic model was set up that explains the path of the ICRF slow wave through the plasma. Experiments on the ion sheath test arrangement (IShTAR), Chapter 5, supported this approach and validated the use of probes to detect RCs in a low-density plasma.

When the experiments on AUG were conceived, it was intended to follow the approach that was used in the experiments on IShTAR. However, significantly higher heat flows from the plasma and limitations in the tokamaks operational parameter space made multiple changes necessary. Figure 6.1 shows schematically a toroidal cross-section of AUG together with further annotations that describe the new experimental concept in principle. RF power is sent via a coaxial cable to a single

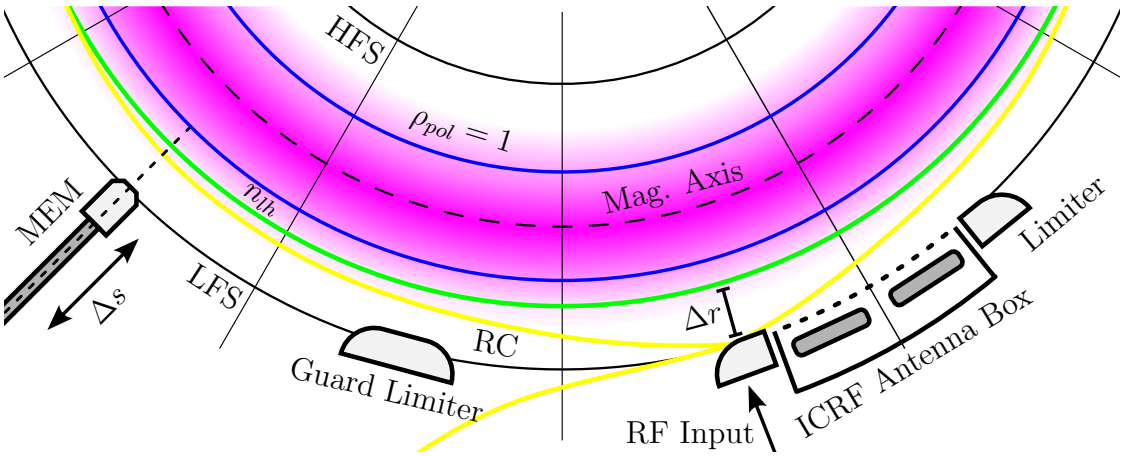

Figure 6.1: Schematic visualization of the concept of the experiments on AUG

tile of the ICRF antenna limiter (RF input). Based on simulations in Chapter 4, it is expected that RCs (yellow curves) emerge from the limiter tile when the plasma density is below the lower hybrid resonance density n_{lh}. The layer where $n_e = n_{lh}$ is in AUG in most experiments behind the limiter. To study propagating slow waves, the layer was intentionally relocated in front of the limiter for this work. Phenomena typically confined to the limiter can now be found in front of the limiter in a narrow low-density region Δr. The launched signals propagate through the layer and are then detected, at some distance from the source, by probes that are quickly plunged a distance Δs into the torus by the mid-plane-manipulator (MEM). To identify the wave type, the known dependence of the RCs on the plasma density and the radio frequency is tested. With a flexible magnetic topology in AUG, it is also possible to verify the dependence of the signal path on the magnetic field orientation.

6.1 Experimental setup

In the experimental campaigns at AUG from 2020 to 2022, different approaches to realize the experimental concept were explored. The setup used in most of the experiments is described in the following. In the first step, a schematic overview of AUG's LFS is introduced, simplifying later discussions. Afterward, it follows a detailed description of the wave source components, i.e., the limiter tile and the modifications that were made to them. In the next step, the probes at the MEM are discussed. The section ends with a detailed schematic showing the anticipated power flow from the RF source, through AUG, to the RF detectors.

Figure 6.2 shows a section of a schematic of the outer wall of AUG. Outer wall is a collective term for plasma-facing components that are located on the LFS. To enable explicit references, AUG is divided into 16 sectors, each spanning a toroidal angle of $\Delta\phi = 22.5°$. Figure 6.2 covers approximately 4 sectors, starting at sector 8 up to sector 11, counting upwards from right to left. ICRF antenna 3 is

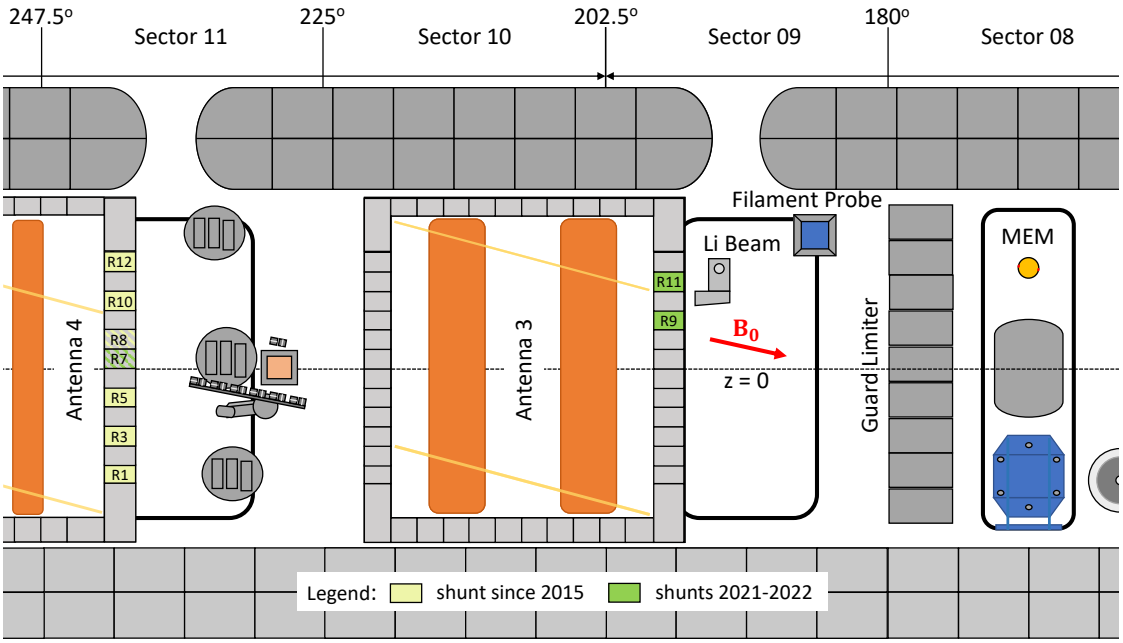

Figure 6.2: Schematic of a section of the outer wall of AUG [38]. Background magnetic field in red $\vec{B}_0$ from #40446 *at* $t = 6\,\mathrm{s}$

located in the center of the Figure, in sectors 10 and 9. ICRF antenna 4 is located predominantly in sector 12 but extends into the Figure in sector 11. Figure 6.2 shows also the location of some of the diagnostic systems that are relevant in later sections: the outlet for the lithium beam of the lithium beam diagnostic (Li Beam) in sector 9, and the before-mentioned mid-plane-manipulator (MEM) in sector 8. The dashed horizontal line in the background indicates the $z = 0$ reference. The red arrow represents the background magnetic field vector $\vec{B}_0$ during a typical reference discharge with standard helicity.

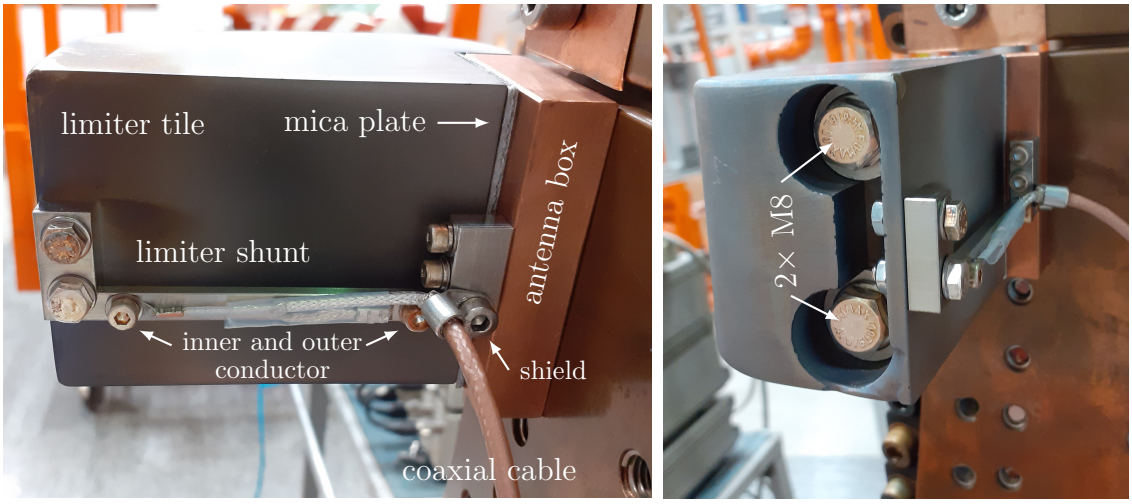

Figure 6.3: Pictures of the back and the side of a single limiter tile with a shunt and a coaxial cable mounted to a mock-up.

The ICRF antennas are surrounded by a rectangular array of graphite tiles, the so-called antenna limiter; see also Section 3.2. While most of the individual tiles of the limiter are electrically in direct contact with the antenna, some of them are insulated from the antenna box and connected to it only via a so-called shunt. These tiles are colored yellow and labeled RXx, identifying them as the Xx-th element of the right side of the antenna limiter labeled from bottom to top. A prototype of such a setup is shown in the two pictures in Figure 6.3 where a single limiter tile, mounted to a mock-up, is shown from the back and the side. The tile is pressed onto the antenna box by two M8 screws that exert a force onto counter bores via a set of cup springs. Electrically, the tile and the antenna box are insulated by a 2 mm thick mica plate. The limiter shunt is a 65 mm long rod of Inconel, a nickel-chromium-alloy, with a rectangular $3\,\text{mm} \times 6\,\text{mm}$ cross-section that merges at both ends into cuboids. On one end, the shunt is in direct contact with the outermost edge of the limiter tile. On the other end, the shunt is connected to the antenna box only. Attached to the shunt is a coaxial cable with a second outer conductor as an additional shield. The shield and the outer conductor are connected to the shunt relatively close to the antenna box. The inner conductor is connected to the limiter shunt close to the edge of the tile. The coaxial cables lead out of the torus to a filter box that splits any signal in a low frequency and an RF part. Both are measured, and the data are stored. This setup serves two purposes: First, it allows to measure any low-frequency electric current that flows from the plasma through the limiter tile to the antenna frame, and second, it acts as a receiving antenna that pics up RF signals that are present in the vicinity of the limiter tile. It thus presents a method to evaluate the RF fields that are induced in the limiter during the operation of the ICRF antennas.

In most experiments conducted for this work, RF power was sent toward the limiter tile - shunt assembly instead of using it as a diagnostic tool. Considering the accessible magnetic field geometry described in Section 6.2, two limiter tiles at ICRF antenna 3 (R9 and R11 in Figure 6.2) and two tiles at ICRF antenna 2 (L1 and L2 in Figure 6.12) were identified as promising launching points and equipped with shunts in a configuration that is similar but in detail different from the diagnostic setup. The differences are:

- the coaxial cables that are used for diagnostic purposes are incapable of handling higher power flows and were replaced by a different, thicker cable;
- the second shield and the outer conductor were connected to one of the screws that mount the shunt to the antenna frame;
- the coaxial cable's dielectric around the inner conductor was preserved and the inner conductor was connected to the outermost point of the shunt;
- the capacitive elements of the circuitry were changed.

The first three modifications are visible in Figure 6.4. The Figure shows the new configuration in AUG at ICRF antenna 3, specifically on tile R11. The coaxial cable is encased by ceramic sleeves to prevent arcing between the outer conductor

and other components in the tokamak. The places where the outer and the inner conductor are connected to the shunt in the new configuration are highlighted with green arrows.

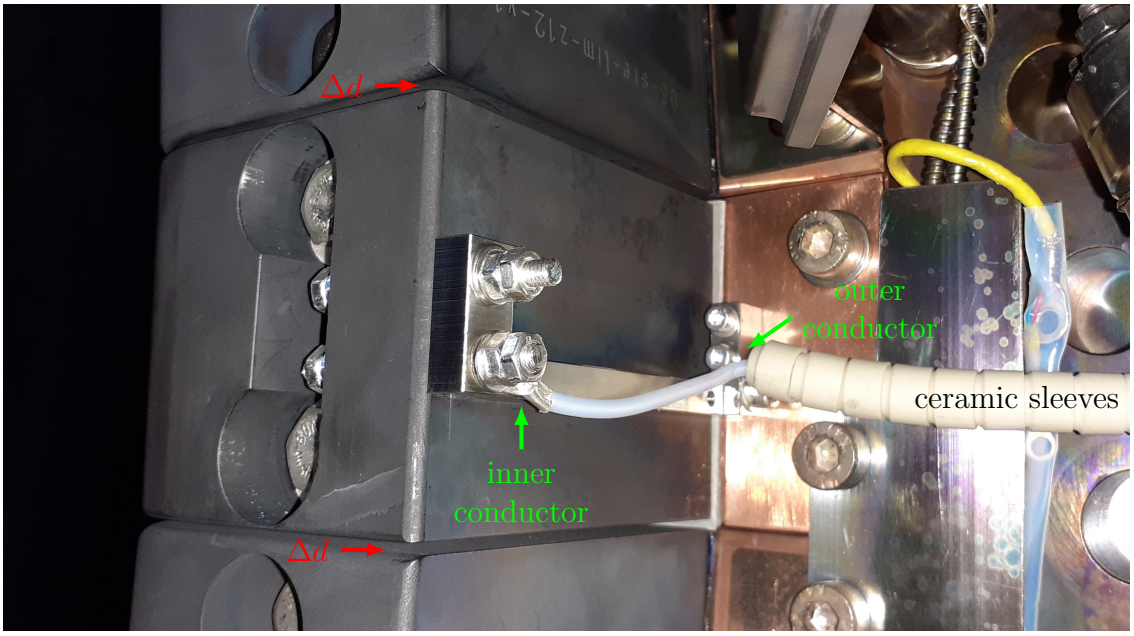

Figure 6.4: Pictures of the back of limiter tile R11 at ICRF antenna 3 (October 2021)

The fourth modification in the list is technically relatively subtle and not noticeable in Figure 6.4. It relates to how much of the RF power that is sent to the limiter tile - shunt assembly radiates into the torus. The parameter that determines this is the complex-valued reflection coefficient S_{11}. In a passive network, $T = 1 - |S_{11}|^2$ is the fraction of power that is transmitted. In tests at the mock-up, it was observed that the reflection coefficient of the assembly responds sensitively to changes in the distance Δd between the active and the adjacent passive limiter tiles. The gap Δd is highlighted with red arrows in the Figure for clarity. The same was observed when the width w of the mica plate between the limiter tile and the antenna box was changed. Both observations indicate the importance of capacitive coupling between the active tile and its surrounding elements. This allowed for RF matching, the systematic manipulation of the reflection coefficient.

Typically, it is beneficial to maximize the transmitted power T. For limiter tile R9 and R11 at ICRF antenna 3, this was achieved by reducing the capacitive elements. The distance Δd was increased from $\leq 0.5\,\text{mm}$ to $\leq 2\,\text{mm}$, and the width of the mica plat was doubled to about 4 mm. Further, the diameters of the M8 screws within the limiter tile were reduced to about 6 mm. The screws within the boreholes represent two cylindrical capacitors with non-negligible capacitance, especially since a ceramic tube ($\varepsilon_r \approx 10$) is used to insulate the screws from the limiter tile. The reflection coefficient S_{11} was measured with a vector network analyzer (VNA) that was connected to the end of the coaxial cables outside of AUG. This is shown in Figure 6.5 in the Smith chart representation where a frequency

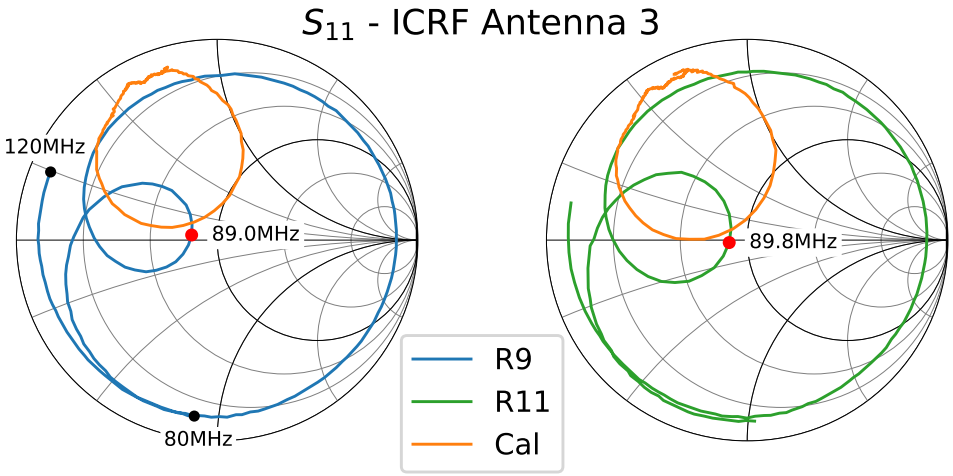

Figure 6.5: Reflection coefficient of the limiter tile - shunt assemblies at R9 and R11 at ICRF antenna 3 measured at the feedthroughs

range from 80 MHz to 120 MHz is covered. The coaxial cable creates a marginal damping but imposes a significant phase shift onto the measurements. Effectively, this creates a frequency-dependent clockwise rotation of the data points in the Smith chart. It is possible to subtract this phase delay. The resulting calibrated, phase-corrected data points are colored orange in the Figure. The calibrated reflection coefficient matches the expectations that the system behaves like a small resistance, left from the center, in series with an inductance, above the horizontal line. The circle-like shape originates from resonances between the internal components. The distance from the data points to the center of the Smith chart (normalized to its radius) represents the fraction of transmitted power. The point of maximal transmission, around 89 MHz to 90 MHz, is highlighted with red dots. Most of the experiments were performed with limiter tile R9. The frequency of the RF waves that were used during most of the experiments (the default) was changed from the intended 100 MHz to the point of maximum transmission at 89.5 MHz. (The maximum transmission point shifted slightly between installation and the experiments.)

In contrast to the limiter tiles at antenna 3, it was necessary to increase the capacitive elements at limiter tiles L1 and L2 at ICRF antenna 2. The geometrical size of the limiter tiles is smaller, and the capacitive coupling to the neighboring tiles is consequently weaker. The capacity was increased by adding a short, open-ended piece of coaxial cable to the setup. Figure 6.6 shows two pictures of the back of limiter tiles L1 and L2 at ICRF antenna 2. In the right picture, the cables disappear behind a steel bar that is part of the support structure of AUG's passive stabilizing loop. The picture on the left shows a region behind the steel bar where the cables continue. The same cables are designated by letters in both pictures. Cables A and C lead to vacuum feedthroughs and allow the RF power transfer. Cables B and D are the short cable pieces that were added as capacitive elements. Cable E is the diagnostic cable originally connected to the shunt at limiter tile L1. It is without function but was left in place to simplify a possible reversal of the

Figure 6.6: Pictures of the back of limiter tiles L1 and L2 (October 2021)

modifications. Despite several attempts, it was not possible to optimize the power transfer to the limiter tile - shunt assemblies at ICRF antenna 2 to values that are comparable to the parameters at ICRF antenna 3. The reflection coefficient for the limiter tile - shunt assemblies at L1 and L2 at ICRF antenna 2 are shown in Figure 6.7. It is further observed that the point of maximum power transfer is at 94 MHz.

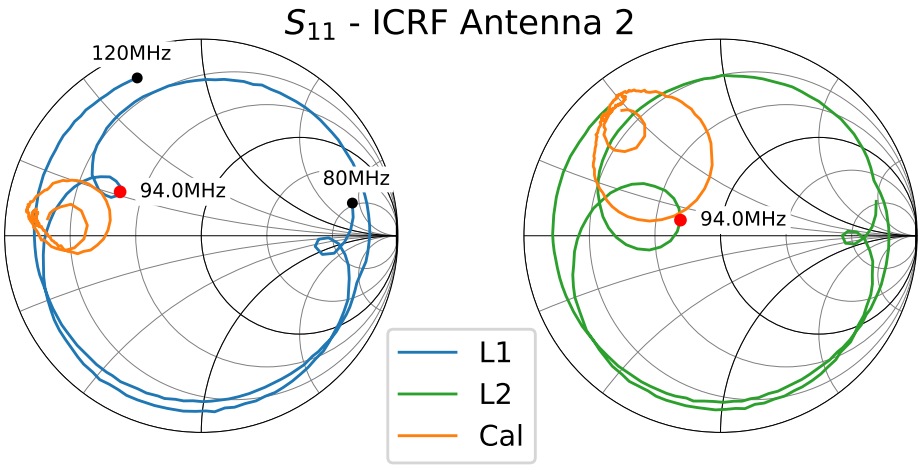

Figure 6.7: Reflection coefficient of the limiter tile - shunt assemblies at L1 and L2 at ICRF antenna 2 measured at the feedthroughs

After describing the setup from the source side, the detector side is addressed. Figure 6.8 shows the ball-pen probe head that was used in the experiments. The

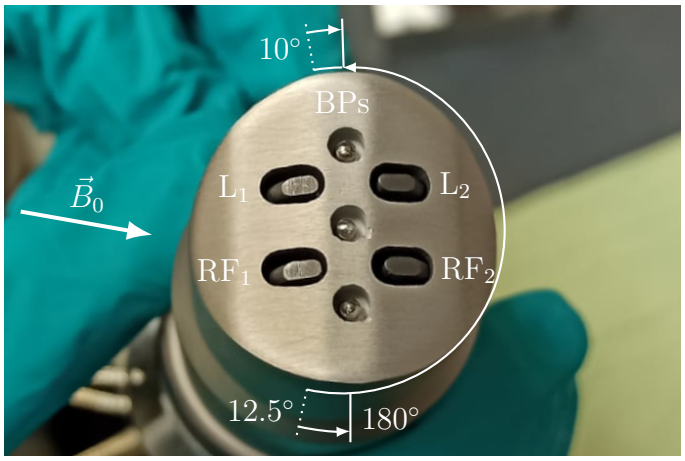

Figure 6.8: Ball-pen probe head for the AUG mid-plane manipulator

probe head was mounted to the, MEM which is located in AUG in sector 8; reconsider Figure 6.2. The probe head is equipped with seven probes. As discussed in Chapter 3, the three ball-pens (BPs) measure perturbation in the plasma potential. They are embedded in a vertically aligned section of the probe head that protrudes slightly. In the tokamak, this separates the two graphite pins on the left from the two pins on the right because the protruding section creates a shadowing effect along the background magnetic field $\vec{B}_0$. Two of the four flush-mounted graphite pins (L_1 and L_2) were used as Langmuir probes. To operate them as a Mach-probe, it is necessary to position them in line with the background magnetic field. In most of the experiments at AUG, the background magnetic field vector points at the MEM, within the outer wall schematic (Figure 6.2), to the right and downwards. To take this into account, the probe head is usually rotated clockwise by about 10°. In most of the experiments conducted for this work, the toroidal component of the background magnetic field was reversed. The background magnetic field vector at the MEM is then directed to the left and downwards. To test the influence of the probe head orientation, it was rotated counterclockwise by about 180° + 12.5° in some of the experiments. The two other graphite pins (RF_1 and RF_2) were operated as RF probes. The RF probes were realized based on the experience gained in the experiments on IShTAR, Chapter 5. The graphite pins remain on time average on floating potential plus an offset from the rectified RF fields as described in Section 2.3 because the coaxial line that connects the probes to the RF detectors is decoupled via DC breaks. DC breaks prevent the transition of low-frequency signals but allow RF signals to pass. The RF probes operate as short receiving antennas.

With the description of the limiter tile - shunt assembly as the source and the RF probes at the MEM as the detector, it is possible to describe the anticipated path of the RF signals through the experiment. Figure 6.9 shows a simplified schematic. It presents conceptually how the RF power flows through the individual components during most of the experiments that are described in later sections.

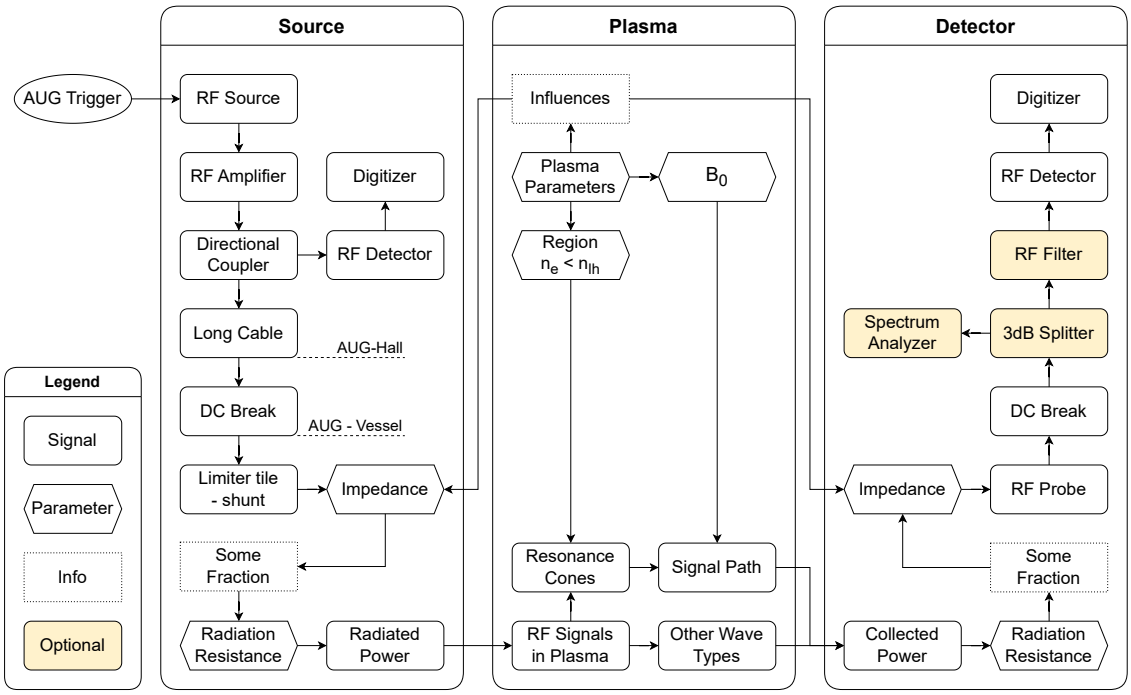

Figure 6.9: Simplified schematic of the expected power flow in the experiments on ASDEX Upgrade

The experiment is started by an external **trigger** from the **AUG** control system. The trigger starts an oscillator that emits pulses of RF signals with the intended frequency, for example, 89.5 MHz. The **RF source** is connected to an **RF amplifier**, which amplifies the input signal to several hundred-watt output power. To monitor the forward and backward power flow, a **directional coupler** is used. It redirects $< -40\,\mathrm{dB}$ of the signal to an **RF detector**. The RF detector measures the amplitude and phase difference between the forward and reflected power waves. The signal from the RF detector is then **digitized**, and the data are stored in the AUG shot file system. Most of the RF power transmits through the directional coupler to a relatively **long coaxial cable** with a length of $\approx 80\,\mathrm{m}$ that leads into the hall where AUG is located. Approximately 3 dB of RF power is lost in the long cable due to ohmic losses. In the AUG hall, the coaxial cable connects to a **DC break** that decouples the previous elements from the following components in AUG. The other side of the DC brake is connected to a vacuum feedthrough at the AUG - vessel. Inside the AUG vacuum vessel, a coaxial cable connects to the **limiter tile - shunt** assembly, as described before. The electric **impedance** of the setup, in particular the **radiation resistance**, determines how much of the injected power is radiated by the setup. In a passive network, the impedance Z is related to the experimentally accessible reflection coefficient by:

$$S_{11} = \frac{Z + Z_0}{Z - Z_0} \Leftrightarrow Z = Z_0 \left(\frac{1 + S_{11}}{1 - S_{11}}\right).$$

Here, $Z_0 = 50\,\Omega$ is the reference impedance. During experiments, it was observed that the reflection coefficient changed when a plasma formed in AUG. It is concluded

that the **plasma parameters** had an **influence** on how much RF signal is radiated from the source into the vessel. Some of the **radiated power** enters the plasma in front of the antenna limiter. Depending on the plasma parameters, the **RF signals in the plasma** propagate through the vessel in different wave types. In the region where the **plasma density is below the lower hybrid resonance density, RCs** form and propagate through the torus. As known from previous sections, the **signal path** depends on the plasma density and the orientation of the **background magnetic field**. RCs are only one wave type, and **other wave types** may contribute to the **collected power** that is received by the two **RF probes** at the ball-pen probe head. As with the launching structure, the RF probes have an electric **impedance**, with a fraction being the **radiation resistance**. It is plausible to assume that the RF probe impedance is **influenced** by the plasma parameters as well. The RF probes are connected via coaxial cable to a vacuum feedthrough at the MEMs infrastructure. Outside the AUG vessel, these cables terminate at **DC breaks**, which decouple AUG from the following components. To analyze the RF spectrum collected by the probes, a 3 dB **splitter** divides the signal into two parts. One part goes to a **spectrum analyzer**, the other to a **RF filter** that transmits only the originally emitted radio frequency. The RF signal that passes the RF filter is **detected**, and **digitized** and the data are stored in the shot file system.

With a general understanding of how the RF signals propagate through the experiment, it is left to specify the expected signal path of the RCs through the plasma. This is the key point of the next section.

6.2 Experimental process

A prerequisite for successful experiments is that RCs form and that they reach the probes. From theory and simulations, it is anticipated that RC emerge from the limiter tiles when the plasma density in the vicinity is below the lower hybrid resonance density. It was further observed that RCs open up along the curved background magnetic field and that the opening angle of the RC is determined by the local plasma density. Before discussing how this concludes into operational parameters for AUG, a preliminary remark is made:

In tokamaks, inside the separatrix, it is typically appropriate to assume that the plasma density is, on average, constant on the same flux surface. The reason for this is the high mobility of the particles along the magnetic field lines that equilibrate any differences in the parameters. In the SOL, this is ,in general, not the case. Specifically, in the volumes located radially behind the limiter - the limiter shadow - the path lengths between the points where the magnetic field lines intersect with the wall are short. The plasma dynamics in this region are complex, and the plasma parameters are typically difficult to diagnose. The conditions are different in the section of the SOL between the limiter and the separatrix. Here, the path lengths are relatively long, exceeding several meters, and it is plausible to assume some continuity along the magnetic field lines. Throughout the following work, as a first-order approximation, it is assumed that the plasma density that is determined by

the Mach-probes at the MEM remains about the same along the magnetic field lines.

The current section starts with discussing the requirements for the magnetic field geometry. Afterward, exemplary density profiles are shown, and their influence on the experimental process is discussed. The section ends with a description of how the experimental parameters were modified to identify the wave type of the RF signals.

Two regions, one at ICRF antenna 3 and one at ICRF antenna 2, were identified as promising launching points. Figure 6.10 shows a section of the LFS schematic with limiter tiles R9 and R11 at ICRF antenna 3 as two possible launching points. Because RCs follow the background magnetic field lines, a magnetic field geometry

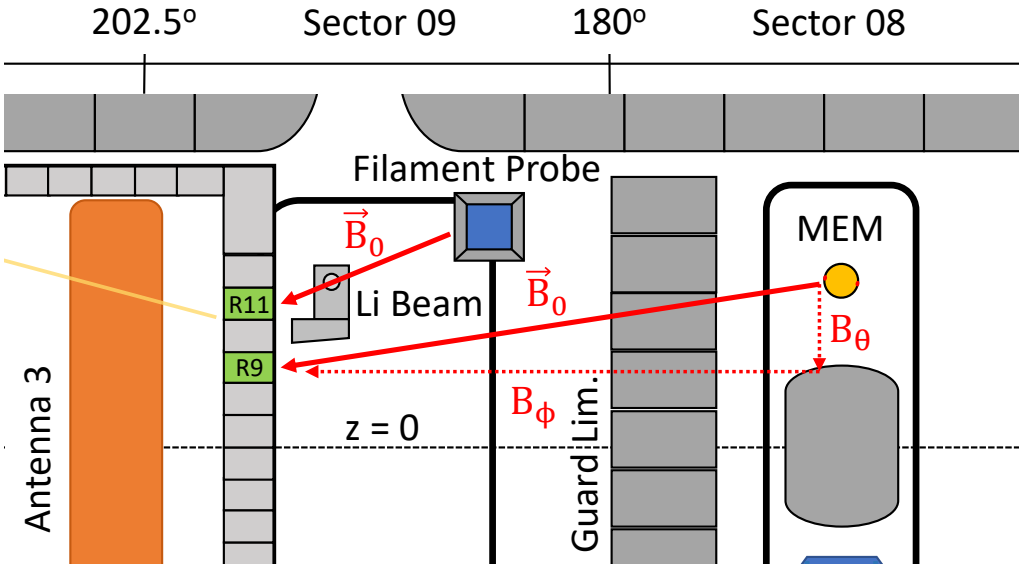

Figure 6.10: Schematic of a section of the outer wall of AUG. Magnetic field lines in red indicate the possible scenarios [38]

had to be found that connects the source to the probes. Two red arrows indicate schematically the direction of the background magnetic field lines that connect tile R9 to the MEM and R11 to the filament probe head. Experiments with the filament probe were not possible because of a mechanical defect of the probe during the experimental campaign (#39837 − 40). Experiments with limiter tile R9 as the source represent most of the conducted experiments. They require a relatively shallow magnetic pitch angle pointing from the MEM downwards to the limiter tile. The pitch angle $\tan\alpha = B_\theta/B_\phi$ of the magnetic field is on the outer wall defined by the toroidal B_ϕ and the poloidal B_θ field component. The toroidal field components are created by the current in the toroidal field coils and can, in AUG, be varied between $-3.2\,\mathrm{T}$ to $+3.2\,\mathrm{T}$. The typical sign convention is used, meaning that B_ϕ is positive in the schematic in Figure 6.10. The poloidal field component is primarily defined by the plasma current I_p. The sign convention is such that the magnetic field component at the outer wall is oriented downwards for a positive plasma current ($+\phi$ direction and right-hand rule). To choose the appropriate

operation parameters, AUG's database was searched for a magnetic topology that suits the requirements. Figure 6.11 shows a poloidal cross-section of an experiment on the left and two excerpts on the right.

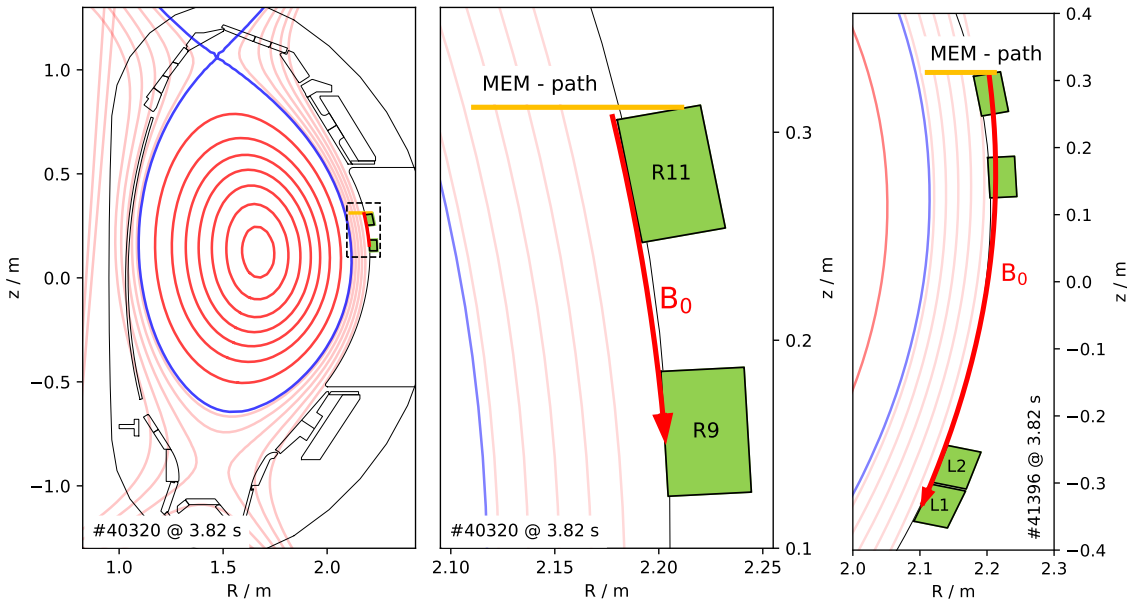

Figure 6.11: Schematic of a section of the outer wall of AUG. Magnetic field lines in red indicate the possible scenarios [38]

The blue and red curves are the separatrix and the flux surfaces. The green polygons represent the approximate location of the limiter tiles R9 and R11. The orange line is the path that the front end of the probe head covers when the MEM is plunged into the vessel. The thick red line in the excerpt $\vec{B}_0$ originates from a routine that traces the magnetic field line from the front end of the limiter tile backward to the toroidal angle of the MEM. The decisive magnetic parameters are $B_\phi = +2.5\,\mathrm{T}$ and $I_p \approx 0.73\,\mathrm{MA}$. The limiter tile R9 is magnetically connected to the MEM. Choosing the radially protruding point on the limiter tile had two reasons: The first is that simulations have shown that RCs emerge from the protruding section of the tile, specifically where the surface normal matches $\pi/2 - \theta_c$. The second is that signals that emerge from recessed points on the limiter tile can possibly terminate at the guard limiter (not visible in Figure 6.11) before reaching the MEM.

Figure 6.12 shows schematically the magnetic connection that was foreseen for the experiments with limiter tiles L1 and L2 at ICRF antenna 2 as the source regions. A defect at one of the coaxial cables inside AUG prevented experiments with tile L2. A magnetic connection between tile L1 and the MEM was found. The right excerpt in Figure 6.11 shows the connection of limiter tile L1 with the MEM path. The governing parameters for the L1 - MEM connection are $B_\phi = -1.8\,\mathrm{T}$ and $I_p \approx 0.9\,\mathrm{MA}$. As can be seen, the magnetic field line intersects with the limiter around $z = 0$ before reaching the MEM. RF signals can only reach the probe head if they enter the plasma in front of the limiter, for example, in the form of RCs that open up along the magnetic field line. The experiments with tile L1 as the

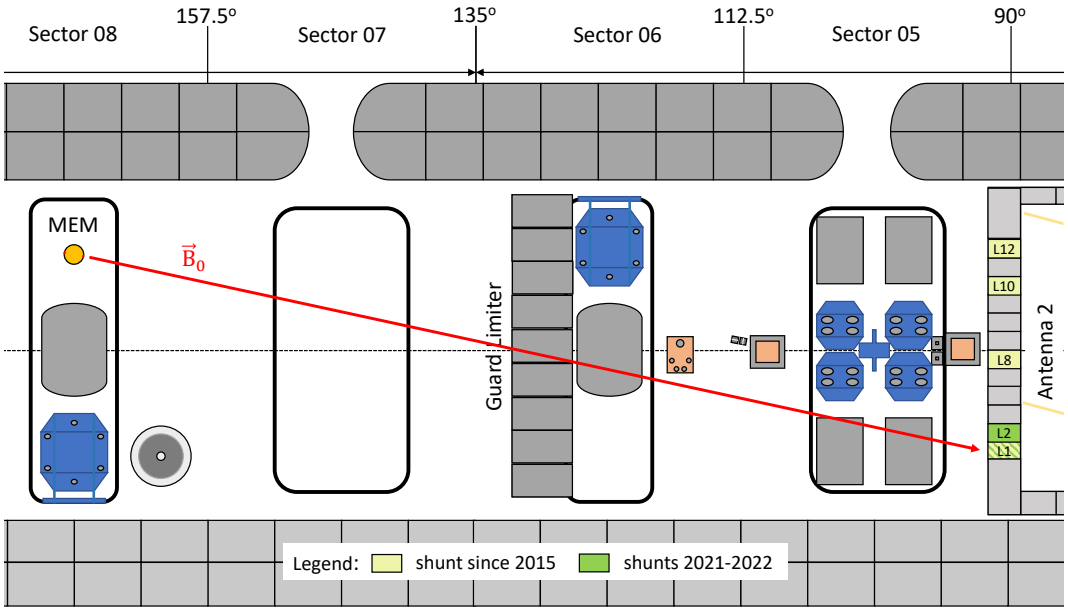

Figure 6.12: Schematic of a section of the outer wall of AUG. Magnetic field lines in red indicate the possible scenarios [38]

source were primarily aimed at verifying the results that were acquired with tile R9 as the source. The tile is not only on the other side of the MEM, meaning it faces RF probe 2 instead of RF probe 1, but also the path length between the tile and the MEM is significantly longer, about $L_{L1} \approx 3\,\mathrm{m}$ vs about $L_{R9} \approx 1\,\mathrm{m}$. If signals reach the MEM, they have covered a toroidal angle of about 80° of the tokamak. Additionally, the background magnetic field vector points from the MEM downwards to the tile. This configuration is similar to the standard helicity.

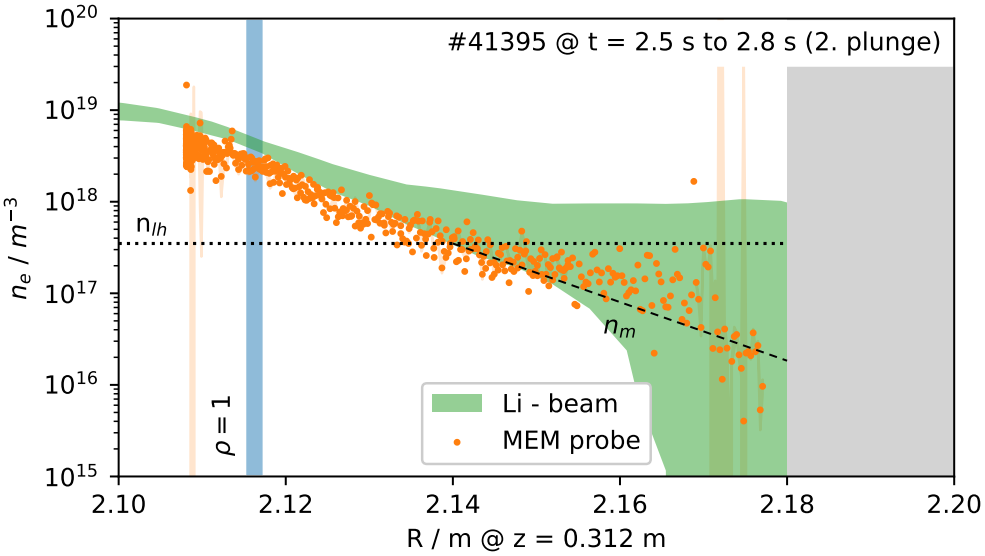

Figure 6.13: Density profiles from the Mach probe and the lithium beam diagnostic mapped to the MEM path

After discussing the magnetic connection between the source and the detector region, the density profile is addressed. The requirement was to find operational parameters for which the plasma density in front of the limiter is below the lower hybrid resonance density n_{lh}. In a tokamak and the frequency range of interest, n_{lh} depends weakly on the magnitude of the background magnetic field; see also Figure 3.7. With a frequency of $f = 89.5\,\mathrm{MHz}$, it is according to Equation (2.25) in the range between $n_{lh} = 3.8 \times 10^{17}\,\mathrm{m}^{-3}$ to $3.4 \times 10^{17}\,\mathrm{m}^{-3}$ with a respective B_0 from 1.0 T to 3.0 T. Most diagnostics can not resolve these differences reliably. For designing the experiments, a single data point $n_{lh} = 3.5 \times 10^{17}\,\mathrm{m}^{-3}$ was used. Figure 6.13 shows a density profile from a discharge with a dedicated low-density SOL. It shows data from the lithium beam and the Mach probe diagnostics that were acquired over the course of a single MEM plunge. The data from the lithium beam were mapped to ρ_{pol} and then back to the R and z coordinates of the MEM. A general agreement between the data can be observed. It is plausible to assume that either of the profiles has to be shifted radially with respect to the other by half a centimeter to achieve a better agreement. The discrepancy can originate from imperfection in the experimental process, but it is also possible that this is an actual difference in the local density profile. The lithium beam data lose applicability around $R = 2.16\,\mathrm{m}$ where the error becomes large.

Besides the data points, the Figure contains additional information. The vertical blue line on the left-hand side shows the location of the separatrix for this particular experiment. The gray area on the right-hand side indicates the location of the limiters at the height of the MEM $z = 0.312\,\mathrm{m}$. The dashed horizontal line in the center indicates the lower hybrid resonance density n_{lh}. It is apparent that there is a layer with a width of several cm in front of the limiter in which the density is below the lower hybrid resonance density. The ICRF slow wave consequently propagates in this region.

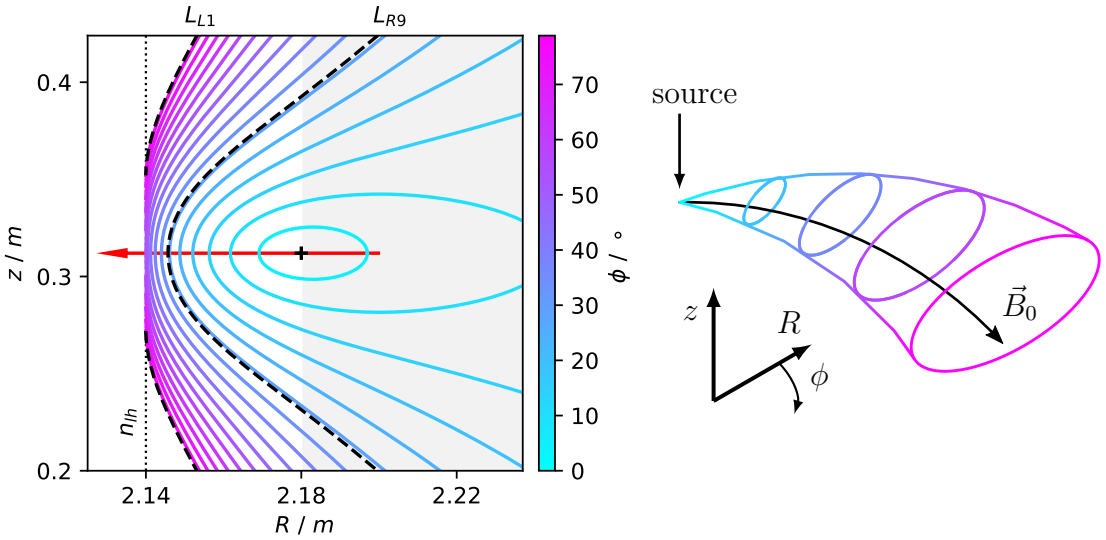

Figure 6.14: Contour plot of a RC that gets distorted at an exponential density gradient and schematic illustrating the model

With the plasma density profile at the limiter, it is possible to model how a RC opens up along the background magnetic field line. This is shown in Figure 6.14. Consider first the schematic on the right-hand side of the Figure. The magnetic field is oriented purely in the toroidal direction in this simplified model. The RC emerges from a point source. The colored curves are the cross-section of the RC at different points along the path from the source to the maximum toroidal angle. Now consider the plot on the left-hand side of the Figure. It shows the cross-sections computed with an algorithm projected onto the zR-plane. The density profile is approximated by an exponential function $\log_{10}(n_m) = a(R_0 - R) + b$, with $a = 32\,\mathrm{m}^{-4}, b = n_{lh}, R_0 = 2.14\,\mathrm{m}$, creating a density profile that is comparable to the experimental observation, see also Figure 6.13. The curves show the expected behavior: the section of the RC that enters the lower density regions (larger R) leaves the plasma while the section that enters the higher density region (smaller R) approaches the lower hybrid resonance density at 2.14 m eventually. The point where the toroidal angle represents the distance from the tile R9 to the MEM $L_{R9} \approx 26°$, and the tile L1 and the MEM $L_{L1} \approx 79°$ are highlighted by black dashed lines. In an idealized scenario, the MEM plunges the probe horizontally through the RCs as indicated with the red arrow. An important conclusion from this analysis is, that a RC that emerges from tile R9 does not reach the lower hybrid resonance layer on the path towards the MEM. The path length is simply not large enough to reach that layer.

With an expectation on how RF signals propagate through the tokamak, it is left to specify how to validate the presence of RCs in the experiment. Three approaches were identified:

1. by scanning the plasma current I_p;
2. by scanning the outermost separatrix position R_{aus};
3. by changing the frequency of the RF waves.

Scanning the plasma current changes the pitch angle of the magnetic field, as indicated schematically in Figure 6.15. The Figure represents an experiment where the plasma current was scanned in six steps from about 430 kA to 930 kA. The pitch angle increases with higher plasma current (purple arrow), and a height difference of approximately $\Delta z \approx 1.8\,\mathrm{cm}/100\mathrm{kA}$ was observed experimentally for the connection from the tile R9 to the MEM. With a scan of the plasma current, it is possible to test if the signals are bound to the background magnetic field lines. The RC is moved past the MEM, and it is tested if this manifests in different RF field amplitudes.

The purpose of scanning R_{aus} is to move the density profile in front of the limiter tile radially. The geometrical location where the RF signals are detected must move if the detected signals propagate in a particular density layer. This identifies the signals as ICRF slow waves. The magnetic parameters were constant during a R_{aus} scan and chosen such that the source region connects magnetically to the detector.

The last parameter that can be changed to validate the observations is the wave frequency. As in the experiments on IShTAR, changing the frequency of the wave

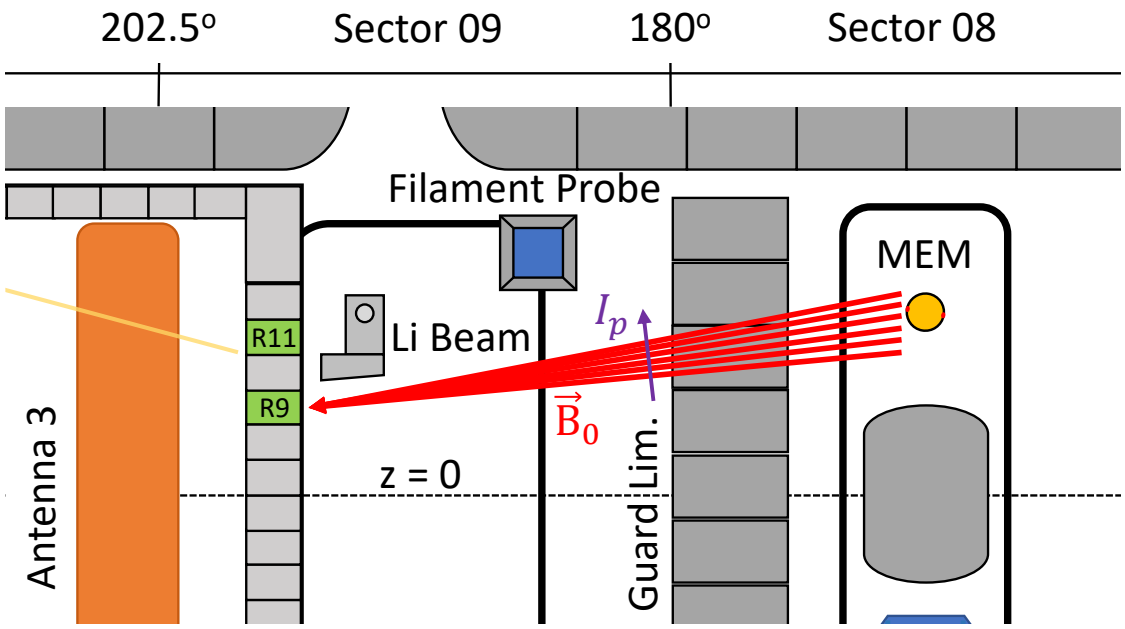

Figure 6.15: Schematic showing the different magnetic field lines intersecting with limiter tile R9 for different I_p

changes the RC opening angle and the lower hybrid resonance density. It is expected that the signals propagate at lower RF frequencies (for example, $f_2 = 50\,\mathrm{MHz}$) in an even narrower layer in front of the limiter.

6.3 Raw data, post-processing, and analysis

This section starts by presenting time traces of data that were recorded during the experiments. It explains the post-processing steps that were applied to the data to extract information and discusses apparent observations. The section ends with a paragraph that concludes the findings.

Time traces

Figure 6.16 shows time traces of relevant signals. The title of the Figure contains information on the individual experimental discharge: the discharge identification number (Shot Nr.), the toroidal field in T, the type of the experiment, the limiter tile that was utilized as the source, the frequency of the oscillator, and the angle of the probe head (see Figure 6.8). The Figure covers a period of about $t = 4.5\,\mathrm{s}$, a common discharge length for these experiments at AUG. The individual rows of the Figure show the plasma current I_p, the outermost separatrix position R_{aus}, the position of the MEM L_{MEM}, two signals S_{for} and S_{ref} representing the RF power that flows towards P_{for} and is reflected P_{ref} from the limiter tile measured with the directional coupler, and the two RF signals S_1 and S_2 that were detected by the RF probes 1 and 2 at the ball-pen probe head. Traces of data from the Mach probe

are not shown. Extracting density profiles from these data is a common task, and established routines exist.

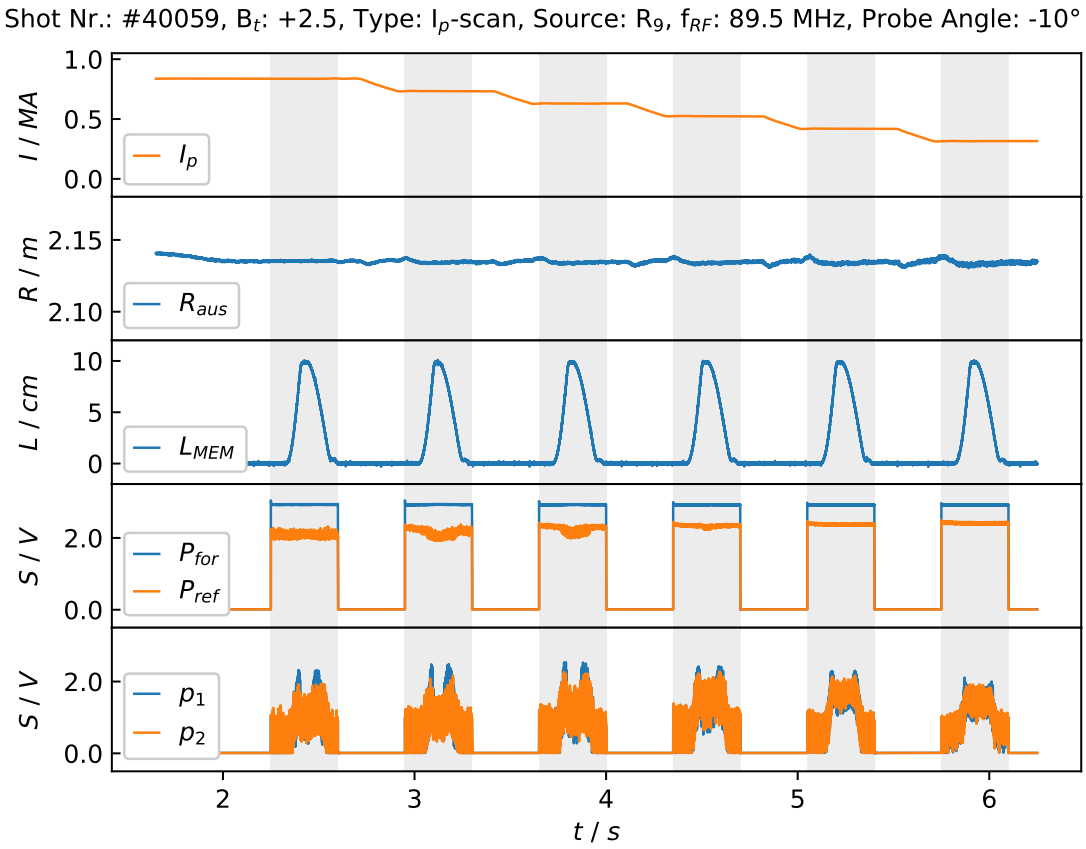

Figure 6.16: Time trace of relevant parameters from discharge #40059, an I_p scan experiment with tile R9 as the source

From the plasma current, the experiment can be identified as an I_p scan, where I_p was scanned in steps downwards from about 840 kA to 320 kA. The outermost separatrix position was kept constant at about 2.135 m throughout. The signal that represents the position of the MEM shows the six intervals in which the probe was plunged into the plasma and retracted from it. As in the experiments in IShTAR, the RF signals were measured using detectors with a logarithmic response of about 50 mV/dB. There are two relevant observations in the signals from the directional coupler S_{for} and S_{ref}:

The first is that the reflected power S_{ref} increases towards lower plasma currents. This is presumably caused by an increase in the plasma density at larger radii that accompanies the reduction of the plasma current, see Figure 6.17. (The solid lines approximate the density profiles using a generic model function:

$$n_e(R) = n_k - \log_{10}(10^{a(R-R_k)} + 10^{b(R-R_k)})/\mathrm{m}^3,$$

with R_k and n_k, the location of and the density at the knee. a and b are the slopes of the two regions.) The reflection coefficient of the tile depends on the electric

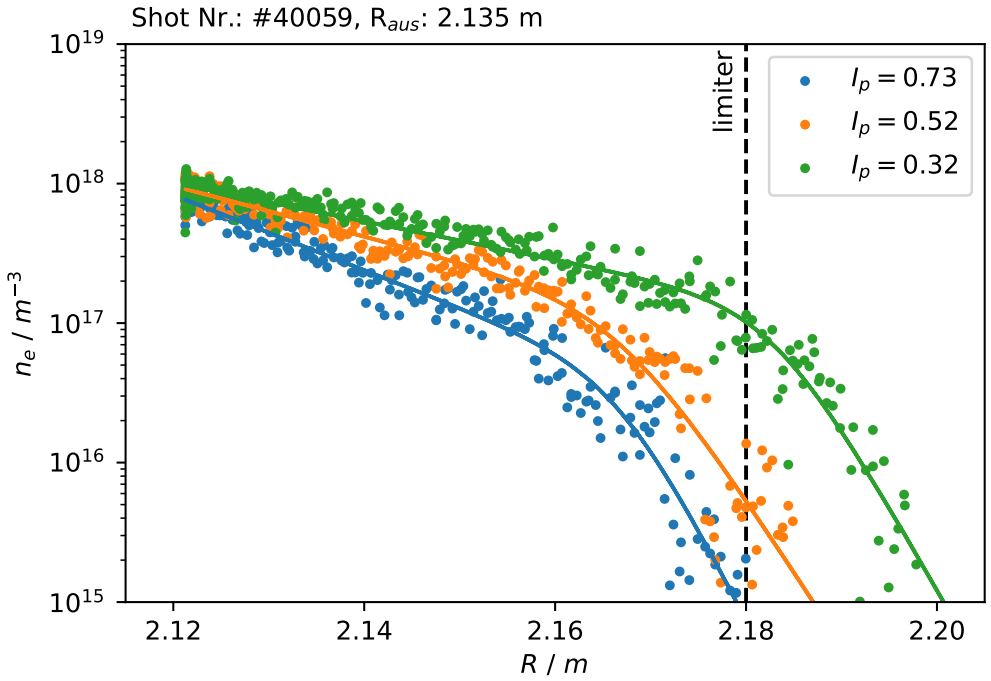

Figure 6.17: Density profiles from the Mach probe at different plasma currents corresponding to plunges 2, 4, and 6 in experiment #40059

impedance of the limiter tile - shunt assembly, which is modified by the presence of the plasma. The influence changes if the plasma gets closer to the tile. The physical mechanism that causes the density increase at larger radii is possibly that the length of the open magnetic field lines increases when the plasma current is reduced. Longer field lines maintain higher plasma densities.

The second relevant observation in the S_{ref} signal is that it reacts to the MEM plunges in plunges two and three. This corresponds to the magnetic connection of the tile with the MEM at 730 kA (2nd plunge). At 630 kA (3rd plunge), the magnetic field line terminates about 1.8 cm lower, and the tile can, in principle, still connect to the probe head because of the finite size of the tile and the probe head. This indicates that the MEM alters the plasma parameter slightly. Consequently, the coupling of the RF signals from the tile into the plasma is different. However, the change in power flow is small and neglected in the following analysis.

The signals from the two RF probes, S_1 and S_2, show four relevant observations ① - ④:

Observation ① is that the probes pick up RF signals at the moment when RF power is sent to the tile whether the probe head is retracted behind the limiter or not. The signal amplitude is more than 1 V below the maximum signal amplitude. This is 20 dB, or on a linear scale, a factor of 100, below the maximum. While negligible in amplitude, it opposes the (simplified) hypothesis of how RF signals propagate through the torus. Since the RF detectors do not discriminate between RF frequencies, it was suspected that the measurements are corrupted by harmonics

of the signal that arise, for example, from non-linear interactions of the signal with the plasma sheath. Signals with a frequency of $2f$ or higher correspond to different points in the dispersion relation and can reach the probes on different paths. These observations motivated to branch off half of the signal from RF probe 1 and feed it into a spectrum analyzer, see also Figure 6.9. The spectrum analyzer was programmed to scan a range of about 100 MHz with a scan rate of about 100 Hz. Figure 6.18 shows two spectra from the 2nd plunge in discharges #40900 and #40901, in which RF power was sent to the tile. The frequency of the RF

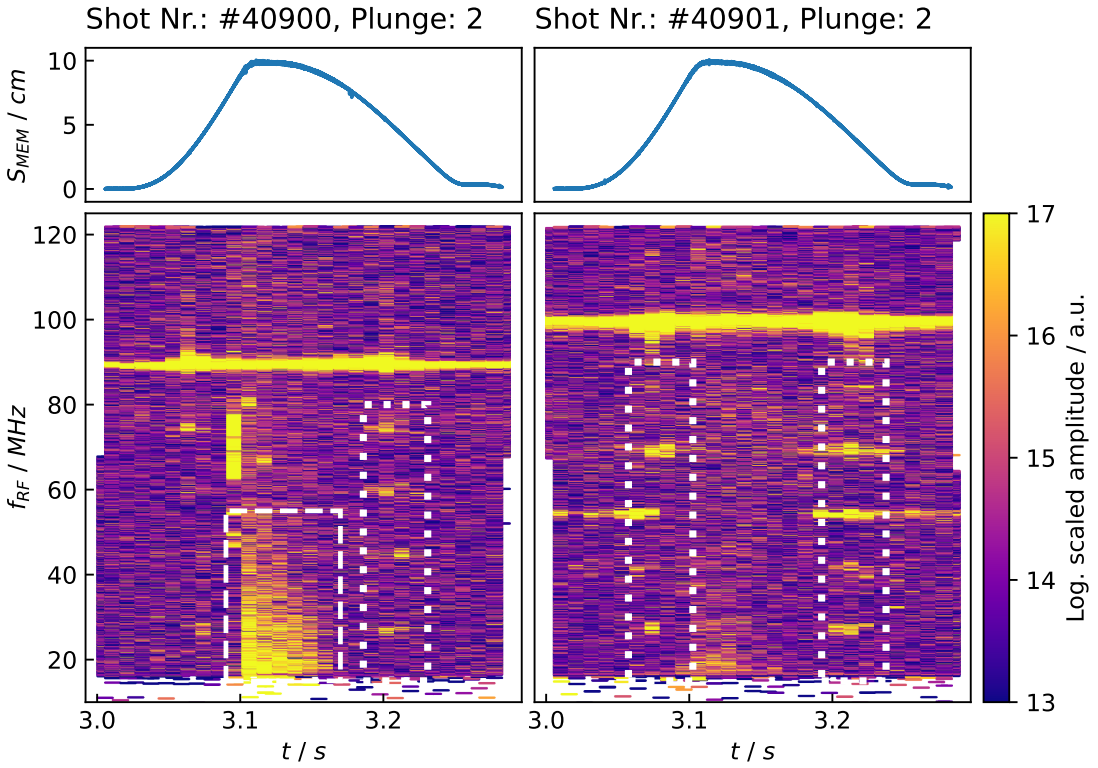

Figure 6.18: RF spectrum from RF probe 1 during the 2nd plunge in #40900 and #40901, with limiter tile R9 as the RF source

power that was sent to limiter tile R9 was 89.5 MHz and 100 MHz respectively, visible as (intense) horizontal lines in the spectra. The spectrum measured during discharge #40900 shows a broadband component, white dashed rectangle, ranging from 15 MHz to 55 MHz. Besides the broadband signals, the spectra show several peaks highlighted with white dotted rectangles. The signals are radially localized in a layer with a width of less than 1 cm. Notice that the frequency of the peaks depends on the injected frequency of the wave. This suggests that the injected RF signal decays into secondary signals with (lower) frequency at certain locations in the plasma. The RF broadband signal and peaks are independent observations. Both were observed without the presence of the respective other. To suppress the signals with different RF frequencies, an RF bandpass filter was installed between the probes and the RF detector; see also Figure 6.9. However, the low-power

background signal remained. This observation indicates that the injected RF signals do not propagate exclusively as RCs through the torus. The detected signal is rather a superposition of signals of (possibly) different wave types.

Observation (2) is that the measured signals show symmetry regarding the probe head's path L_{MEM}. The signal that is recorded when the probes are plunged into the plasma is about the same when they are retracted. On the way inwards, the probe measures an increase in signal amplitude up to a point where it suddenly drops.

Observation (3) is the wide fluctuation range of the data points. The fluctuation of the amplitude is enormous, considering the logarithmic scale. The signal fluctuation may result from plasma intermittency that disturbs the experimental process. Figure 6.19 shows the spectrum of signal S_1 during the 2nd plunge. Starting from

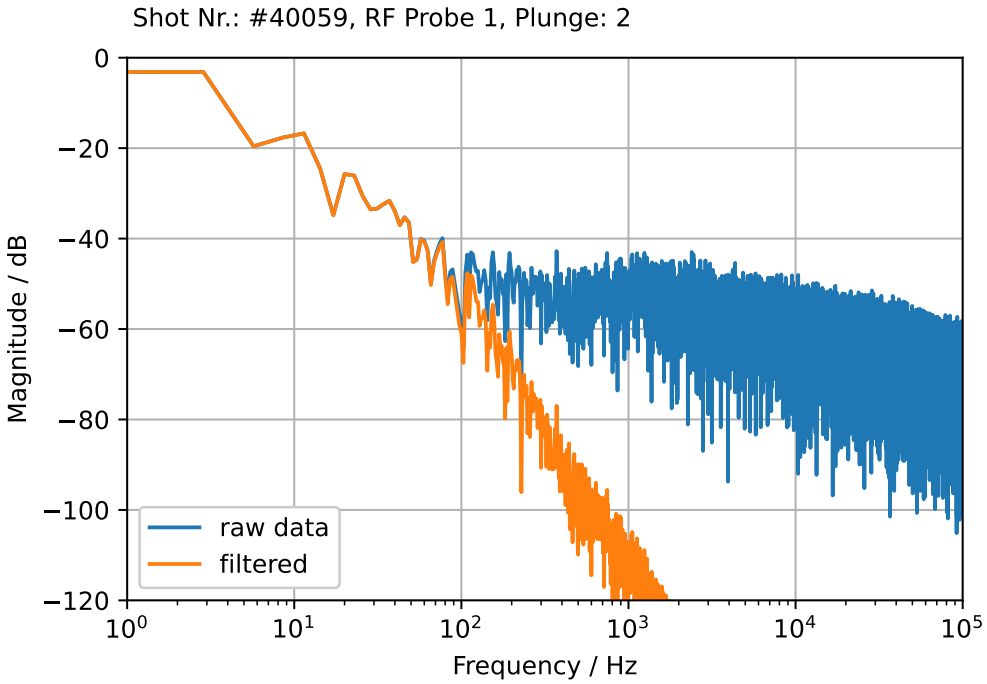

Figure 6.19: Magnitude spectrum of signal S_1 during the 2nd plunge

100 Hz, the spectrum becomes defined by random oscillations with decreasing amplitudes. A digital low pass filter (3rd order Butterworth filter) is used in the following analysis to suppress these oscillations.

Observation (4) is that the signals S_1 and S_2 are often nearly identical. This is in contrast to the expectation that the probe that faces the source - probe 1 - picks up the signal and that the other probe, probe 2, measures a (small) reference background field. There are several possible reasons for the similarity of the signals from the two RF probes.

- As discussed before, the probed RF field is likely a superposition of different wave types, and the signal of interest, the RCs, is embedded in a background field;

- The probe head's main body, the tungsten-coated graphite rod that encases the graphite pins, takes part in the receiving process. The detected signal depends on the momentary electromagnetic potential difference between the graphite pins and the probe head's main body. It is plausible that both probes detect the signals that change the reference potential.
- The four flush-mounted graphite pins are separated from each other by ceramics inside the ball-pen probe head. While ceramics are suitable insulators for low-frequency signals, they permit capacitive coupling between the channels. The signal received by one of the probes couples with some factor to the other probe.

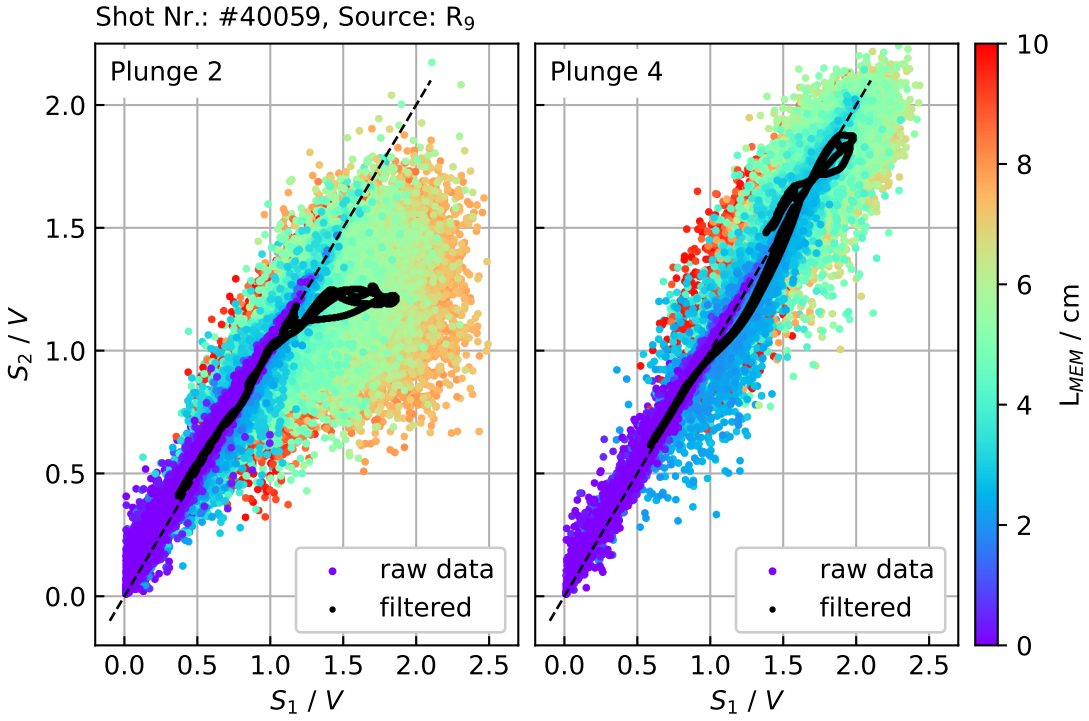

Figure 6.20: Signal S_1 against S_2 for 2nd and 4th plunge

Despite that, it is possible to identify sections in Figure 6.16 where S_1 exceeds S_2. Figure 6.20 shows a plot where S_2 is plotted against S_1 for plunges 2 and 4. In plunge 2, there is clearly an interval along the probe head's path where the data points deviate from the black dashed line (slope = 1). The plot of the signals from plunge 4, on the contrary, does not show a substantial deviation beyond the fluctuation of the data points. The signals from the two RF probes are approximately the same throughout the plunge.

RF signals S_1 and S_2 against n_e and I_p

With the momentary position of the probe head and the density profiles from the Mach probe, it is possible to map the (filtered) signals from the RF probes to the

local plasma density, see Figure 6.21. The Figure contains six column pairs, each

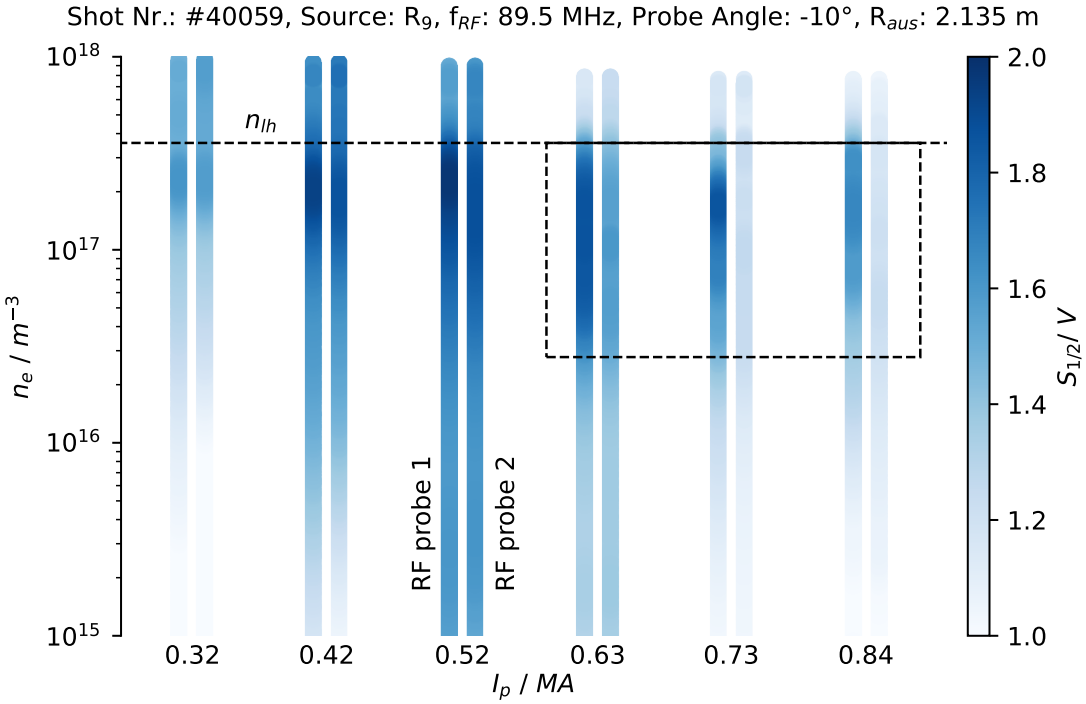

Figure 6.21: Filtered signals from RF probes 1 and 2 against n_e and I_p from discharge #40059

associated with one step of the plasma current scan. The left column of each pair represents the signal from RF probe 1, and the right column represents the signal from RF probe 2. The plasma current associated with each column pair lies between the two columns. The color represents the amplitude of the signals. As discussed before, it is apparent that the signals from the two RF probes coincide most of the time. The signals show a visible difference primarily in the box in the upper right corner of the Figure, where the signal from probe 1 is always larger than the signal from probe 2. (This section also includes the 2nd plunge ($I_p = 730\,\mathrm{kA}$) shown in Figure 6.20.) The data is interpreted as an RF background field with a superimposed signal. The plasma density where this signal is observed is sufficiently low to maintain ICRF slow waves, and the magnetic field lines connect the tile with the probe head approximately at these plasma currents. Because of that, the signals are presumably ICRF slow waves. In the following, the difference of the signals from the two RF probes $S_\Delta = S_1 - S_2$ is examined. Because of the logarithmic response of the RF detectors:

$$S_\Delta = S_1 - S_2 \propto \log\left(P_1/P_r\right) - \log\left(P_2/P_r\right) = \log\left(P_1/P_2\right)$$

The difference between the signals represents the power ratio between RF probes 1 and 2.

RF signal difference S_Δ against n_e and I_p

Figure 6.22 shows S_Δ against the plasma density n_e and the plasma current I_p. The color represents S_Δ, and the width of the column represents the average signal

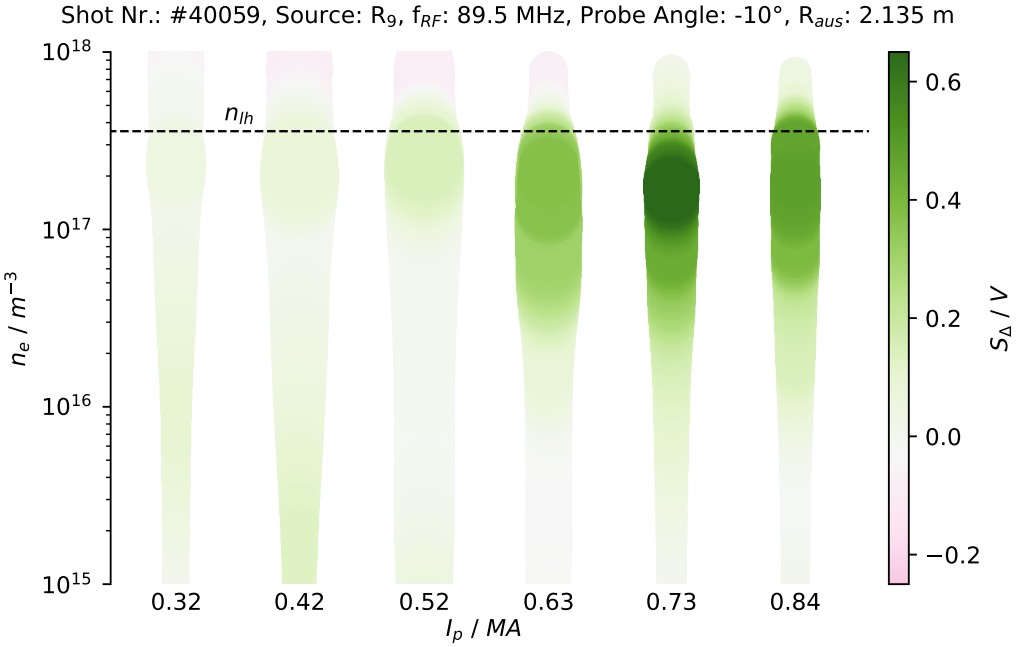

Figure 6.22: S_Δ against I_p and n_e for discharge #40059, an I_p- scan

$(S_1 + S_2)/2$. The plot shows six columns corresponding to the six plasma current steps. It is apparent that S_Δ decreases above n_{lh} for all plasma currents. The signals of interest can not enter the high-density plasma, a key property of ICRF slow waves. It is further apparent that S_Δ is maximal around 730 kA close to n_{lh}. Recall that the signals are scaled logarithmically. Dark green (0.6 V) means that the signal from probe 1 is 12 dB $\approx$ 16 times larger than the signal from probe 2. The maximum signal is observed at the plasma current that connects the limiter tile magnetically with the probe head. This indicates that the RF signals are bound to the magnetic field lines. S_Δ shows large amplitudes also at the adjacent columns corresponding to the plasma currents 630 kA and 830 kA. It is plausible to interpret these signals as marginal by-products that are observable because of the finite size of the source. The limiter tile has a height of approximately 6 cm, and the plasma current sweep changes the height of the endpoint of the magnetic field lines by approximately 1.8 cm/100kA in the experiments with tile R_9 as the source. Three plasma current steps of 100 kA each are just enough to scan the tile past the detector.

Figure 6.23 shows data for an I_p-scan from about 420 kA to 940 kA with the probe head in the +12.5° orientation; notice the change in the probe angle parameter in the Figure title. It is apparent that the signal maximum contracts to a single point in the column that corresponds to an I_p of 630 kA. This demonstrates the sensitivity of the experiments to the orientation of the probe head. When examining

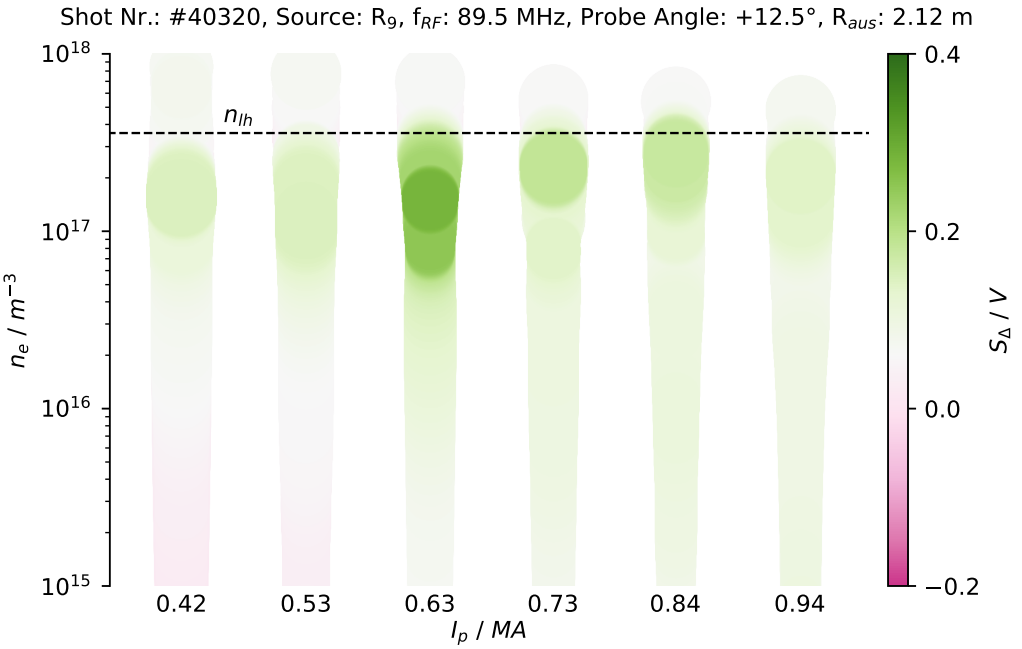

Figure 6.23: S_Δ against I_p and n_e for discharge #40320, an I_p- scan

the difference between the two RF signals, it is possibly advantageous that they are subject to the same magnetic field line. Notice also that the maximum is detected at a plasma current of 630 kA and not at the plasma current corresponding to the fundamental magnetic connection at 730 kA. It is further apparent that the signal ratio S_Δ decreased as visible from the different color ranges. This is possibly caused

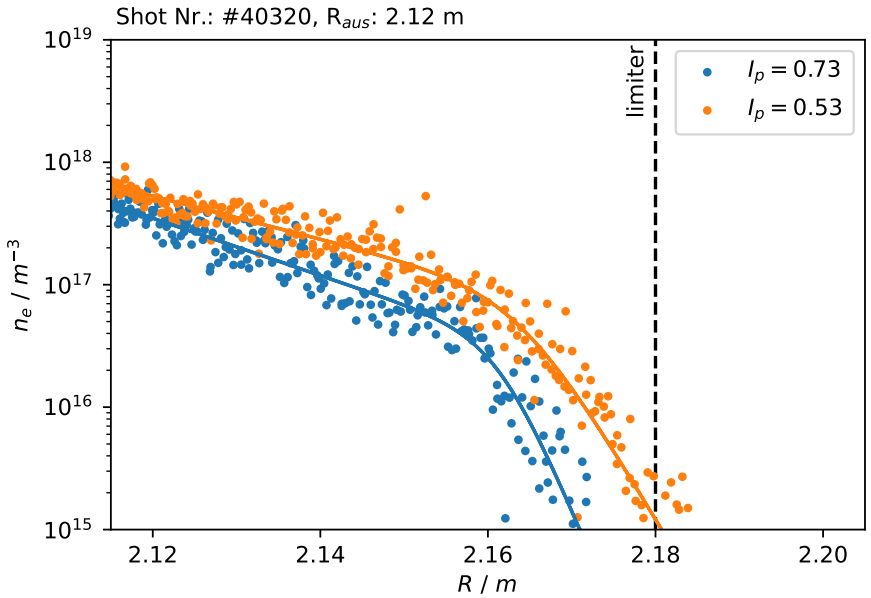

Figure 6.24: Density profiles from the Mach probe at different plasma currents corresponding to plunges 3 and 5 in experiment #40320

by a change in R_{aus} that is $\approx 2.135\,\mathrm{m}$ in #40059 and $\approx 2.12\,\mathrm{m}$ in #40320. This moved the plasma density profiles at the MEM about 1 cm radially inwards for the same plasma currents, as seen when comparing Figures 6.17 and 6.24. This suggests that the coupling of the RF power from the tile to the plasma depends sensitively on the density profile at the tile. Experiments of the R_{aus}-scan type confirmed this.

RF signal delta S_Δ against n_e and R_{aus}

Figure 6.25 shows data from an experiment where the outermost separatrix position R_{aus} was scanned in five steps from about 2.107 m to 2.147 m. The plasma current

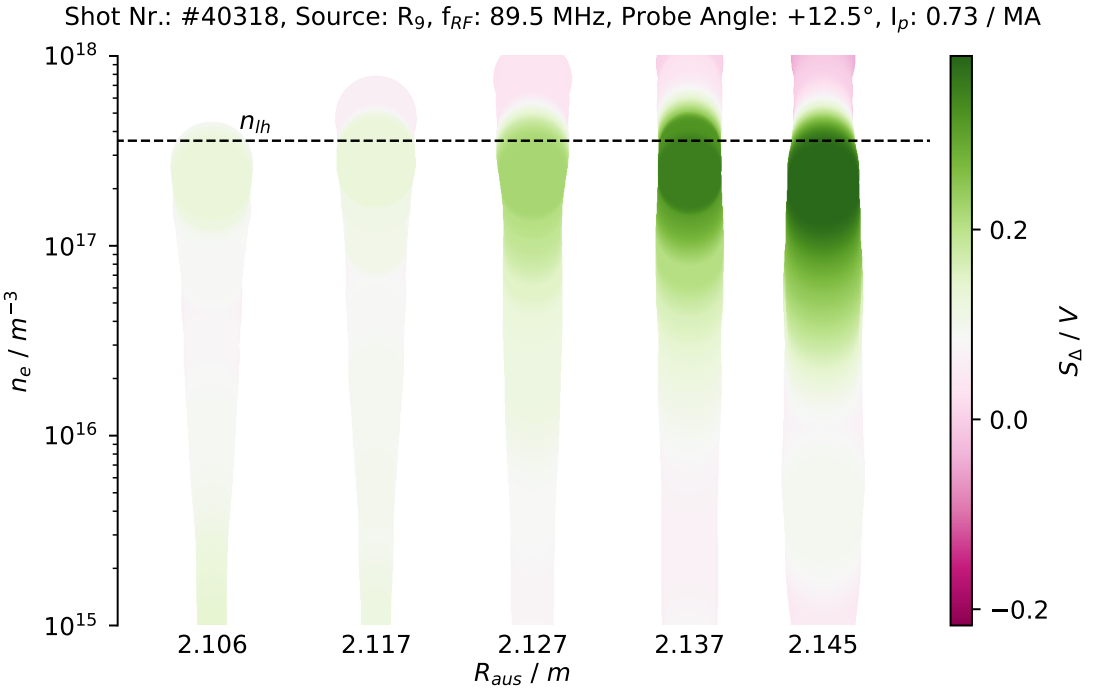

Figure 6.25: S_Δ against n_e and R_{aus} for discharge #40318, a R_{aus}- scan

was $I_p \approx 730\,\mathrm{kA}$, which is again the value that connects the source with the probe head. It is apparent that the amplitude of the RF signals (the width of the columns) but also S_Δ increases towards larger R_{aus}. Notice also that the maximum is always located below n_{lh}. An important deduction from the Figure is the following: Recall that changing R_{aus} causes the density profile to move in the same direction. Figure 6.25 shows that the maximum S_Δ is detected at the same density for all R_{aus}. The geometrical position where the maximum is located consequently moves with the different R_{aus} steps. The RF signals are localized in a particular (narrow) density layer. This is consistent with the qualitative model that predicts how RCs propagate through the torus.

Plausibility checks

To validate the findings, two types of plausibility checks were performed: experiments with a different radio frequency and experiments with a different source. Figure 6.26 shows S_Δ in the established format but from an experiment with $f = 50\,\mathrm{MHz}$. The experiment type is a R_{aus} -scan at a plasma current of $I_p = 730\,\mathrm{kA}$.

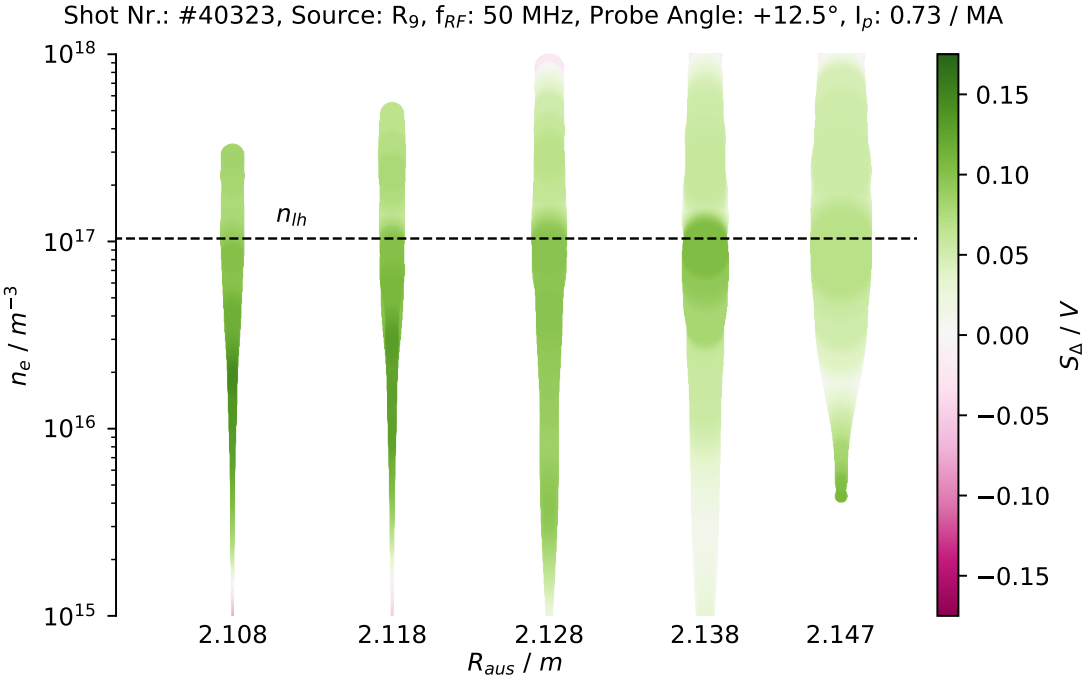

Figure 6.26: S_Δ against n_e and R_{aus} for discharge #40323, a R_{aus} - scan, with $f = 50\,\mathrm{MHz}$

There are two important differences noticeable in the Figure. The first is that the amplitude of the RF signals decreased compared to the higher frequency, particularly for small R_{aus}, as can be seen from the reduced width of the columns. The coupling of RF power from the tile into the empty vessel is weaker at different radio frequencies, see Figure 6.5. It is plausible that this prevails in the presence of the plasma as long as the plasma is far away from the tile. When the plasma gets closer to the tile (larger R_{aus}) the coupling gets stronger as observed before. The second relevant difference is that the amplitude of S_Δ has a maximum at a density slightly above the lower hybrid resonance density at 50 MHz for all R_{aus}. It is possible that the density measurement itself or the generic model function that is used to map the probe position to the density becomes too imprecise for lower plasma densities. Notice that the difference between the dashed n_{lh} line and the maxima is relatively small. Because of that, the deviation is considered to be within the uncertainty of the measurements, and the experiment with $f = 50\,\mathrm{MHz}$ did not reject the previous findings in principle.

Figure 6.27 shows S_Δ in the established format from an experiment where L1 was used as the source tile. The radio frequency is $f = 89.5\,\mathrm{MHz}$. There are

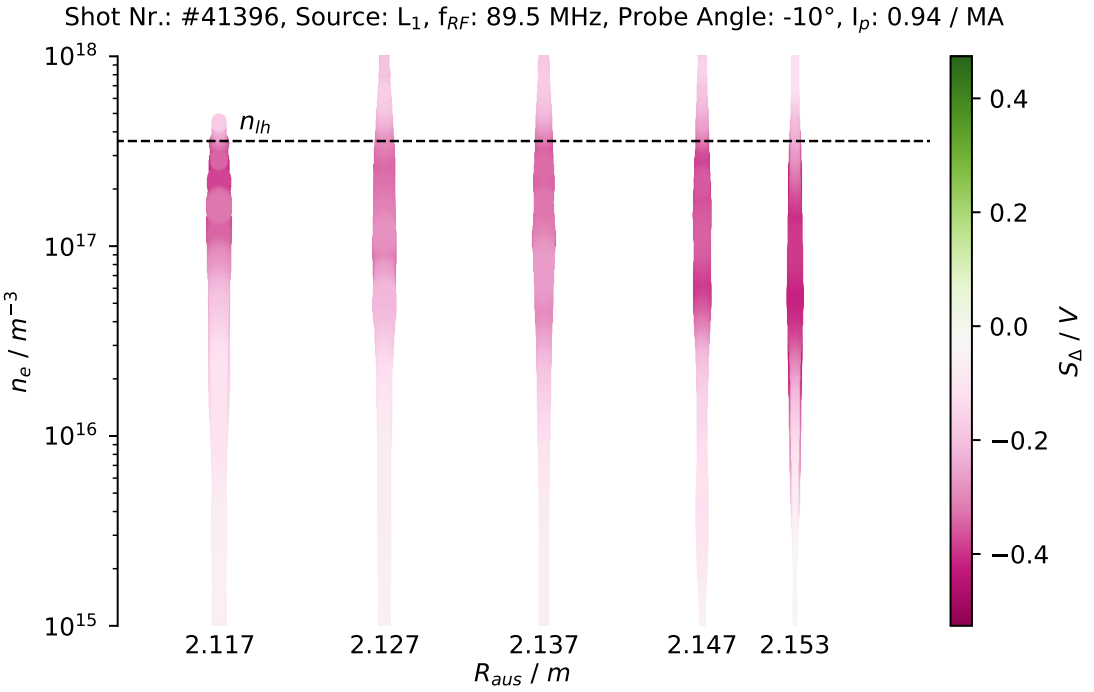

Figure 6.27: S_Δ against n_e and R_{aus} for discharge #41396, a R_{aus} - scan, with limiter tile L1 as the RF source

four relevant observations in the Figure: The 1st is, that S_Δ is negative as can be seen from the color. The signal that is detected by RF probe 2 is larger than the one that is detected by RF probe 1. This is an important plausibility check because it confirms that the direction from which the signal approaches the probe head matters. The second observation is that the signal amplitude (the width of the columns) is, in principle, lower compared to the experiments where tile R9 was used as the RF source. This is possibly a consequence of the different setups of the two sources. The vacuum reflection coefficient is different for the different sources (Figures 6.5 and 6.7) and it is plausible that this applies in principle also in the plasma. Recall also that the distance between the source and the detector is about three times larger compared to experiments with limiter tile R9. It is plausible that the amplitude of the signals reduced along the path. The 3rd important validation is that S_Δ drops above the lower hybrid resonance density in agreement with the previous observations. The 4th important observation is that the signals show a several maxima distributed unevenly through the profiles. There is possibly a maximum of around n_{lh} for all R_{aus}, but the profiles are versatile. It is possible that the signals are corrupted by secondary signals along the longer path to the probe that were irrelevant for shorter distances. These might be, for example, reflections or secondary emissions of the RCs from components along the signal path, as described by the RAPLICASOL simulations in Section 4.2.

Conclusion

The experimental findings are summarized and interpreted: The RF probes in the ball-pen probe head detect signals starting from the moment when RF power is sent to the tiles. The signals that are detected by the two probes during a plunge are similar and show an ambiguous RF field profile. A difference between the two signals exists with an asymmetry towards the probe that faces the source. This difference shows several features that are intrinsic to ICRF slow waves:

- the signal is maximal for particular magnetic geometries, indicating that the direction of propagation of the RF signals is governed by the background magnetic field;
- the signal only exists in plasma with densities below the lower hybrid resonance density;
- the signals are localized in particular density layers;
- the density layer in which the signals are located depends on the radio frequency.

Furthermore, it was observed that both the amplitude of the detected RF signals and the difference of the two signals depend on the proximity of the plasma to the source tile. The experimental findings are interpreted as a superposition of an RF background field and propagating ICRF slow waves.

Chapter 7

Conclusion and Outlook

Heating plasma with ion cyclotron range of frequencies (ICRF) waves is an established method in magnetic confinement fusion (MCF). However, the compatibility of ICRF heating with reactor-relevant plasma-facing components (PFC) is questioned by experimental findings. The operation of the ICRF antennas can cause increased sputtering of elements of the antenna periphery. This can contaminate the plasma and impede access to advanced operation scenarios that are considered reactor-relevant. It is believed that the increased sputtering is the result of a rectification process of parallel radio frequency (RF) electric fields at the plasma sheath. The ICRF slow wave is a potential carrier for these fields. If the ICRF slow wave propagates, it is possible that sputtering is induced at locations that are far away from the RF source. The objective of this work was to study experimentally the propagation of ICRF slow waves in a reactor-relevant scrape-off layer (SOL). The pursued approach consists of three aspects:

- a method to excite ICRF slow waves;
- a hypothesis on how ICRF slow waves propagate;
- a concept of how to measure the slow waves.

The preceding chapters address these points from different perspectives.

Simulations with the RAPLICASOL routine suggest that components that are embedded in a magnetized plasma with a plasma density below the lower hybrid resonance density excite resonance cones (RCs) when RF fields are applied to them. RCs are a particular type of propagating ICRF slow waves with large electric field amplitudes. The reason for the predominant excitation of RCs is a divergence condition for the electric field at particular points along the RF source/plasma boundary. It can be shown that, in practice, any source contour will have points where this divergence condition exists. It is, therefore, plausible to assume that RCs will always dominate the RF electric field, considering propagating ICRF slow waves. The main goal of this thesis was, therefore, to study propagating (lower hybrid) RCs.

The RF electric field structure of RCs is a cone when launched from a point-like source. The cone opens up along the background magnetic field depending

on the wave frequency and the plasma parameter. Specifically at larger magnetic field amplitudes and for opening angles of about $\theta_c > 3°$, this dependence becomes $\tan\theta_c \approx \omega/\omega_{pe}$. The opening ratio of the RC $\tan\theta_c = r/z$ is proportional to the wave frequency and inversely proportional to the square root of the local plasma density. This has practical implications: RCs distort at plasma density gradients. The section of a RC that enters the lower density region leaves the plasma because θ_c increases continuously towards lower plasma density. The section of the RC that enters the higher density region approaches zero degrees at the lower hybrid resonance density. The RF signal that reaches the lower hybrid resonance layer stays in it and follows the background magnetic field.

The experiments on the ion sheath test arrangement (IShTAR) aimed to validate the experimental approach. A localized source, the wire-loop antenna, was placed inside IShTAR. The wire-loop antenna creates a scenario that resembles the RAPLICASOL simulations. A plasma formed when sending RF power to the wire-loop antenna. The light emissions from the plasma show linear structures that are consistent with RCs. Two RF probes were scanned through the plasma to probe the RF electric field pattern. Parameter scans were performed to identify the wave type. The $\theta_c \approx \omega/\omega_{pe}$ approximation indicates the parameters influencing the RC characteristics: the wave frequency and the plasma density. The wave frequency was changed directly at the RF oscillator. The plasma density was changed by manipulating the RF power level that was fed to the wire-loop antenna. The findings from the parameter scans coincide with a model for propagating RC. The experiments at IShTAR have shown three important things:

- RF probes are suitable tools to probe the RF electric field;
- parameter scans are a viable method to identify the RF wave type;
- RCs propagate in IShTAR with the expected properties in the ICRF parameter range.

Experiments on AUG were building on the previous findings. To excite RCs in the AUG SOL, an element of the ICRF antenna limiter was activated with RF fields. This was achieved by insulating a single limiter element from the rest of the antenna limiter and connecting it to the antenna box only via a shunt resistor. The tile and the shunt form an LC resonator in the frequency range of interest. To probe the RF electric field, two graphite pins at the Mittelebenenmanipulator (MEM) were utilized as RF probes. The plasma parameter in AUG deviates from the conditions in IShTAR. The background magnetic field wraps around the torus, and the plasma density profile shows steep gradients, particularly in the SOL. This required modifying the hypothesis of how the RCs propagate and how to identify the wave type. Two requirements for successful experiments were identified. 1st, The lower hybrid resonance density layer had to be located in front of the antenna limiter to enable the propagation of RCs over longer distances in the SOL. 2nd, There had to be a magnetic connection between the source and the probe because RCs expand along the magnetic field lines. Because of the steep density gradients, it

is expected that a section of the RCs is localized close to the lower hybrid resonance density layer. To identify the RF signals as propagating RCs for types of tests were performed at AUG. 1st I_p-scans, 2nd R_{aus}-scans, 3rd experiments with different radio frequencies and 4th experiments from different sources. 1st I_p-scans showed that the detected RF signals are bound to the background magnetic field lines. By modifying the plasma current I_p it is possible to change the poloidal component of the magnetic field. The inclination angle of the magnetic field lines consequently changes. If the signals are bound to the magnetic field lines, it is expected that there is a maximal RF field amplitude at a certain plasma current. 2nd R_{aus}-scans showed that the detected RF signals are localized in a particular density layer. By changing the outermost separatrix position R_{aus}, it is possible to move the lower hybrid resonance density layer in front of the limiter. The point where the RF signal maximum is located has to move accordingly if the signals are localized in a particular density layer. 3rd I_p and R_{aus} scans at a different radio frequency addressed the influence that the wave frequency has on the RCs propagation. 4th An experiment from a different source added a plausibility check. The experiments indicates that propagating ICRF slow waves in the form of RCs were detected in the AUG SOL.

RCs are a potential candidate to transport RF electrical fields through a SOL of an MCF experiment, provided that the plasma density is sufficiently low. In modern tokamaks, this is typically not the case for most of the SOL. The plasma density in front of the limiters is typically above the lower hybrid resonance density, and the ICRF slow wave can not propagate there. However, in the far SOL, in particular, in the limiter shadow, where the plasma density can fall below n_{lh}, RCs can take a determining role in the RF field distribution because of the large electric field that is associated with them. Considering the observation of reemission and reflection of the RCs that were observed in the simulations, it is plausible that RCs can define the RF field also in low-density regions that are far away from the RF source.

Future work can address different questions that remain unanswered.

- What is the influence of the plasma sheath on the excitation of RCs? RCs were identified as the dominant solution type because of a divergence condition at the source/plasma boundary. However, this description did not include a sheath description.

- What is the RF background field that was detected by the two RF probes in the experiments on AUG? The two RF probes detected a similar RF signal. Are these signals a consequence of an imperfect measurement apparatus, or is it a real RF field? If it is a real RF field, what is the origin of these signals? The signals were observed in regions with density above the lower hybrid resonance.

- What is the origin of the localized RF signals that were detected with the spectrum analyzer, and what is the origin of the broadband background RF signals?

Bibliography

[1] H.-S. Bosch and G.M. Hale. "Improved formulas for fusion cross-sections and thermal reactivities". In: *Nuclear Fusion* 32.4 (Apr. 1992), p. 611. DOI: 10.1088/0029-5515/32/4/I07. URL: https://dx.doi.org/10.1088/0029-5515/32/4/I07.

[2] A. B. Zylstra et al. "Burning plasma achieved in inertial fusion". In: *Nature* 601.7894 (Jan. 2022), pp. 542–548. ISSN: 1476-4687. DOI: 10.1038/s41586-021-04281-w. URL: https://doi.org/10.1038/s41586-021-04281-w.

[3] Elizabeth Gibney. "Nuclear-fusion reactor smashes energy record". In: (2022). DOI: 10.1038/d41586-022-00391-1.

[4] IPP. *Wendelstein 7-X erreicht Meilenstein: Leistungsplasma mit Gigajoule Energieumsatz über acht Minuten erzeugt.* URL: https://www.ipp.mpg.de/5322014/01_23?c=9995 (visited on 04/19/2023).

[5] ITER. *What is ITER?* URL: https://www.iter.org/proj/inafewlines (visited on 04/20/2023).

[6] J.-M. Noterdaeme. "Fifty years of progress in ICRF, from first experiments on the model C stellarator to the design of an ICRF system for DEMO". In: *AIP Conference Proceedings* 2254.1 (Sept. 2020). 020001. ISSN: 0094-243X. DOI: 10.1063/5.0014254. eprint: https://pubs.aip.org/aip/acp/article-pdf/doi/10.1063/5.0014254/13709599/020001_1_online.pdf. URL: https://doi.org/10.1063/5.0014254.

[7] J.R. Myra, D.A. D'Ippolito, and M.J. Gerver. "Faraday screen sheaths and impurity production during ion cyclotron heating". In: *Nuclear Fusion* 30.5 (May 1990), p. 845. DOI: 10.1088/0029-5515/30/5/004. URL: https://dx.doi.org/10.1088/0029-5515/30/5/004.

[8] Vl.V. Bobkov et al. "Assessment of compatibility of ICRF antenna operation with full W wall in ASDEX Upgrade". In: *Nuclear Fusion* 50.3 (Feb. 2010), p. 035004. DOI: 10.1088/0029-5515/50/3/035004. URL: https://dx.doi.org/10.1088/0029-5515/50/3/035004.

[9] V. Bobkov et al. "First results with 3-strap ICRF antennas in ASDEX Upgrade". In: *Nuclear Fusion* 56.8 (July 2016), p. 084001. DOI: 10.1088/0029-5515/56/8/084001. URL: https://dx.doi.org/10.1088/0029-5515/56/8/084001.

[10] Paul M. Bellan. *Fundamentals of Plasma Physics*. Cambridge University Press, 2008.

[11] Pascal Chabert and Nicholas Braithwaite. *Physics of Radio-Frequency Plasmas*. Cambridge University Press, 2011. DOI: 10.1017/CBO9780511974342.

[12] Jane P. Chang Francis F. Chen. *Lecture Notes on Principles of Plasma Processing*. 1. Springer New York, NY, 2003. ISBN: 978-0-306-47497-2.

[13] I. H. Hutchinson. *Principles of Plasma Diagnostics*. 2nd ed. Cambridge University Press, 2002. DOI: 10.1017/CBO9780511613630.

[14] Roman Schrittwieser et al. "Measurements with an emissive probe in the CASTOR tokamak". In: *Plasma Physics and Controlled Fusion* 44.5 (Apr. 2002), p. 567. DOI: 10.1088/0741-3335/44/5/305. URL: https://dx.doi.org/10.1088/0741-3335/44/5/305.

[15] M.A. Lieberman. "Analytical solution for capacitive RF sheath". In: *IEEE Transactions on Plasma Science* 16.6 (1988), pp. 638–644. DOI: 10.1109/27.16552.

[16] Thomas Howard Stix. *Waves in plasmas*. 1st ed. American Institute of Physics, 1992.

[17] ixtract IPP. *Schematic of ASDEX Upgrade*. URL: https://www.ipp.mpg.de/1471827/asdex_upgrade (visited on 03/30/2023).

[18] Volker Rohde IPP. *AUG Gefäss 2015*. 2015. URL: https://www.ipp.mpg.de/1471827/asdex_upgrade?page=3 (visited on 03/30/2023).

[19] A. Kallenbach, for the ASDEX Upgrade Team, and the EUROfusion MST1 Team. "Overview of ASDEX Upgrade results". In: *Nuclear Fusion* 57.10 (June 2017), p. 102015. DOI: 10.1088/1741-4326/aa64f6. URL: https://dx.doi.org/10.1088/1741-4326/aa64f6.

[20] U. Stroth et al. "Progress from ASDEX Upgrade experiments in preparing the physics basis of ITER operation and DEMO scenario development". In: *Nuclear Fusion* 62.4 (Mar. 2022), p. 042006. DOI: 10.1088/1741-4326/ac207f. URL: https://dx.doi.org/10.1088/1741-4326/ac207f.

[21] J. C. Fuchs et al. *Routines and Tools for Working with Equilibrium Data*. Available at https://www.aug.ipp.mpg.de/aug/manuals/kk/libkk.pdf. Max-Planck-Institut für Plasmaphysik. Garching bei München, Mar. 2022.

[22] P. J. McCarthy, P. Martin, and W. Schneider. *The CLISTE Interpretive Equilibrium Code*. eng. Tech. rep. IPP 5/85. Garching: Max-Planck-Institut für Plasmaphysik, 1999.

[23] R. Fischer et al. "Integrated Data Analysis of Profile Diagnostics at ASDEX Upgrade". In: *Fusion Science and Technology* 58.2 (2010), pp. 675–684. DOI: 10.13182/FST10-110. eprint: https://doi.org/10.13182/FST10-110. URL: https://doi.org/10.13182/FST10-110.

[24] T. Lunt et al. "Study of detachment in future ASDEX Upgrade alternative divertor configurations by means of EMC3-EIRENE". In: *Nuclear Materials and Energy* 26 (2021), p. 100950. ISSN: 2352-1791. DOI: https://doi.org/10.1016/j.nme.2021.100950. URL: https://www.sciencedirect.com/science/article/pii/S2352179121000399.

[25] Helmut Faugel. Photograph. Aug. 2020.

[26] G. Grenfell et al. "High-heat flux ball-pen probe head in ASDEX-Upgrade". In: *Review of Scientific Instruments* 93.2 (Feb. 2022). 023507. ISSN: 0034-6748. DOI: 10.1063/5.0075846. eprint: https://pubs.aip.org/aip/rsi/article-pdf/doi/10.1063/5.0075846/16714918/023507_1_online.pdf. URL: https://doi.org/10.1063/5.0075846.

[27] W. Tierens et al. "Validation of the ICRF antenna coupling code RAPLICASOL against TOPICA and experiments". In: *Nuclear Fusion* 59.4 (Jan. 2019), p. 046001. DOI: 10.1088/1741-4326/aaf455. URL: https://dx.doi.org/10.1088/1741-4326/aaf455.

[28] M Usoltceva et al. "Simulation of the ion cyclotron range of frequencies slow wave and the lower hybrid resonance in 3D in RAPLICASOL". In: *Plasma Physics and Controlled Fusion* 61.11 (Oct. 2019), p. 115011. DOI: 10.1088/1361-6587/ab476d. URL: https://dx.doi.org/10.1088/1361-6587/ab476d.

[29] Jean-Pierre Berenger. "A perfectly matched layer for the absorption of electromagnetic waves". In: *Journal of Computational Physics* 114.2 (1994), pp. 185–200. ISSN: 0021-9991. DOI: https://doi.org/10.1006/jcph.1994.1159. URL: https://www.sciencedirect.com/science/article/pii/S0021999184711594.

[30] Eliane Bécache, Patrick Joly, and Maryna Kachanovska. "Stable perfectly matched layers for a cold plasma in a strong background magnetic field". In: *Journal of Computational Physics* 341 (2017), pp. 76–101. ISSN: 0021-9991. DOI: https://doi.org/10.1016/j.jcp.2017.03.051.

[31] Jonathan Jacquot. "Description non-linéaire auto-cohérentede la propagation d'ondes radiofréquenceset de la périphérie d'un plasma magnétisé". PhD thesis. Université de Lorraine, 2013.

[32] Marco Brambilla. *Kinetic theory of plasma waves: homogeneous plasmas*. 96. Oxford University Press, 1998.

[33] Laurent Colas et al. "Perfectly Matched Layers for time-harmonic transverse electric wave propagation in cylindrical and toroidal gyrotropic media". In: *Journal of Computational Physics* 389 (July 2019), pp. 94–110. DOI: 10.1016/j.jcp.2019.02.017. URL: https://hal-cea.archives-ouvertes.fr/cea-02103360.

[34] W. Tierens, F. Paulus, and R. Bilato. "Resonance cones in cold plasma: Origin, singularities, and power flow". In: *Physics of Plasmas* 30.10 (Oct. 2023), p. 102102. ISSN: 1070-664X. DOI: 10.1063/5.0152069. eprint: https://pubs.aip.org/aip/pop/article-pdf/doi/10.1063/5.0152069/18150805/102102_1_5.0152069.pdf. URL: https://doi.org/10.1063/5.0152069.

[35] R.W.Gould R.K. Fischer. "Resonance cones in the field pattern of a short antenna in an anisotropic plasma". In: *Physical Review Letters* 22.21 (1969), pp. 1093–1095.

[36] Gary Bradski. "The Opencv Library". In: *Dr. Dobb's J. Softw. Tools* 25 (Nov. 2000).

[37] Pauli Virtanen et al. "SciPy 1.0: Fundamental Algorithms for Scientific Computing in Python". In: *Nature Methods* 17 (2020), pp. 261–272. DOI: 10.1038/s41592-019-0686-2.

[38] Roman Ochoukov. "Schematic of important Plasma Facing Components on the LFS in AUG". 2023.